

University of Nebraska - Lincoln

DigitalCommons@University of Nebraska - Lincoln

---

Mechanical (and Materials) Engineering --  
Dissertations, Theses, and Student Research

Mechanical & Materials Engineering, Department  
of

---


Summer 8-16-2014

# Design and Development of a Miniature *In Vivo* Surgical Robot with Distributed Motor Control for Laparoendoscopic Single-Site Surgery

Eric J. Markvicka

University of Nebraska-Lincoln, [eric.markvicka@gmail.com](mailto:eric.markvicka@gmail.com)

Follow this and additional works at: <http://digitalcommons.unl.edu/mechengdiss>

 Part of the [Biomedical Devices and Instrumentation Commons](#), [Surgery Commons](#), and the [Surgical Procedures, Operative Commons](#)

---

Markvicka, Eric J., "Design and Development of a Miniature *In Vivo* Surgical Robot with Distributed Motor Control for Laparoendoscopic Single-Site Surgery" (2014). *Mechanical (and Materials) Engineering -- Dissertations, Theses, and Student Research*. 75. <http://digitalcommons.unl.edu/mechengdiss/75>

This Article is brought to you for free and open access by the Mechanical & Materials Engineering, Department of at DigitalCommons@University of Nebraska - Lincoln. It has been accepted for inclusion in Mechanical (and Materials) Engineering -- Dissertations, Theses, and Student Research by an authorized administrator of DigitalCommons@University of Nebraska - Lincoln.

DESIGN AND DEVELOPMENT OF A MINIATURE *IN VIVO* SURGICAL ROBOT  
WITH DISTRIBUTED MOTOR CONTROL FOR LAPAROENDOSCOPIC SINGLE-  
SITE SURGERY

by

Eric John Markvicka

A THESIS

Presented to the Faculty of

The Graduate College at the University of Nebraska

In Partial Fulfillment of Requirements

For the Degree of Master of Science

Major: Mechanical Engineering & Applied Mechanics

Under the Supervision of Professor Shane M. Farritor

Lincoln, Nebraska

August, 2014

DESIGN AND DEVELOPMENT OF A MINIATURE *IN VIVO* SURGICAL ROBOT  
WITH DISTRIBUTED MOTOR CONTROL FOR LAPAROENDOSCOPIC SINGLE-  
SITE SURGERY

Eric John Markvicka, M.S.

University of Nebraska, 2014

Advisor: Shane Farritor

Paradigm shifts in invasiveness, recovery time, cosmesis, and cost have been seen within the field of general surgery through major advances in surgical technology. Some of the most advanced types of general surgery now include Minimally Invasive Surgery (MIS), LaparoEndoscopic Single-Site (LESS) surgery, and Natural Orifice Translumenal Endoscopic Surgery (NOTES). One of the newest and rapidly developing catalysts is robotic platforms. Such platforms have improved ergonomics and control, increased workspace and dexterity, and have surpassed the efficacy of many non-robotic platforms such as traditional laparoscopic surgical tools.

This thesis presents the design and development of a four-degree-of-freedom (4-DOF) miniature *in vivo* surgical robot with distributed motor control for laparoendoscopic single-site surgery. The robotic platform consists of a two-armed robotic prototype, distributed motor control system, insufflated insertion device, and a remote surgeon interface.

*“Make everything as simple as possible, but not simpler.”*  
Albert Einstein

*First of all, I would like to thank my advisor, Dr. Shane Farritor, for his support and guidance throughout this project. I would like to thank my fellow colleagues for their continued support and significant contributions. Without them, this work would not have been possible.*

*I would like to thank my incredible wife, Stacie. Her unending love, patience, and encouragement have allowed me to pursue my dreams.*

*Finally, I would like to thank my parents for their endless support. They are the foundation of who I am today and I am forever grateful for everything they have done.*

This research was performed under support provided by National Science Foundation, NASA EPSCoR, Nebraska Research Initiative, Telemedicine and Advanced Technology Research Center, and the NASA Nebraska Space Grant Consortium.

# Table of Contents

<b>CHAPTER 1: INTRODUCTION .....</b>	<b>1</b>
<b>CHAPTER 2: BACKGROUND .....</b>	<b>4</b>
SECTION 2.1: MINIMALLY INVASIVE SURGERY.....	4
<i>Section 2.1.1: Laparoscopic Surgery .....</i>	<i>4</i>
<i>Section 2.1.2: Natural Orifice Transluminal Endoscopic Surgery (NOTES).....</i>	<i>4</i>
<i>Section 2.1.3: LaparoEndoscopic Single-Site (LESS) Surgery.....</i>	<i>5</i>
SECTION 2.2: ROBOTIC MINIMALLY INVASIVE SURGERY.....	5
<i>Section 2.2.1: Robotic Laparoscopic Surgery .....</i>	<i>6</i>
<i>Section 2.2.2: Robotic NOTES (R-NOTES).....</i>	<i>8</i>
<i>Section 2.2.3: Robotic LESS Surgery (R-LESS).....</i>	<i>9</i>
<b>CHAPTER 3: MOTIVATION .....</b>	<b>13</b>
SECTION 3.1: OVERVIEW .....	13
SECTION 3.2: DESIGN REQUIREMENTS .....	14
<b>CHAPTER 4: ERIC-BOT 2.0 SYSTEM DESCRIPTION .....</b>	<b>18</b>
SECTION 4.1: KINEMATIC MODEL .....	19
<i>Section 4.1.1: Forward Kinematics .....</i>	<i>21</i>
<i>Section 4.1.2: Workspace .....</i>	<i>23</i>
<i>Section 4.1.3: Jacobian Matrix.....</i>	<i>27</i>
<i>Section 4.1.4: Theoretical Abilities.....</i>	<i>28</i>
Section 4.1.4.1: Manipulability.....	29
Section 4.1.4.2: Forces .....	30
Section 4.1.4.3: Velocities .....	34
SECTION 4.2: PHYSICAL DESIGN.....	36

<i>Section 4.2.1: Torso</i> .....	37
<i>Section 4.2.2: Upper Arm</i> .....	39
<i>Section 4.2.3: Forearms</i> .....	40
Section 4.2.3.1: Monopolar Hook Cautery .....	41
Section 4.2.3.2: Grasper End-Effector .....	42
Section 4.2.3.3: Alternate Grasper End-Effector .....	44
<i>Section 4.2.4: Bevel Gear Manufacturing</i> .....	45
<i>Section 4.2.5: Flexibility Methods</i> .....	48
<i>Section 4.2.6: Vision System</i> .....	52
<i>Section 4.2.7: Size Comparisons</i> .....	54
SECTION 4.3: CONTROL SYSTEM .....	55
<i>Section 4.3.1: Hardware and Communication</i> .....	55
Section 4.3.1.1: Brushless DC Distributed Motor Control .....	56
<i>Section 4.3.2: Inverse Kinematics</i> .....	59
<i>Section 4.3.3: Surgical User Interface</i> .....	62
SECTION 4.4: INSUFFLATED INSERTION .....	64
<b>CHAPTER 5: CONCLUSIONS AND FUTURE WORK</b> .....	<b>68</b>
<b>REFERENCES</b> .....	<b>69</b>
<b>APPENDIX A. KINEMATIC ANALYSIS</b> .....	<b>75</b>
<b>APPENDIX B. THEORETICAL ABILITIES AND SUPPORTING MATERIAL</b> .....	<b>79</b>
<b>APPENDIX C. BRUSHLESS DC MOTOR DATA SHEETS</b> .....	<b>88</b>
<b>APPENDIX D. DISTRIBUTED MOTOR CONTROL SCHEMATICS</b> .....	<b>93</b>



## LIST OF FIGURES

FIGURE 1.1: MINIATURE <i>IN VIVO</i> SURGICAL ROBOT. ....	3
FIGURE 2.1: THE <i>DA VINCI</i> <sup>®</sup> SURGICAL SYSTEM, MODEL XI (©2014 INTUITIVE SURGICAL, INC.).....	6
FIGURE 2.2: THE LOCATION OF THE PORTS AND ROBOTIC CART FOR A ROBOTIC ASSISTED SIGMOID COLECTOMY: A) THE LOWER LEFT OBLIQUE LOCATION OF THE ROBOTIC CART, B) THE LEFT VERTICAL LOCATION OF THE ROBOTIC CART. (BAIK ET AL.) ..	8
FIGURE 2.3: THE <i>DA VINCI</i> <sup>®</sup> SYSTEM SET UP TO PERFORM AN R-LESS PROCEDURE USING CURVED CANNULAS (©2014 INTUITIVE SURGICAL, INC.) .....	10
FIGURE 2.4: THE <i>DA VINCI</i> <sup>®</sup> SP <sup>™</sup> SURGICAL SYSTEM (©2014 INTUITIVE SURGICAL, INC.).....	11
FIGURE 2.5: EB2.0 DESIGN .....	12
FIGURE 4.1: EVOLUTION OF MINIATURE <i>IN VIVO</i> SURGICAL DEVICES FROM THE ADVANCED SURGICAL TECHNOLOGIES LAB AT THE UNIVERSITY OF NEBRASKA-LINCOLN. A) FIRST GENERATION OF SURGICAL DEVICES DEVELOPED FOR NOTES (LEHMAN ET AL.), B) FIRST GENERATION OF SURGICAL DEVICES DEVELOPED FOR LESS SURGERY (WOOD ET AL.), C) SECOND GENERATION OF SURGICAL DEVICES DEVELOPED FOR LESS SURGERY (WORTMAN ET AL.), D) EB2.0 THIRD GENERATION OF SURGICAL DEVICES DEVELOPED FOR LESS SURGERY.....	19
FIGURE 4.2: KINEMATIC MODEL OF EB2.0. FRAME {1} IS LOCATED AT (6, 0, 0) [MM]. ....	20
FIGURE 4.3: EB2.0 WITH LABELED DEGREES OF FREEDOM AND LINK NAMING CONVENTION. ....	20
FIGURE 4.4: DERIVATION OF THE TRANSFORMATION MATRIX BETWEEN FRAMES {2} AND {3}.....	21
FIGURE 4.5: EB2.0 SUPERIMPOSED ON TOP OF A SLICE OF THE ENTIRE ROBOTIC WORKSPACE AT $\theta_1 = 0$ DEGREES.....	24
FIGURE 4.6: LEFT: EB2.0 SUPERIMPOSED ON TOP OF A SLICE OF THE INTERSECTING ROBOTIC WORKSPACE AT $\theta_1 = 0$ DEGREES. RIGHT: EB2.0 WITH THE INTERSECTING WORKSPACE OF THE DEVICE. ....	25
FIGURE 4.7: EB2.0 SUPERIMPOSED ON TOP OF A SLICE OF THE ENTIRE ROBOTIC WORKSPACE AT $\theta_1 = 0$ DEGREES. BLACK: ORIGINAL INTERESTING WORKSPACE, GREEN + BLACK: INTERESTING WORKSPACE USING $\theta_{2, \text{ALTERNATIVE}}$ , GREEN + BLACK + RED: ROBOTIC WORKSPACE USING $\theta_{2, \text{ALTERNATIVE}}$ .....	26
FIGURE 4.8: EB2.0 MANIPULABILITY MEASURE, RIGHT ARM. ....	30
FIGURE 4.9: EB2.0 STATIC ENDPOINT FORCE IN EACH PRINCIPAL CARTESIAN AXIS, RIGHT ARM (PLEASE NOTE THAT THE FORCE SCALE FOR EACH INDIVIDUAL PLOT IS DIFFERENT: Fx: 10-0.8 [N], Fy: 4-0.8 [N], Fz: 10-2.2 [N]). ....	31

FIGURE 4.10: FREE BODY DIAGRAM (FBD) OF EB2.0 WHEN GRAVITY FULLY ACTS ON EACH BODY. TOP: FBD FOR SHOULDER PITCH, BOTTOM: FBD FOR SHOULDER AND ELBOW YAW.....	32
FIGURE 4.11: EB2.0 MINIMUM STATIC ENDPOINT FORCE, RIGHT ARM (FORCES ARE IN NEWTONS WITH A SCALE FROM 0.8-3 [N]).....	33
FIGURE 4.12: EB2.0 ENDPOINT VELOCITY IN EACH PRINCIPAL CARTESIAN AXIS, RIGHT ARM (PLEASE NOTE THAT THE VELOCITY SCALE FOR EACH INDIVIDUAL PLOT IS DIFFERENT: $V_x$ : 70-800 [MM/S], $V_y$ : 70-1000 [MM/S], $V_z$ : 72-500 [MM/S]).....	35
FIGURE 4.13: EB2.0 MINIMUM ENDPOINT VELOCITY, RIGHT ARM (VELOCITY IS IN MM/SEC WITH A SCALE FROM 70-150 [MM/SEC]).....	36
FIGURE 4.14: ISOMETRIC VIEW OF EB2.0.....	37
FIGURE 4.15: EB2.0 TORSO CROSS SECTION VIEW.....	38
FIGURE 4.16: EB2.0 "D-SHAPED" GEOMETRY SPUR GEAR TO SHAFT MATE.....	38
FIGURE 4.17: EB2.0 10MM MOTOR CLAMP.....	39
FIGURE 4.18: EB2.0 UPPER ARM CROSS SECTION VIEW.....	40
FIGURE 4.19: EB2.0 MONOPOLAR HOOK CAUTERY CROSS SECTION VIEW.....	41
FIGURE 4.20: EB2.0 2-DOF FOREARM CROSS SECTION VIEW.....	43
FIGURE 4.21: EB2.0 GRASPER CROSS SECTION VIEW.....	44
FIGURE 4.22: EB2.0 ALTERNATIVE GRASPER FOREARM DESIGN CROSS SECTION VIEW.....	45
FIGURE 4.23: JOINT DESIGN COMPARISON USING TRADITIONAL (TOP) VERSUS NON-TRADITIONAL (BOTTOM) MANUFACTURING TECHNIQUES.....	46
FIGURE 4.24: LOST WAX INVESTMENT CAST BEVEL GEARS. THE BEARING SEATS ON THE FAR RIGHT PART HAVE BEEN TOUCHED UP. THE OTHER TWO PARTS ARE AS CAST.....	48
FIGURE 4.25: ELECTROPERMANENT MAGNET ASSEMBLY.....	50
FIGURE 4.26: ORIGINAL CONCEPT DRAWING FOR AN ELECTROPERMANENT MAGNETIC CLUTCH.....	50
FIGURE 4.27: PRELIMINARY DESIGN FOR AN ELECTROPERMANENT MAGNETIC CLUTCH (EPMC).....	51
FIGURE 4.28: HIGH-DEFINITION STEREOSCOPIC VISION SYSTEM (CARLSON ET AL.).....	52
FIGURE 4.29: INTEGRATION OF EB2.0 WITH THE HIGH-DEFINITION STEREOSCOPIC VISION SYSTEM (CARLSON ET AL.).....	53
FIGURE 4.30: 3-DIMENSIONAL VIEWING SYSTEM, MIRROR STEREOSCOPE ( <a href="http://www.3dfocus.co.uk/">HTTP://WWW.3DFOCUS.CO.UK/</a> ).....	54

FIGURE 4.31: SIZE COMPARISON OF EB2.0 AND A SINGLE ARM OF TB2.0. TOP LEFT: ISOMETRIC VIEW OF SIZE COMPARISON. TOP RIGHT: FRONT VIEW OF SIZE COMPARISON. BOTTOM: TOP VIEW OF SIZE COMPARISON. ....	55
FIGURE 4.32: CONCEPTUAL DIAGRAM OF THE DISTRIBUTED MOTOR CONTROL SYSTEM (BARTELS ET AL.). ....	56
FIGURE 4.33: BOARD LAYOUT FOR DISTRIBUTED MOTOR CONTROL SYSTEM V3, TOP: FRONT SIDE OF PCB, BOTTOM: BACK SIDE OF PCB.....	57
FIGURE 4.34: CROSS SECTION VIEW OF A POGO PIN. ....	59
FIGURE 4.35: DMCS V3 WITH THE POGO PIN PROGRAMMING HEADER JIG. ....	59
FIGURE 4.36: PROJECTION OF THE ROBOT ARM, R, ON TO THE YZ PLANE. ....	60
FIGURE 4.37: PLANAR ORIENTATION OF THE ROBOTIC ARM PROJECTED ON TO THE XR PLANE, WHERE PLANE R IS DEFINED AS THE PLANE THAT CONTAINS THE ROBOTIC ARM AND IS PERPENDICULAR TO THE YZ PLANE WITH AN ANGULAR OFFSET OF $\theta_1$ FROM THE XZ PLANE.....	61
FIGURE 4.38: REMOTE SURGEON USER INTERFACE FOR EB2.0.....	63
FIGURE 4.39: SUBSET OF INSERTION DEVICES THAT WERE DEVELOPED TO ALLOW NON-UNIFORM SHAPED DEVICES TO BE INSERTION INTO THE ABDOMINAL CAVITY UNDER INSUFFLATION. A: CANISTER TYPE DEVICE THAT EXTENDS THE PRESSURIZED ENVIRONMENT INTO THE CANISTER, ALLOWING THE SURGEON TO INSERT AND/OR REMOVE HIS/HER HANDS INTO THE PRESSURIZED ENVIRONMENT AND INSERT THE DEVICE UNDER INSUFFLATION; B, C, D: STANDALONE, CUSTOM INSERTION PORT THAT SEALS AGAINST NON-UNIFORM OBJECTS; E, F, G: DEPLOYMENT OF A 4-BAR-LINKAGE THAT ALLOWS THE OVERALL DIAMETER OF THE ARMS TO BE MINIMIZED FOR INSERTION, E, AND EXPAND ONCE FULLY INSERTED; F, G (FREDERICK ET AL.).....	65
FIGURE 4.40: CROSS SECTION VIEW OF THE INSERTION DEVICE FOR EB2.0. ....	66
FIGURE 4.41: INTRODUCTION OF EB2.0 INTO THE ABDOMINAL CAVITY THROUGH A 3 CM DIAMETER ACCESS PORT. A) ROBOTIC PLATFORM STORED WITHIN ACCESS PORT, B) & C) INSERTION OF THE ROBOTIC PLATFORM INTO THE ABDOMINAL CAVITY, D) ROBOTIC PLATFORM SECURED TO THE ABDOMINAL WALL BY MAGNET, READY FOR SURGICAL PROCEDURE TO BEGIN. THE ROBOTIC VISION SYSTEM AND COMMUNICATION AND POWER TETHER IS NOT SHOWN. ....	66
FIGURE 4.42: ARTICULATION OF EB2.0 FROM THE UPPER ABDOMINAL QUADRANT TO THE LOWER QUADRANT ABOUT A FULCRUM LOCATED AT THE ACCESS POINT. TOP: TOP VIEW, BOTTOM: SIDE VIEW. A VIDEO OF THE ARTICULATION CAN BE FOUND AT [59]. ....	67

FIGURE 0.1: EB2.0 MANIPULABILITY MEASURE, RIGHT ARM. ....	84
FIGURE 0.2: EB2.0 MINIMUM STATIC ENDPOINT FORCE, RIGHT ARM.....	84
FIGURE 0.3: EB2.0 STATIC ENDPOINT FORCE DEFICIENCIES IN THE X PRINCIPAL CARTESIAN AXIS, RIGHT ARM.....	85
FIGURE 0.4: EB2.0 STATIC ENDPOINT FORCE DEFICIENCIES IN THE Y PRINCIPAL CARTESIAN AXIS, RIGHT ARM.....	85
FIGURE 0.5: EB2.0 STATIC ENDPOINT FORCE DEFICIENCIES IN THE Z PRINCIPAL CARTESIAN AXIS, RIGHT ARM. ....	86
FIGURE 0.6: EB2.0 ENDPOINT VELOCITY DEFICIENCIES IN THE X PRINCIPAL CARTESIAN AXIS, RIGHT ARM. ....	86
FIGURE 0.7: EB2.0 ENDPOINT VELOCITY DEFICIENCIES IN THE Z PRINCIPAL CARTESIAN AXIS, RIGHT ARM.....	87

**LIST OF TABLES**

TABLE 3.1: AVERAGE FORCE DESIGN REQUIREMENTS.....	16
TABLE 3.2: AVERAGE VELOCITY DESIGN REQUIREMENTS.....	16
TABLE 4.1: EB2.0 OF JOINT LIMITS, RIGHT ARM. ....	26
TABLE 4.2: EB2.0 JOINT CHARACTERISTICS.....	28
TABLE 4.3: EB2.0 JOINT COST USING TRADITIONAL VERSUS NON-TRADITIONAL MANUFACTURING TECHNIQUES. ....	47

## Chapter 1: Introduction

General surgery was traditionally performed using a large open incision. This allowed the surgeon to directly manipulate the tissue with full visualization of the surgical site. In the last 50 years, there has been a large push towards minimizing invasiveness through techniques known as Minimally Invasive Surgery (MIS). There are many benefits to MIS including faster recovery time, reduced risk of infection, and improved cosmesis [1]. Laparoscopic surgery, a form of MIS, uses long rigid tools that are inserted through 3-5 small incisions in the abdominal wall. Some procedures, such as colon resection, may also require an additional larger incision of approximately 3-4 cm in size for specimen removal [2]. This type of MIS has been widely adopted for many routine procedures [3]. However, the complexity of the procedure is greatly increased due to the unintuitive control of long rigid tools coupled with diminished visual feedback and dexterity [4]. Most complex procedures are rarely done laparoscopically. Out of 300,000 colon resections performed in the United States annually, less than twenty percent are performed as laparoscopic procedures [5].

Natural Orifice Transluminal Endoscopic Surgery (NOTES) is a “scarless” form of MIS. NOTES takes advantage of a natural orifice, such as the esophagus, to access the peritoneal cavity. This form of MIS is particularly complex and requires specialized instruments that are generally sub-inch in diameter and flexible for atraumatic insertion through the natural lumen [6]. This form of MIS has a further reduction in risk of infection, faster recovery time, and improved cosmesis compared to laparoscopic MIS due to the elimination of all external incisions.

Laparo-Endoscopic Single Site (LESS) surgery is a form of MIS that takes advantage of a preexisting scar within the umbilicus. LESS surgery has been seen as a viable bridge to NOTES [7]. However, this method is not as complex as NOTES but is inherently limited in visualization and triangulation due to the constraints of working through a single access port. LESS surgery often requires specialized bent and/or articulating surgical tools and multi-lumen ports. These specialized tools are frequently crossed at the incision site for improved triangulation, requiring extensive training. This advanced form of MIS has additional benefits over laparoscopic MIS such as improved patient cosmesis, reduced hospital stay, and reduced cost [5], [8].

A completely insertable *in vivo* robotic prototype has been developed to address some of the limitations seen with manual tools during LESS procedures. LESS is an attractive minimally invasive technique for complex procedures such as colon resection which require a 3-4 cm incision for anastomosis and specimen removal [2]. The miniature *in vivo* robotic device that has been developed can be inserted through a small incision in the umbilicus. The device has two dexterous four-degree-of-freedom (4-DOF) arms with interchangeable end-effectors. This system offers access to each of the four abdominal quadrants, improved visualization and triangulation, and more intuitive control. An example of this system is shown in Figure 1.1.

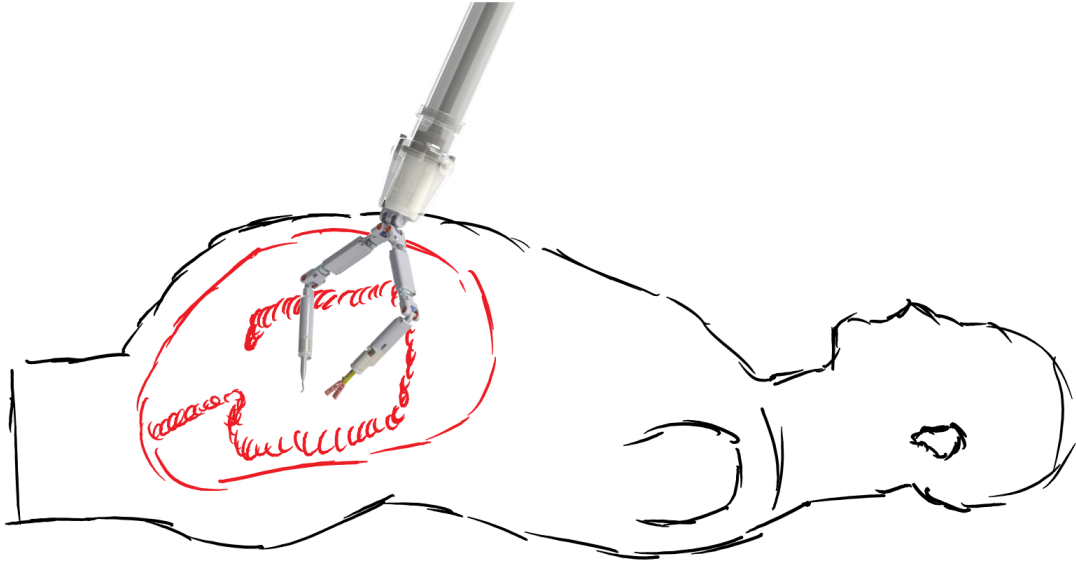


**Figure 1.1: Miniature *in vivo* Surgical Robot.**

This thesis presents the design and development of a miniature *in vivo* surgical robot with distributed motor control for LESS surgery. The device, motor control system, and insertion device will be examined. In addition, this system will be compared to predicate devices and future work will be discussed.



## **Chapter 2: Background**

### ***Section 2.1: Minimally Invasive Surgery***

#### ***Section 2.1.1: Laparoscopic Surgery***

Through technological breakthroughs, traditional open surgeries were slowly shifting to laparoscopic procedures throughout the late 1980s and early 1990s [9], [10]. Laparoscopic surgery began to replace the large open incision with 3-5 small incisions of approximately 5-12 mm in diameter. Specialized single-lumen ports called trocars are inserted into each of the small incisions. These ports allow the peritoneal cavity to be insufflated without loss of pressure [5]. Trocars allow surgical tools such as a needle driver, grasper, and laparoscope to be inserted interchangeably between all of the available ports. Although laparoscopic surgery is more difficult than traditional methods, the benefits to patients have helped it to become a very popular form of MIS [6]. Surgical instruments for laparoscopic surgery are typically rigid and vary from 5-12 mm in diameter and 25-45 cm long.

#### ***Section 2.1.2: Natural Orifice Transluminal Endoscopic Surgery (NOTES)***

Natural Orifice Transluminal Endoscopic Surgery (NOTES) is an advanced form of MIS which eliminates all external incisions. NOTES was originally envisioned as the predecessor to laparoscopy. There are many benefits to the patient if the peritoneal cavity is accessed through a natural orifice. Kalloo *et al.* were the first to demonstrate the feasibility of NOTES during an animal model study [6]. Additional feasibility studies have

followed and successful NOTES procedures have been performed on humans [11]. However, this form of MIS has proven to be too difficult with the current state-of-the-art tools to be widely adopted. Surgical tools that are used via a natural orifice are typically based on a flexible scope with a working channel for mm-size tools.

### ***Section 2.1.3: LaparoEndoscopic Single-Site (LESS)***

#### ***Surgery***

LaparoEndoscopic Single-Site (LESS) surgery is a more realistic evolution of MIS. LESS surgery is a technique that involves placing all instruments through a single access point. This 20-35 mm incision is typically made at the umbilicus, a preexisting scar. This advanced form of MIS improves upon patient benefits, compared to laparoscopic surgery, such as patient cosmetics, hospital stay, and cost [5], [8]. A specialized multi-lumen port is used to provide access to the surgical site. Articulated tools, which are generally crossed at the access point, enhance the capabilities of the surgeon and allow them to approach the surgical site from different angles. These tools help to restore some of the triangulation and visualization that is lost while maximizing range of motion and minimizing internal and external crowding. While LESS surgery is more difficult, multiple procedures have been performed in humans including cholecystectomies, appendectomies, splenectomies, nephrectomies, and colectomies [12], [13].

### ***Section 2.2: Robotic Minimally Invasive Surgery***

### ***Section 2.2.1: Robotic Laparoscopic Surgery***

As the fields of medicine and robotics have advanced, there has been an increase in interest in using robotics to improve surgical outcomes [14]. Surgical robots offer many advantages over traditional tools such as intuitive control, improved ergonomics, and increased precision. The Automated Endoscopic System for Optimal Positioning (AESOP) was the first clinically used surgical robot [15]. AESOP was a robotic endoscopic camera assistant that provided a stable view of the surgical site and could be repositioned via voice control. It was the first Food and Drug Administration (FDA) approved surgical robot, achieving approval in 1994.



**Figure 2.1: The *da Vinci*® Surgical System, model Xi (©2014 Intuitive Surgical, Inc.)**

At this time, the *da Vinci*® Surgical System (Intuitive Surgical, Sunnyvale, CA) is the most advanced commercially available robotic system for general surgery. The newest

model, the *da Vinci*® Xi Surgical System, is shown in Figure 2.2. The surgical system improves upon dexterity and visualization through the use of stereoscopic vision and specialized EndoWrist® laparoscopic instruments. Other improvements include motion scaling, tremor reduction, intuitive control, and telerobotic operation [16]–[18]. The surgeon operates the robot from a remote user interface while the surgical system is positioned above the patient at the operating table. Some of the limitations of previous versions of the *da Vinci*® Surgical System include repositioning, robot arm collisions, crowding of the surgical site, size, and high cost [18], [19]. Complex surgical procedures, such as colon resection, often require multiple access positions. This is often seen with traditional laparoscopy as well. For example, a sigmoid colectomy would require the robotic cart of the *da Vinci*® Surgical System to be positioned in two different locations as shown in Figure 2.2. The task of undocking from the first location and docking to the new location is a timely, costly process. Repositioning of the robotic cart provides improved triangulation and visualization of the surgical target. Some of these concerns have been addressed with the new system [20]. The improvements include an overhead boom that will help to facilitate fast 4-quadrant surgery and free up space within the surgical field to allow unobstructed access to the patient. However, this system still faces some of the downfalls of traditional laparoscopy including limited workspace and degradation or complete loss of haptic feedback.

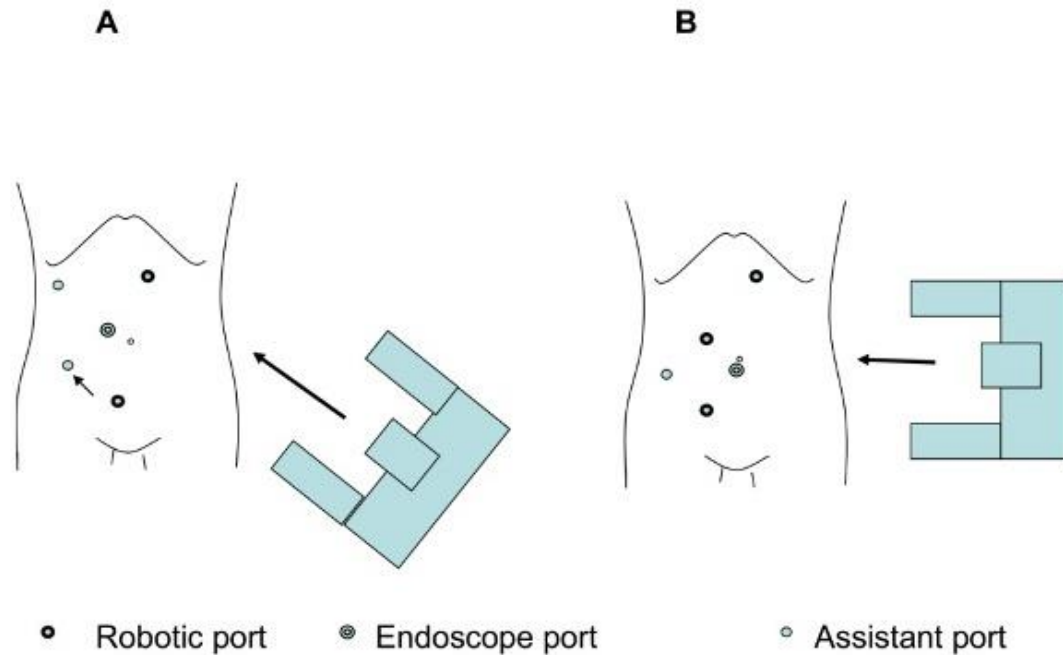


**Figure 2.2:** The location of the ports and robotic cart for a robotic assisted sigmoid colectomy: A) The lower left oblique location of the robotic cart, B) The left vertical location of the robotic cart. (Baik et al.)

Other researchers are also actively pursuing the area of surgical endoscopy. Research platforms include CoBRASurge [21], Raven [22], Mirosurge [23], and CURES [24]. These systems have been developed to combat the high price and large size of the *da Vinci*® surgical system. Although these systems are smaller and less expensive than the *da Vinci*® surgical system, they are still limited by the constraints of the access point. Mirosurge has partially improved upon its predecessors by restoring the sense of touch to the surgeon through the use of a force/torque sensor at the tool's end-effector and haptic interface [25].

### ***Section 2.2.2: Robotic NOTES (R-NOTES)***

Research is also being conducted towards the realization of NOTES. One example of this type of robotic platform was developed by Rentschler et al. as described in [26].

Once the device is inserted into the peritoneal cavity through a natural lumen, helical drive wheels are used to traverse the abdominal cavity. The modular devices can be equipped with various types of end-effectors to provide surgical assistance [27]. These devices are inexpensive and can be easily transported. Another example of R-NOTES devices include those developed by Nelson et al. as described in [28]–[30]. These device are tubular in shape and include steerable and articulating snake like mechanisms, material handlers, and tool changing mechanisms. Although, there has been success with simple R-NOTES procedures, more complex operations will require additional dexterity and workspace than what current platforms provide. R-NOTES devices will need to be further developed before they will be considered clinically viable.

### ***Section 2.2.3: Robotic LESS Surgery (R-LESS)***

LaparoEndoscopic Single-Site (LESS) surgery is considered a more realistic evolution for MIS robotic platforms. Both companies and research groups are actively performing research in this area. Intuitive Surgical has developed two types of single-port systems. The first uses curved cannulas to improve dexterity and triangulation, shown in Figure 2.3. Although capable, the adoption of this system has been limited due to the external arms of the system colliding together [31]. The most recent FDA approved single-port robotic system, the *da Vinci*® Sp™ Surgical System, delivers an articulating 3D camera along with three fully articulating EndoWrist® instruments through a single 25-mm cannula, shown in Figure 2.4, [32]. This system is not yet commercially available but is projected to be compatible with the *da Vinci*® Xi Surgical System.

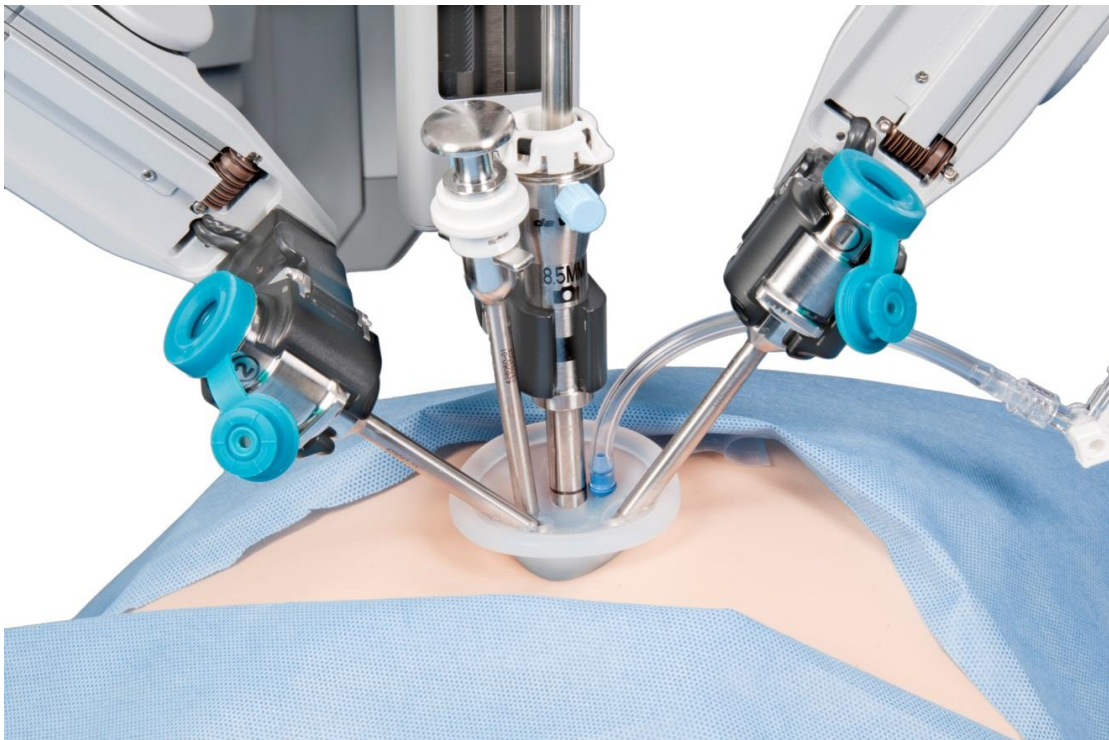


Figure 2.3: The *da Vinci*® system set up to perform an R-LESS procedure using curved cannulas (©2014 Intuitive Surgical, Inc.)

In addition to the commercially available R-LESS systems, numerous research groups are attempting to create a miniature *in vivo* surgical robot that places some or all of the actuators inside of the peritoneal cavity. Dario et al. have developed a Single-Port lapaRoscopy bImaNual roboT (SPRINT), [33]. This bi-manual robot has two six-DOF arms with end-effectors. Each arm is 18 mm in diameter and is designed to be inserted individually through a single 30 mm diameter cannula. The device is controlled via a haptic interface device. Only 4 of the 6 positional DOFs per arm are actuated by *in vivo* motors. The two proximal DOFs and the end-effectors' open/close actuation are externally actuated. These external DOFs constrain the device to the location of the access point.



**Figure 2.4: The *da Vinci*® Sp™ Surgical System (©2014 Intuitive Surgical, Inc.)**

The Advanced Surgical Technologies Laboratory at the University of Nebraska-Lincoln has been developing *in vivo* surgical devices since the early 2000s. The group has developed various types of platforms such as magnetically mounted imaging robots, two-wheeled mobile robots, and rigidly mount single-port robotic devices [34]–[42]. The most recent developments have been two-armed miniature *in vivo* surgical robots for use in R-LESS procedures. These multi-functional devices can be inserted through a single incision to perform general surgical procedures within multiple quadrants of the peritoneal cavity. Successful *in vivo* procedures include colectomies, cholecystectomies, and a hysterectomy [43]. This thesis will present a new, miniaturized version of the predicate devices with distributed motor control and a device that will allow the robot to be inserted into the abdominal cavity under insufflation, shown in Figure 2.5.



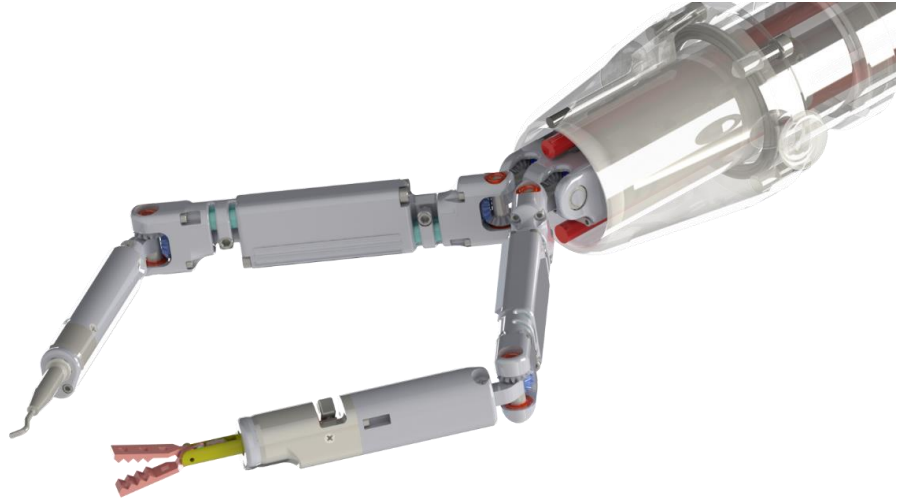


**Figure 2.5: EB2.0 Design**

## Chapter 3: Motivation

### *Section 3.1: Overview*

Single-port surgery has many benefits but is inherently difficult due to the constraints of a single access point. Dexterous *in vivo* robotic platforms aim to replace standard laparoscopic tools, while improving the standard of care. The basic robot design consists of two arms that can be inserted together or individually through a single small incision. Once inserted, only a central rod is protruding from the insertion site. This rod allows the robot to be rigidly supported to the operating table or grossly positioned, if needed. For NOTES applications this central rod would be replaced by a magnetic handle that would affix the device to the wall of the abdominal cavity.

Each arm is designed to meet or exceed the capabilities of traditional laparoscopic tools. The device can be completely inserted into the abdominal cavity under insufflation using a custom insertion device. Since the device is completely inserted into the cavity there are no kinematic restrictions due to the access point. The device is designed to have two symmetric arms, similar to the kinematics of the left and right arms of a human. Each arm of this device is designed to have four degrees of freedom with open/close actuation of the end-effectors. Each arm consists of a 'Torso', 'Upper arm', and 'Forearm'. The symmetric arms have a 2-DOF shoulder joint, a 1-DOF elbow joint, and a 1-DOF rotation of the end-effector. The end-effector's rotational DOF is decoupled and has no effect on the Cartesian positioning of the end-effector. Each arm can be independently controlled using a set of haptic controllers. Video feedback is provided to the surgeon by a traditional endoscope or custom stereoscopic camera pair.

## ***Section 3.2: Design Requirements***

A number of factors should be considered when developing *in vivo* surgical robots. Some of these factors include: force, velocity, dexterity, workspace, and size. The robotic device must have adequate force, velocity, and dexterity to perform surgical procedures. It must also have a large enough workspace to complete the surgical procedure. Robotic workspace can be defined as the volume that the device can reach. Because this device has multiple manipulators, the union of the two arms' workspaces will be considered the workspace of the entire device. The intersection of the two arms' workspaces must be maximized to allow the arms to cooperatively complete surgical tasks throughout a large volume of the entire workspace. A large workspace also prevents the need for the robot to be grossly repositioned multiple times during a surgery. However, coupling such a device with a robotic gross positioning system may be beneficial [44].

It is difficult to quantify forces and speeds required to manipulate tissue and perform surgical tasks because of the preliminary stage of this type of device. Currently, the most prevalent available data is from laparoscopic procedures. BlueDRAGON recorded the forces directly applied to the tool handle by the surgeon. Due to the unknown interference with the access point, it is impossible to accurately determine the applied tissue force. However, it can be safely assumed that the required forces are not higher than the reported forces that were applied to the tool handle. The BlueDRAGON, developed by the BioRobotics Lab at the University of Washington, was used to measure forces and speeds of various surgical procedures [45]–[47]. The raw data from these studies found that forces applied along the axis of the tool were on the order of 20 N, while forces applied perpendicular to the axis of the tool were on the order of 5 N. This dataset was further

analyzed to determine the velocity design specifications for a spherical robotic manipulator. From the raw data, the calculated angular velocities for the axes perpendicular to the laparoscopic tool were 0.432 rad/sec and 0.486 rad/sec, while the angular velocity around the axis of the tool was 1.053 rad/sec. The linear velocity along the axis of the tool was 72 mm/sec. From the reported approximate tool length of 100-150 mm, the upper limit of the velocity design requirement can be approximated.

Another study was completed in an open-surgery setup that recorded the force needed to stretch the mesocolon for dissection [48]. For this study, clamps were applied to the mesocolon in series with a spring scale. The surgeon then applied tension to the sigmoid mesocolon at an angle of approximately 60 degrees relative to horizontal. The average pull force per clamp was  $1.9 \pm 0.6$  N, with a maximum of 3.1 N. Using the data from this study, Lehman et al. assumed that the remainder of the applied forces was evenly distributed between the remaining axes [35]. The summarized force and velocity design requirements are shown in Table 3.1 and Table 3.2.

Predicate devices have demonstrated that a two-armed miniature *in vivo* surgical robot is a feasible method for performing surgical procedures. They have also demonstrated that such devices can be inserted through a single incision and be grossly positioned throughout the abdominal cavity through the use a protruding rod [43], [49].

The most recent predicate devices have two arms that are introduced individually into the abdominal cavity to reduce the necessary size of the access incision. This type of insertion technique would be a cumbersome task to complete during a NOTES procedure. Lehman et al. developed a device that would become flexible for insertion through a natural

orifice and could be grossly positioned throughout the abdominal cavity using a magnetic handle [50]. However, this device required minor assembly once inside the abdominal cavity.

**Table 3.1: Average Force Design Requirements**

Force Direction	Value (N)
$F_x$	0.8
$F_y$	0.8
$F_z$	2.2

**Table 3.2: Average Velocity Design Requirements**

Rotational Velocity	Value (mm/sec)
$V_x$	70
$V_y$	70
$V_z$	72
$\omega_{Grasper}$	1.053 rad/sec

From these observations a list of requirements were derived: 1) the device should be developed such that a protruding rod or magnetic attachment system could be used to grossly position the robotic platform, 2) the two arms of the robotic device should be permanently coupled together to ease the insertion process, 3) following introduction into the cavity no additional steps should be required by the surgeon except for gross

positioning, and 4) force and speed requirements should be met, as set forth in Table 3.1 and Table 3.2, through a large area of the robotic workspace.

## Chapter 4: Eric-Bot 2.0 System Description

The Advanced Surgical Technologies Lab at the University of Nebraska-Lincoln has developed numerous iterations of multi-functional two-armed *in vivo* surgical robots. The first generation of devices were developed specifically for NOTES applications. These devices were compact with at most three-DOFs per arm and lacked position control. The next generation of devices were designed specifically for LESS surgery. The simplified access to the abdominal cavity allowed the number of DOFs to be increased with larger motors equipped with encoders for position control. These changes allowed the devices to complete more advanced surgical procedures. The first of these devices were too large to be inserted into the abdominal cavity through a 20-35 mm incision. However, these original devices validated that a miniature, two-armed surgical robot was capable of performing complex surgical procedures. The second generation of this type of device, specifically designed for LESS surgery, have been composed of two arms that are individually inserted into a non-insufflated abdominal cavity. Once inserted, the two arms are assembled together and secured via a central insertion rod. This rod protrudes from the incision site and can be rigidly attached to the operating table. A specialized gel port is used to create a seal between the abdominal incision and the insertion rod.

Eric-Bot 2.0 (EB2.0) is a two-armed multi-quadrant robotic platform that has been developed for LESS surgery. This platform is based on previous research from our group and can be used as a stepping stone towards NOTES. EB2.0 was designed to eliminate the need for additional assembly tasks once inserted into the abdominal cavity. In addition, the device is equipped with a distributed motor control system and custom insertion device

that allows insufflated insertion into the abdominal cavity. The progression of surgical devices from the Advanced Surgical Technologies Lab is shown in Figure 4.1.

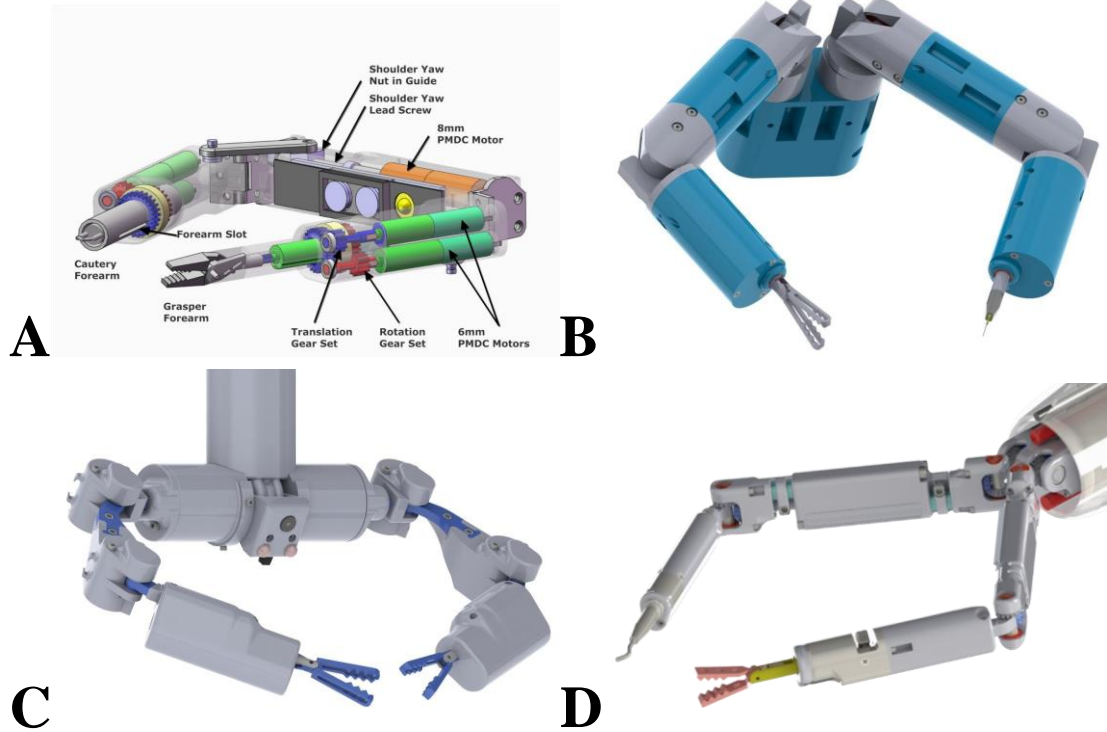


**Figure 4.1:** Evolution of miniature *in vivo* surgical devices from the Advanced Surgical Technologies Lab at the University of Nebraska-Lincoln. A) First generation of surgical devices developed for NOTES (Lehman et al.), B) First generation of surgical devices developed for LESS surgery (Wood et al.), C) Second generation of surgical devices developed for LESS surgery (Wortman et al.), D) EB2.0 third generation of surgical devices developed for LESS surgery.

## Section 4.1: Kinematic Model

A kinematic model of the right arm of EB2.0 is shown below in Figure 4.2. The base frame {0}, not shown, is -6 mm along the X axis from frame {1}. The plane of symmetry is located at (0, 0, 0) parallel to the YZ plane. Frames {1} and {2} are located at the shoulder of the device between the torso and upper arm. Frame {3} is located at the elbow joint between the upper arm and forearm. Frame {4} is located at the tip of the end-



effector. The degrees of freedom as shown on the actual device with corresponding link/body naming convention are shown in Figure 4.3.

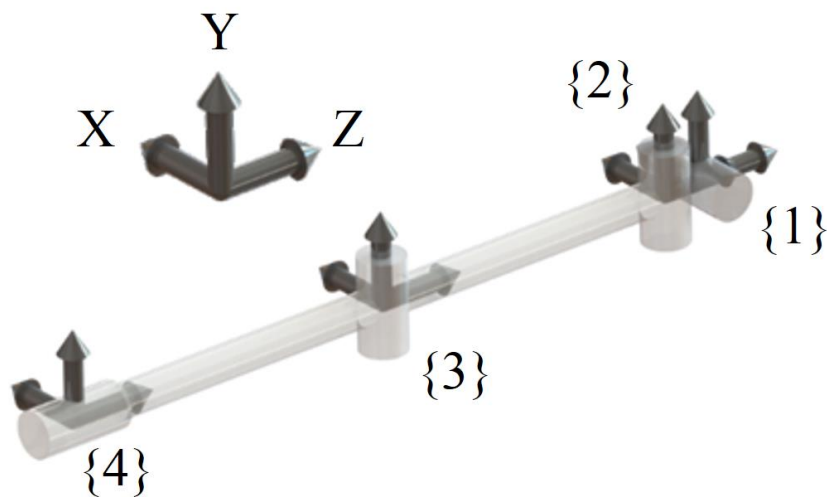


Figure 4.2: Kinematic model of EB2.0. Frame {1} is located at (6, 0, 0) [mm].

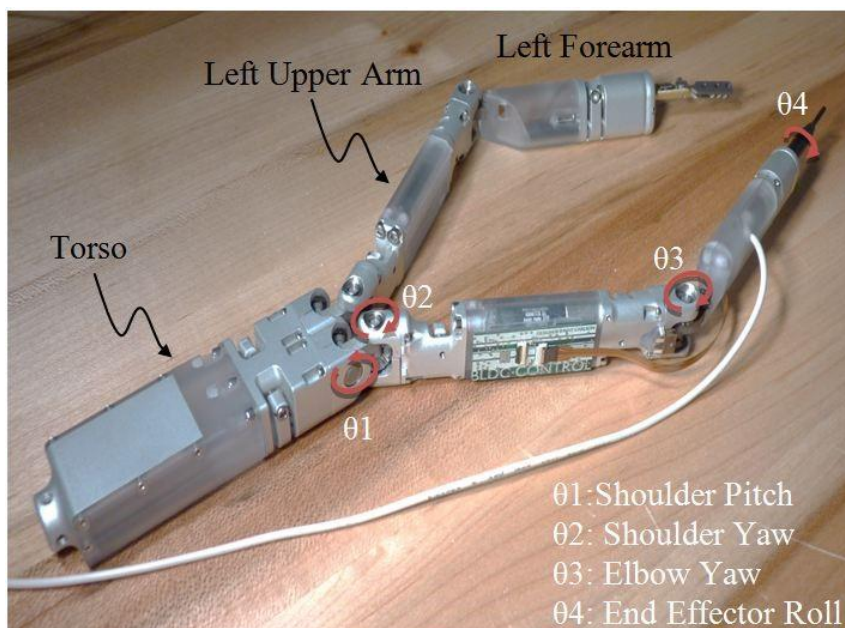
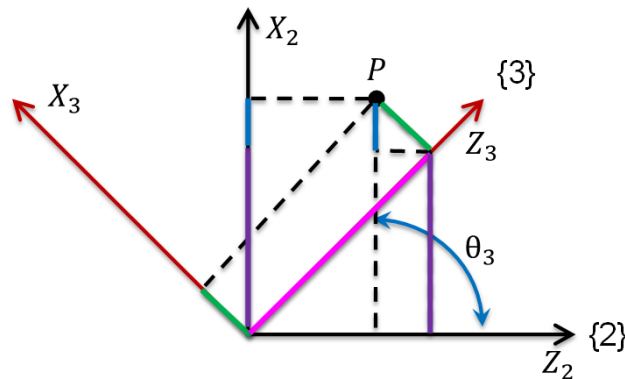


Figure 4.3: EB2.0 with labeled degrees of freedom and link naming convention.

### Section 4.1.1: Forward Kinematics

Using the kinematic model, the transformation matrixes between frames can be derived. A transformation matrix is used to describe the location of frame {i} relative to the previous frame {i-1} [51]. The derivation of the transformation matrix between frames {2} and {3} is shown in Figure 4.4. Traditionally, the Denavit-Hartenberg (DH) notation is used to affix reference frames to the links of a robotic manipulator [51]. Each link is summarized by 4 link parameters. These parameters can be used to derive the transformation matrixes between frames or construct the original kinematic model. However, the DH notation often results in multiple solutions. Based on the simplicity of the model and to eliminate any uncertainty a geometric method was used.



$$\begin{aligned} X_2 &= X_3 \cos(\theta_3) + Z_3 \sin(\theta_3) \\ Z_2 &= -X_3 \sin(\theta_3) + Z_3 \cos(\theta_3) \end{aligned}$$

$${}^2_3R = \begin{bmatrix} C_3 & 0 & S_3 \\ 0 & 1 & 0 \\ -S_3 & 0 & C_3 \end{bmatrix}$$

$${}^2_3P = \begin{bmatrix} 0 \\ 0 \\ -87.5 \end{bmatrix}$$

$${}^{i-1}_i T = \begin{bmatrix} {}^{i-1}_i R & {}^{i-1}_i P \\ 0 & 1 \end{bmatrix}$$

Figure 4.4: Derivation of the transformation matrix between frames {2} and {3}.

Equations  $X_2$  and  $Z_2$  can be written solving for point P, while only using variables  $X_3$ ,  $Z_3$ , and  $\theta_3$ .  $\theta_3$  is defined as the positive rotation between frames {2} and {3}. Matrix R is the rotation matrix that is populated using equations  $X_2$  and  $Z_2$ . Matrix P is the vector from frame {2} to frame {3}. A transformation matrix can be formed using Equation 4-1.

Equation 4-1

$${}^{i-1}T_i = \begin{bmatrix} {}^{i-1}R_i & {}^{i-1}P_i \\ 0 & 1 \end{bmatrix}$$

The forward kinematics of the right arm of the robot can be constructed by multiplying all of the transformation matrices together in order from  ${}^0T_1$  to  ${}^{n-1}T_n$ . Following the derivation described above the following transformation matrices were formed:

$${}^0T_1 = \begin{bmatrix} 1 & 0 & 0 & 0 \\ 0 & C_1 & -S_1 & 0 \\ 0 & S_1 & C_1 & 0 \\ 0 & 0 & 0 & 1 \end{bmatrix}$$

Equation 4-2

$${}^1T_2 = \begin{bmatrix} C_2 & 0 & S_2 & 0 \\ 0 & 1 & 0 & 0 \\ -S_2 & 0 & C_2 & -L_0 \\ 0 & 0 & 0 & 1 \end{bmatrix}$$

Equation 4-3

$${}^2T_3 = \begin{bmatrix} C_3 & 0 & S_3 & 0 \\ 0 & 1 & 0 & 0 \\ -S_3 & 0 & C_3 & -L_1 \\ 0 & 0 & 0 & 1 \end{bmatrix}$$

Equation 4-4

$${}^3T_4 = \begin{bmatrix} 1 & 0 & 0 & 0 \\ 0 & 1 & 0 & 0 \\ 0 & 0 & 1 & -L_2 \\ 0 & 0 & 0 & 1 \end{bmatrix}$$

Equation 4-5

where  $C_n = \cos(\theta_n)$ ,  $S_n = \sin(\theta_n)$ ,  $L_0 = 10.7$  mm,  $L_1 = 87.5$  mm, and  $L_2 = 95.3$  mm.

The Cartesian coordinates corresponding to the forward kinematics of the robot can be extracted from the single transformation matrix that is formed by multiplying all of the transformation matrices together. The extracted forward kinematics, matrix P, of EB2.0 is shown below in Equation 4-6, Equation 4-7, and Equation 4-8.

$$X = -L_2(C_2S_3 + S_2C_3) - L_1S_2$$

Equation 4-6

$$Y = L_2(S_1C_2C_3 - S_1S_2S_3) + L_1S_1C_2 + L_0S_1$$

Equation 4-7

$$Z = -L_2(C_1C_2C_3 - C_1S_2S_3) - L_1C_1C_2 - L_0C_1$$

Equation 4-8

### ***Section 4.1.2: Workspace***

The entire workspace of the robotic device is defined as the union of the reachable workspace of the right and left arm of the robotic prototype. Robotic workspace can be defined as the volume that the manipulator can reach. The workspace can be mathematically found using the forward kinematics and joint limits. However, for this device if  $\theta_1$  is removed, it becomes a planar device. Therefore, the workspace of the device can be found by tracing the minimum and maximum reach of the planar device and revolving this trace about the axis of  $\theta_1$ . The workspace of the planar device is shown in Figure 4.5. The area of a single slice within the prototype's workspace is  $305.0 \text{ cm}^2$ . The volume of the entire workspace is  $7431.2 \text{ cm}^3$ .



**Figure 4.5: EB2.0 superimposed on top of a slice of the entire robotic workspace at  $\theta_1 = 0$  degrees.**

The intersecting workspace of the surgical robot is very important. Tasks such as suturing, dissection, and tissue manipulation often require the arms to cooperatively complete these surgical tasks. The intersecting workspace of the planar device and the intersecting workspace volume of EB2.0 are shown in Figure 4.6. The area of a single slice within the prototype's intersecting workspace is  $142.7 \text{ cm}^2$ , accounting for 46.8% of the entire workspace. The volume of the intersecting workspace is  $3838.2 \text{ cm}^3$ .



**Figure 4.6:** Left: EB2.0 superimposed on top of a slice of the intersecting robotic workspace at  $\theta_1 = 0$  degrees. Right: EB2.0 with the intersecting workspace of the device.

The previous workspace plots were formed using the joints limits shown in Table 4.1. The specific design of each joint will be discussed in detail within Chapter 4, Section 4.2. In addition,  $\theta_2$  was limited to 0 degrees in the positive rotational direction to eliminate collisions between the upper arms and  $\theta_3$  was limited to 0 degrees in the negative rotational direction to prevent the device from passing through a singularity. Based on intelligent interference control, the joint range of  $\theta_2$  could be increased to 35 to -90 degrees, listed as  $\theta_{2, \text{alternative}}$  in Table 4.1. Using  $\theta_{2, \text{alternative}}$  the workspace and intersecting workspace would be increased by 40.8% and 45.8% respectively. The area of the entire workspace is 429.6  $\text{cm}^2$ , while the intersecting workspace accounts for 208.1  $\text{cm}^2$ . The increased workspace and intersecting workspace are shown in Figure 4.7. The original intersecting workspace is also shown for comparison.

Table 4.1: EB2.0 of joint limits, right arm.

Joint	Range (Degrees)	Positive Rotation
$\theta_1$	45 to -80	-Z to Y
$\theta_2$	0 to -90	Z to X
$\theta_{2, \text{alternative}}$	35 to -90	Z to X
$\theta_3$	0 to 135	Z to X

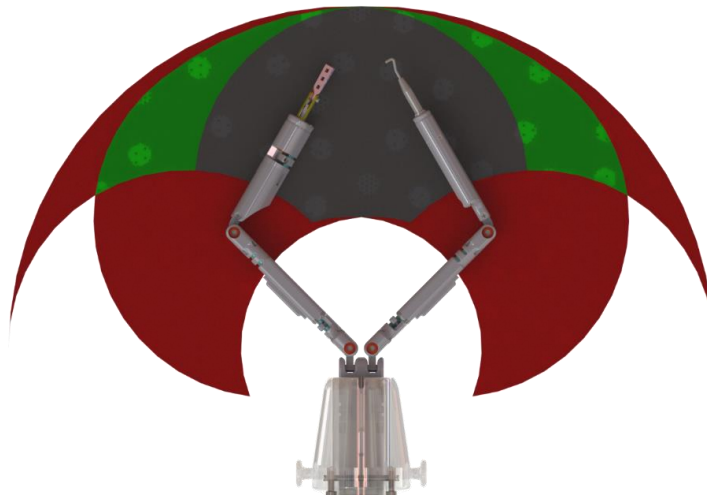


Figure 4.7: EB2.0 superimposed on top of a slice of the entire robotic workspace at  $\theta_1 = 0$  degrees. Black: original interesting workspace, Green + Black: interesting workspace using  $\theta_{2, \text{alternative}}$ , Green + Black + Red: robotic workspace using  $\theta_{2, \text{alternative}}$ .

The area of the entire workspace of the most recent previously developed miniature *in vivo* surgical robot, TB2.0, is  $169.5 \text{ cm}^2$ , while the intersecting workspace accounts for  $52.7 \text{ cm}^2$ . Ignoring  $\theta_{2, \text{alternative}}$  the entire workspace of EB2.0 is 79.9% larger, while the intersecting workspace is 170.8% larger.

### ***Section 4.1.3: Jacobian Matrix***

The Jacobian matrix is the first order partial derivative of the forward kinematics. This matrix is used to study both velocities and static forces of robotic manipulators [51]. The Jacobian matrix written in vector notion from frame {0} is shown in Equation 4-9.

**Equation 4-9**

$${}^0J(\theta) = \frac{\delta(X, Y, Z)}{\delta\theta}$$

In the case of the present robotic prototype,  $\theta_4$  can be ignored when calculating the Jacobian matrix. This DOF does not affect the position of the end-effector and is decoupled from the system. Therefore, a 3 X 3 Jacobian matrix for EB2.0 can be formed, shown in Equation 4-10. The matrix was calculated using MAPLE (Maplesoft, Waterloo, ON). The code used to calculate the Jacobian matrix can be found in Appendix A.

**Equation 4-10**

$${}^0J(\theta) = \begin{bmatrix} 0 & -(C_2C_3 - S_2S_3)L_2 - C_2L_1 & -(C_2C_3 - S_2S_3)L_2 \\ -(C_1S_2S_3 - C_1C_2C_3)L_2 + C_1C_2L_1 & -(S_1S_2C_3 - S_1C_2S_3)L_2 - S_1S_2L_1 & -(S_1S_2C_3 + S_1C_2S_3)L_2 \\ -(S_1S_2S_3 - S_1C_2C_3)L_2 + S_1C_2L_1 & (C_1S_2C_3 + C_1C_2S_3)L_2 + C_1S_2L_1 & (C_1S_2C_3 + C_1C_2S_3)L_2 \end{bmatrix}$$

where  $C_n = \cos(\theta_n)$ ,  $S_n = \sin(\theta_n)$ ,  $L_0 = 10.7$  mm,  $L_1 = 87.5$  mm, and  $L_2 = 95.3$  mm

The determinant of the Jacobian matrix can be analyzed to determine the singularities of the device, expressed in Equation 4-11. A singularity of EB2.0 exists when  $\theta_3 = 0$  degrees. In this configuration, motion of the end-effector is possible along only two Cartesian directions, the directions perpendicular to the arm. The mechanism has lost one DOF in this configuration. This type of singularity is classified as a workspace-boundary



singularity because it only exists at the edge of the manipulator's workspace. A singularity can also arise if the angular velocity or torque approaches infinity.

$$DET[J(\theta)] = 0$$

Equation 4-11

### ***Section 4.1.4: Theoretical Abilities***

Brushless DC motors with integrated planetary gearheads and Hall effect sensors were used throughout the robotic prototype. Brushless DC motors have many advantages over brushed DC motors such as increased lifespan, high efficiency, low electrical noise, and improved heat dissipation. In addition, brushless motors can be sterilized which would be required for FDA approval. Some companies, such as Maxon Motor, offer brushless motor options that are rated up to at least 100 autoclave cycles [52]. However, brushless DC motors sometimes require complex and expensive control systems. The motor specifications for each joint are shown in Table 4.2. The specific joint design and motor selection is discussed in detail within Chapter 4, Section 4.2.

**Table 4.2: EB2.0 joint characteristics.**

Joint	Stall Torque, $\tau_s$ (mNm)	No-Load Speed, $\omega_{nl}$ (rpm)	Internal Gearhead, $N_I$	Efficiency, $\eta$ (%)	External Reduction, $N_E$
$\theta_1$	1.63	45,600	256:1	65	1:1
$\theta_2$	0.73	46,500	1024:1	55	8:5
$\theta_3$	0.73	46,500	1024:1	55	8:5
$\theta_4$	0.73	46,500	256:1	55	7:5
$\theta_5$ , Grasper	0.73	46,500	256:1	55	2:1

As previously stated, the Jacobian matrix can be used to find the end point velocities and static forces of robotic manipulators. The relationship that relates joint torques to static endpoint forces and angular velocities to endpoint velocities is shown in Equation 4-12 and Equation 4-13 respectively. Based on the knowledge of the theoretical motor capabilities the theoretical endpoint capabilities can be derived across the workspace of the prototype.

$$\tau = {}^0J^T(\theta) {}^0\mathcal{F} \quad \text{Equation 4-12}$$

$${}^0v = {}^0J(\theta)\dot{\theta} \quad \text{Equation 4-13}$$

#### ***Section 4.1.4.1: Manipulability***

The Jacobian matrix can also be used to determine the dexterity of a robotic manipulator. Yoshikawa used the Jacobian matrix to determine the dexterity of a manipulator by defining the manipulability measure,  $\omega$ , [53]. The manipulability measure is defined in Equation 4-14.

$$\omega = \sqrt{\det(J(\theta)J^T(\theta))} \quad \text{Equation 4-14}$$

The manipulability of EB2.0 was calculated across the workspace of the right arm. These results were normalized and plotted in MATLAB® (Mathworks®, Natick, MA) using the surface function, shown in Figure 4.8. The value 1 represents the highest manipulability while 0 represents the lowest. The code that was used to calculate and plot the manipulability measure across the workspace and the original plot can be found in Appendix B.

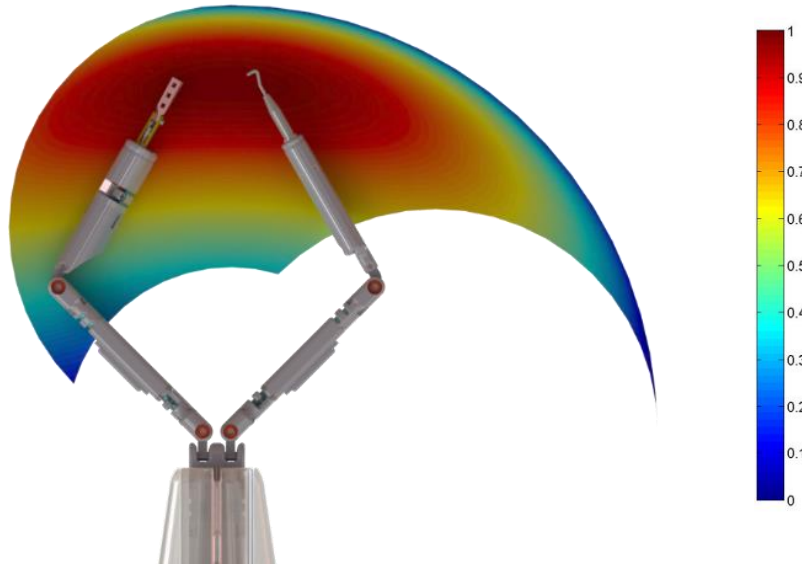


Figure 4.8: EB2.0 manipulability measure, right arm.

#### *Section 4.1.4.2: Forces*

Using Equation 4-12 and known joint torques from Table 4.2, the static endpoint forces can be found along each of the principal Cartesian axes. The theoretical joint torques can be calculated using Equation 4-15.

**Equation 4-15**

$$\tau = \eta \cdot \tau_s \cdot N_I \cdot N_E$$

Once the maximum individual joint torques were found, the theoretical static endpoint force in each Cartesian direction was calculated and plotted across the workspace. The results were plotted using the surface function in MATLAB®, as shown in Figure 4.9. The code that was used to calculate and plot the static endpoint force in each principal Cartesian axis can be found in Appendix B.

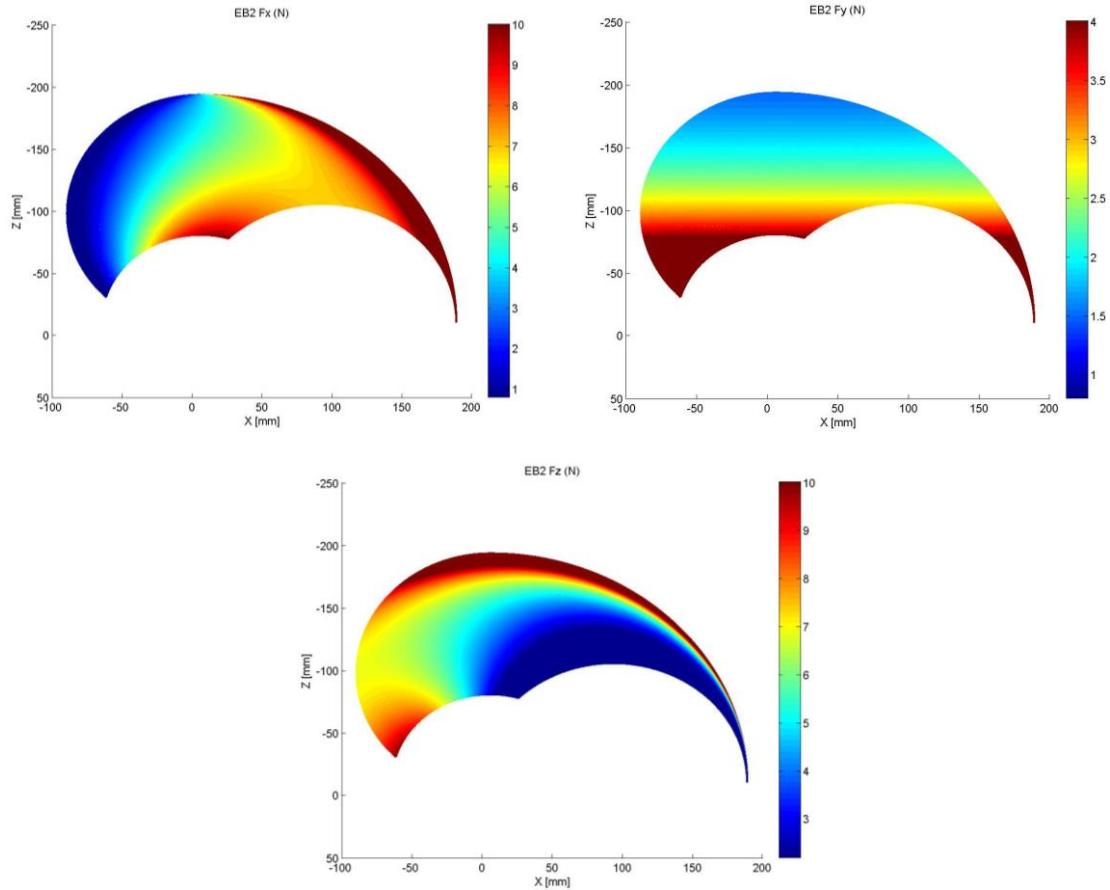


**Figure 4.9: EB2.0 static endpoint force in each principal Cartesian axis, right arm (Please note that the force scale for each individual plot is different: Fx: 10-0.8 [N], Fy: 4-0.8 [N], Fz: 10-2.2 [N]).**

This analysis assumes no gravity and massless arms. While not exact, the values found are a reasonable estimation of the prototype's abilities. At the worst case scenario, when the arm is positioned parallel to the negative-Z axis, the torque,  $\tau_g$ , required to compensate for gravity is showed in Equation 4-16. This compensation accounts for approximately 3.5% of the maximum intermittent torque allowed by the gearhead of the 10-mm Maxon motor. At the worst case scenario, when the insertion rod is perpendicular to the operating table and the arm is parallel to the X axis, gravity accounts for approximately 18% and 4.9% of the maximum intermittent torque allowed by the gearhead of the 6-mm Faulhaber motor for should yaw and elbow yaw, as shown in Equation 4-17

and Equation 4-18 respectively. A free body diagram (FBD) of each case is shown in Figure 4.10. Acceleration limits have not been set for this device. These limits will be set during future benchtop testing. Additionally, a dynamic analysis of the system will be completed.

Equation 4-16

$$\tau_{g1} = 35 [g] \left[ \left( 10.7 + \frac{87.5}{2} \right) + \left( 10.7 + 87.5 + \frac{95.3}{2} \right) \right] [mm] \approx 7 \text{ mNm}$$

Equation 4-17

$$\tau_{g2} = 35 [g] \left[ \left( \frac{87.5}{2} \right) + \left( 87.5 + \frac{95.3}{2} \right) \right] [mm] \approx 6.3 \text{ mNm}$$

Equation 4-18

$$\tau_{g3} = 35 [g] \left( \frac{95.3}{2} \right) [mm] \approx 1.7 \text{ mNm}$$

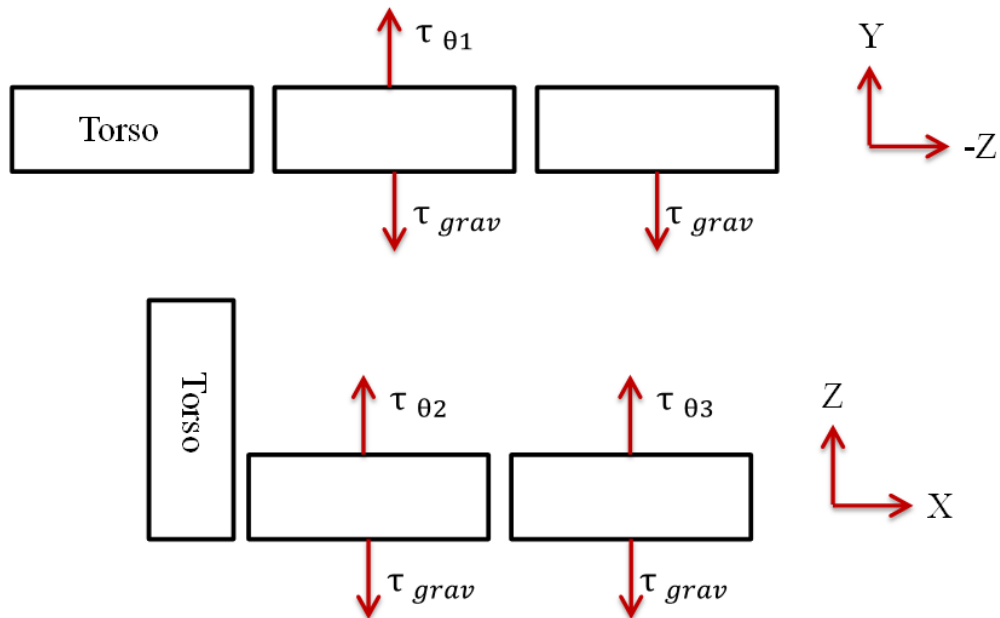


Figure 4.10: Free body diagram (FBD) of EB2.0 when gravity fully acts on each body. Top: FBD for shoulder pitch, Bottom: FBD for shoulder and elbow yaw.

To further understand the capabilities of EB2.0, the calculated static endpoint force in each principal Cartesian axis was compared and the minimum value was plotted across the workspace. The results were plotted using the surface function in MATLAB®, as shown in Figure 4.11. The code that was used to calculate and plot the minimum static endpoint force across the workspace and the original plot can be found in Appendix B.

It should be noted that a large majority of the workspace meets or exceeds the values set forth earlier within Chapter 3, Section 3.2. In addition, all of the endpoint force deficiencies are seen at the boundary of the workspace, where one or more of the DOFs are lost. Force deficiency plots can be found in Appendix B. The deficiency plots show in detail how the force capabilities decrease as the singularity is approached.



**Figure 4.11: EB2.0 minimum static endpoint force, right arm (Forces are in Newtons with a scale from 0.8-3 [N]).**

### ***Section 4.1.4.3: Velocities***

Using Equation 4-13 and known no-load angular velocities from Table 4.2, the endpoint velocity can be found along each of the principal Cartesian axes. The theoretical no-load angular velocity can be calculated using Equation 4-19.

$$\omega_{joint} = \frac{\omega_{nl}}{N_I \cdot N_E} \quad \text{Equation 4-19}$$

Once the individual joint no-load angular velocities were found, the theoretical endpoint velocity in each Cartesian direction was calculated and plotted across the workspace. The results were plotted using the surface function in MATLAB®, as shown in Figure 4.12. The code that was used to calculate and plot the endpoint velocity in each principal Cartesian axis can be found in Appendix B.

This analysis assumes no gravity and massless arms. While not exact, the values found are a reasonable estimation of the prototype's abilities. Based on the worst case scenario, when gravity fully acts on the body of interest as shown in Figure 4.10, the maximum torque required for gravity compensation can be calculated as shown in Equation 4-16, Equation 4-17, and Equation 4-18. The provided speed-to-torque gradient, found in Appendix C, can be used to calculate the revised no-load speed for each joint as shown in Equation 4-20. The recommended speed at  $\tau_g$  and the no-load speed can also be compared using the speed-torque curve for each motor which is provided in Appendix C. There is no significant change in no-load speed for any of the joints. Additionally, the revised no-load speed is greater than the recommended maximum angular velocity for each joint.

## Equation 4-20

$$\omega_{nl, revised} = (\text{speed} - \text{to} - \text{torque gradient}) * (\tau_{stall} - \tau_g)$$

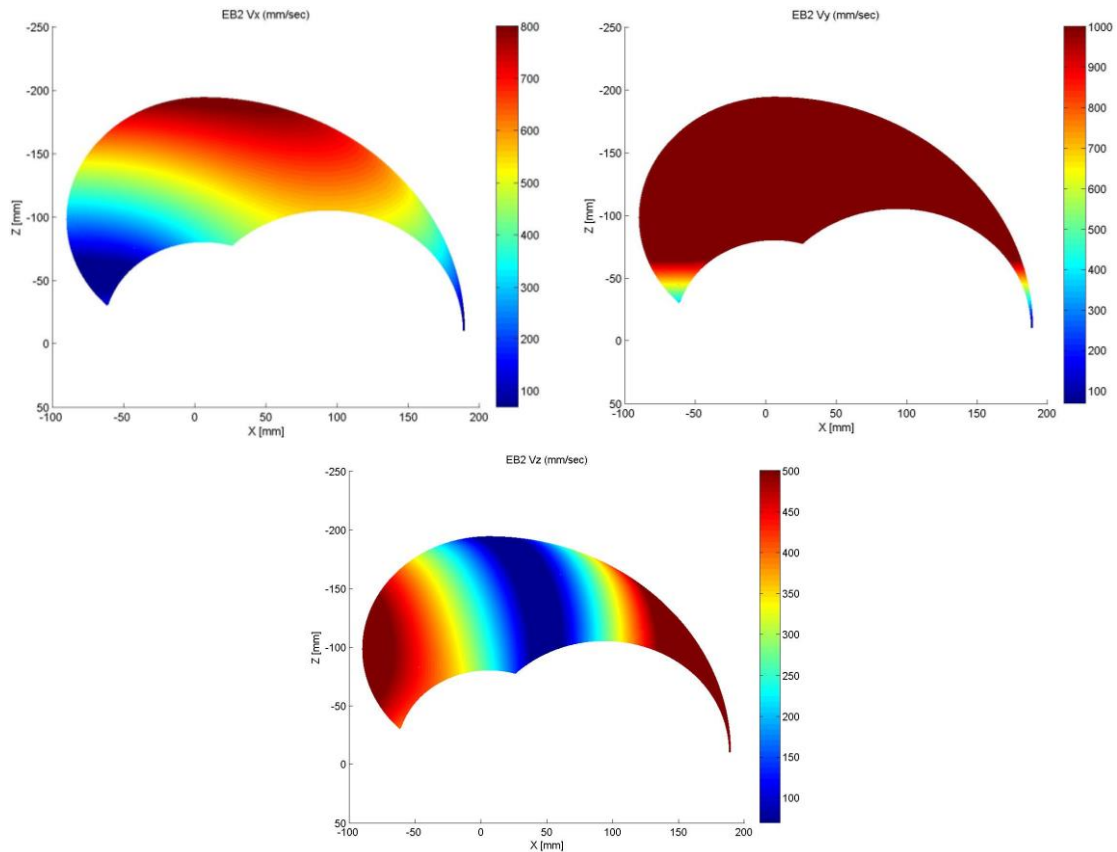


**Figure 4.12: EB2.0 endpoint velocity in each principal Cartesian axis, right arm (Please note that the velocity scale for each individual plot is different: Vx: 70-800 [mm/s], Vy: 70-1000 [mm/s], Vz: 72-500**

To further understand the capabilities of EB2.0, the calculated endpoint velocity in each principal Cartesian axis was compared and the minimum value was plotted across the workspace. The results were plotted using the surface function in MATLAB®, as shown in Figure 4.13. The code that was used to calculate and plot the minimum endpoint velocity across the workspace and the original plot can be found in Appendix B.

It should be noted that a large majority of the workspace meets or exceeds the values set forth earlier within Chapter 3, Section 3.2. The endpoint velocity deficiencies



are seen where one or more of the DOFs are lost and are unable to contribute to the endpoint velocity in one of the principal Cartesian axes. Velocity deficiency plots can be found in Appendix B. The deficiency plots show in detail how the velocity capabilities decrease as the singularity is approached.



**Figure 4.13: EB2.0 minimum endpoint velocity, right arm (Velocity is in mm/sec with a scale from 70-150 [mm/sec]).**

## ***Section 4.2: Physical Design***

As previously stated, EB2.0 is composed of two arms, each with four degrees of freedom. Each arm has three segments/links which are labeled as ‘Torso’, ‘Upper Arm’, and ‘Forearm’. The left and right arms are symmetric about the YZ plane. An isometric view of EB2.0 is shown in Figure 4.14. Each segment/link is labeled and will be discussed in detail in the following sections.

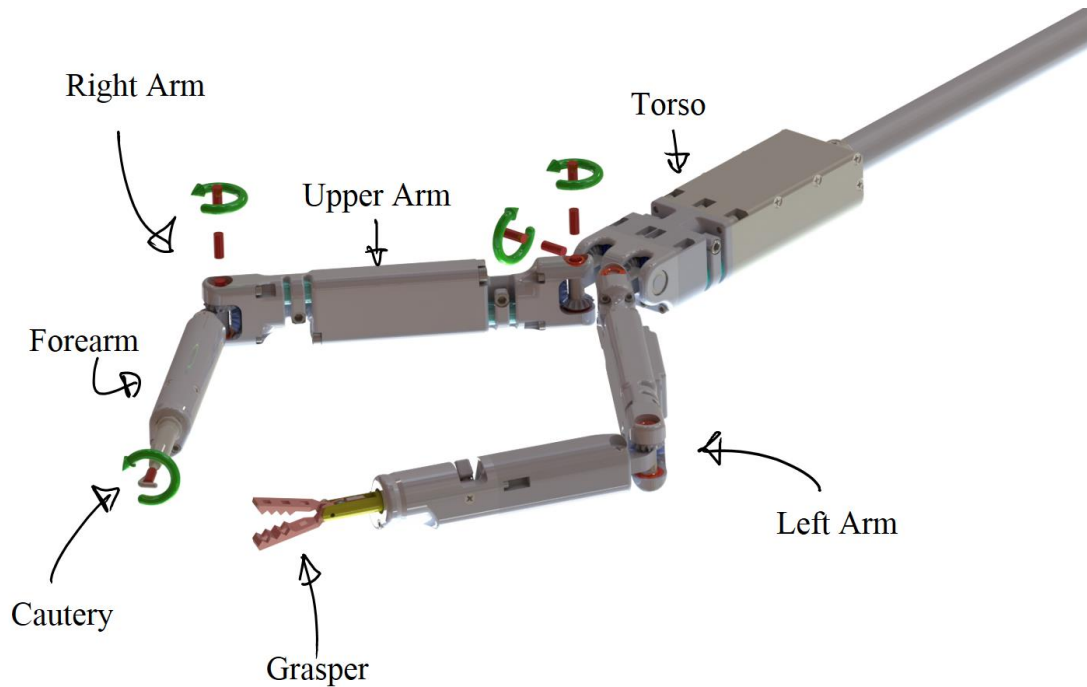
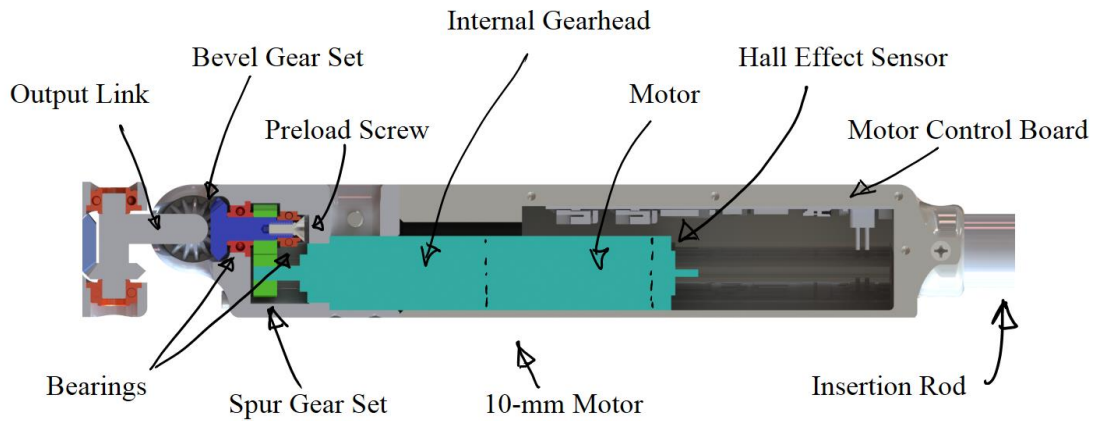


Figure 4.14: Isometric view of EB2.0.

### *Section 4.2.1: Torso*

The torso of the robot is shared between the right and left arm, and houses the first DOF of the 2-DOF shoulder joint for each arm. This DOF provides shoulder pitch. Shoulder pitch is powered by an 8 Watt, 10-mm brushless DC motor with 256:1 integrated gearhead and Hall effect sensor package from Maxon Motor (Sachseln, Switzerland). The data sheet for this motor combination can be found in Appendix C. The internal gearhead is mated to a spur gear set with a 1:1 gear ratio which is assembled to a 90 degree 1:1 bevel gear set to provide rotation perpendicular to the axis of the motor. A cross section of this joint is shown in Figure 4.15.



**Figure 4.15: EB2.0 torso cross section view.**

All shaft to spur gear mates are coupled using a “D-shaped” geometry, as shown in Figure 4.16. This type of mechanical mate rotationally fixes the two parts, while allowing disassembly.

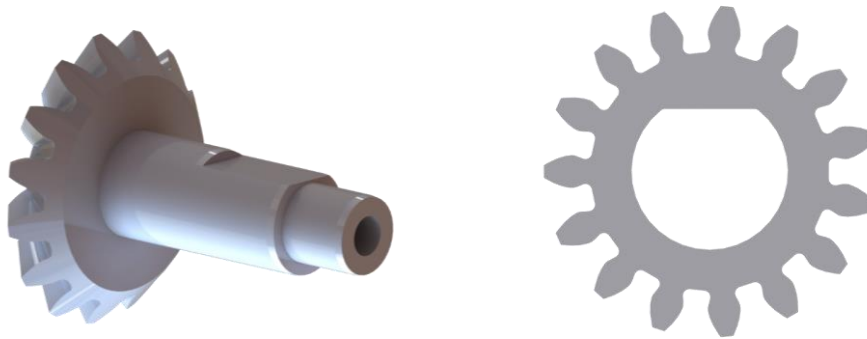


**Figure 4.16: EB2.0 “D-shaped” geometry spur gear to shaft mate.**

All shafts are supported by two deep-groove ball bearings at a spacing greater than 2 times the inner diameter. Bearings are shown in red within Figure 4.15. A motor control board is also shown within the cross-section view. The master control board is responsible for sending and receiving update commands sent from the host computer. It also relays updates from the local control boards. The master board also has a copy of the local control

boards, responsible for controlling shoulder pitch for the right and left arms of the robotic prototype. The control system will be discussed in detail in Chapter 4, Section 4.3. The 10-mm brushless motor is secured in the motor housing by a mechanical friction clamp, shown in Figure 4.17.

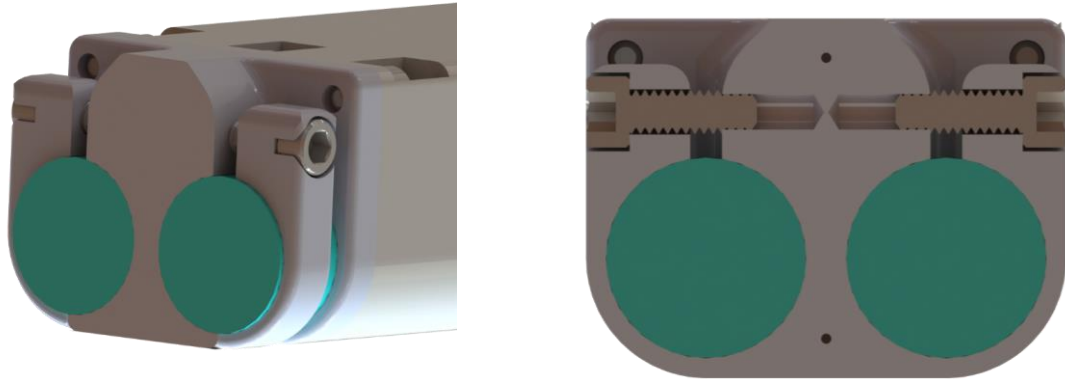
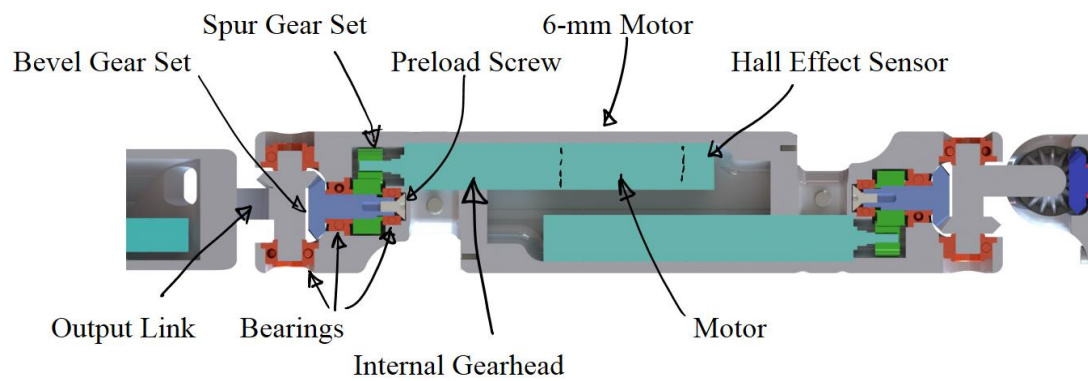


Figure 4.17: EB2.0 10mm motor clamp.

### ***Section 4.2.2: Upper Arm***

The upper arm of the prototype device provides two DOFs, shoulder and elbow yaw. These joints are identical copies. A cross-section view is shown in Figure 4.18. Similar to the torso, both joints consist of a spur and bevel gear set. However, these joints are powered by a smaller 1.5W 6-mm brushless DC motor with 1024:1 integrated gearhead and Hall effect sensor package from Faulhaber (Schönaich, Germany). The data sheet for this motor combination can be found in Appendix C. The internal gearhead is mated to a spur gear set with an 8:5 gear ratio which is assembled to a 90 degree 1:1 bevel gear set to provide rotation perpendicular to the axis of the motor. All shaft to spur gear mates are coupled using a “D-shaped” geometry, like previously shown in Figure 4.16. The 6-mm brushless motor is secured in the motor housing by a mechanical friction clamp, like

previously shown in Figure 4.17. Additionally, all shafts are supported by two deep-groove ball bearings at a spacing greater than 2 times the inner diameter. Bearings are shown in red in Figure 4.18. A local motor control board, not shown, is also housed within the upper arm. The local control board has two motor drivers and is responsible for controlling shoulder and elbow yaw. Additional details about the control system will be discussed in Chapter 4, Section 4.3.



**Figure 4.18:** EB2.0 upper arm cross section view.

### ***Section 4.2.3: Forearms***

Three different forearm designs were developed for EB2.0. Each of the forearm designs could be interchanged with different surgical tools for the specified surgical task. For general surgical procedures such as a colectomy, a grasper and a monopolar electrocautery device are the essential tools. Typically, for a right-handed surgeon the left hand controls the grasper, while the right hand is used to control the cautery, which requires a steady and precise hand. It should be noted that the right and left end-effectors are easily interchangeable. For this prototype only a monopolar hook cautery device, grasper, and

surgical shears were developed. However, with minor alterations many other surgical tools could be retro-fitted for this device.

### ***Section 4.2.3.1: Monopolar Hook Cautery***

A single-DOF forearm was designed specifically for a monopolar hook cautery. This forearm only actuates the end-effector roll DOF and consists of a 6-mm motor, spur gear set, monopolar hook cautery, and slip ring. A cross section view is shown in Figure 4.19. Similar to the upper arm, a 6-mm motor combination with a 256:1 internal gearhead from Faulhaber (Schönaich, Germany) was used. However, due to space constraints the motor is glued within the motor housing. The internal gearhead is mated to a spur gear set with an 8:5 gear ratio. All shaft to spur gear mates are coupled using a “D-shaped” geometry. Additionally, all shafts are supported by two deep-groove ball bearings at a spacing greater than 2 times the inner diameter. Bearings are shown in red in Figure 4.19. A slip ring is used to provide electrical connection between the monopolar hook cautery and the electrosurgical generator, allowing unlimited rotation of the end-effector.

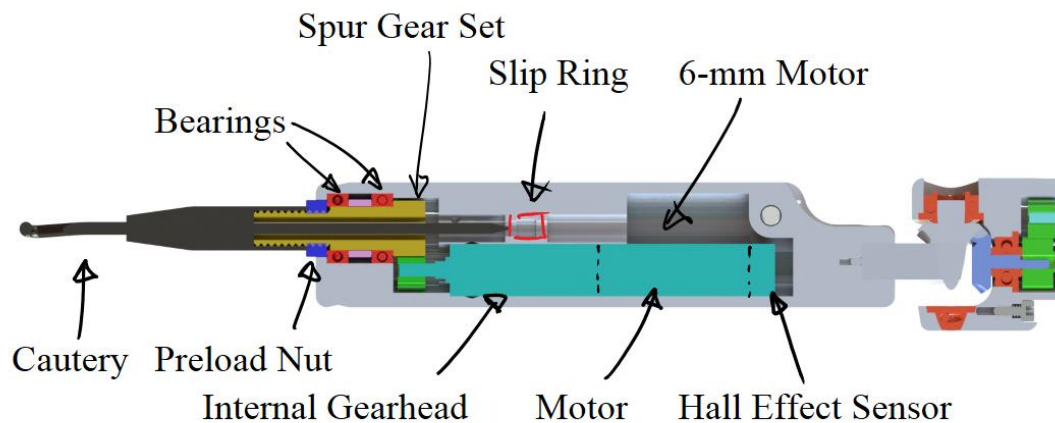


**Figure 4.19:** EB2.0 monopolar hook cautery cross section view.

### ***Section 4.2.3.2: Grasper End-Effector***

A 2-DOF forearm was designed for an open and close type of end-effector such as a grasper, needle driver, or surgical shears. This forearm actuates the open and close action of the end-effector using a custom linear screw drive. End-effector roll is performed at the distal tip of the forearm using a standard spur gear set. This forearm consists of two 6-mm motors with spur gear sets, a linear screw drive, and the selected end-effector, in this case a grasper. A cross-section view is shown in Figure 4.20. The 6-mm motor that actuates the open/close actuation is not shown. Similar to the upper arm, a 6-mm motor combination with a 256:1 internal gearhead from Faulhaber was used for both end-effector actuations. The internal gearhead for the open and close actuation is mated to a spur gear set with an 8:5 gear ratio, while the other gearhead is mated to a spur gear set with a 12:5 gear ratio. All shaft to spur gear mates are coupled using a “D-shaped” geometry. Additionally, all shafts are supported by two deep-groove ball bearings at a spacing greater than 2 times the inner diameter. Bearings are shown in red in Figure 4.20. This forearm is equipped with a local control board, responsible for both end-effector actuations.

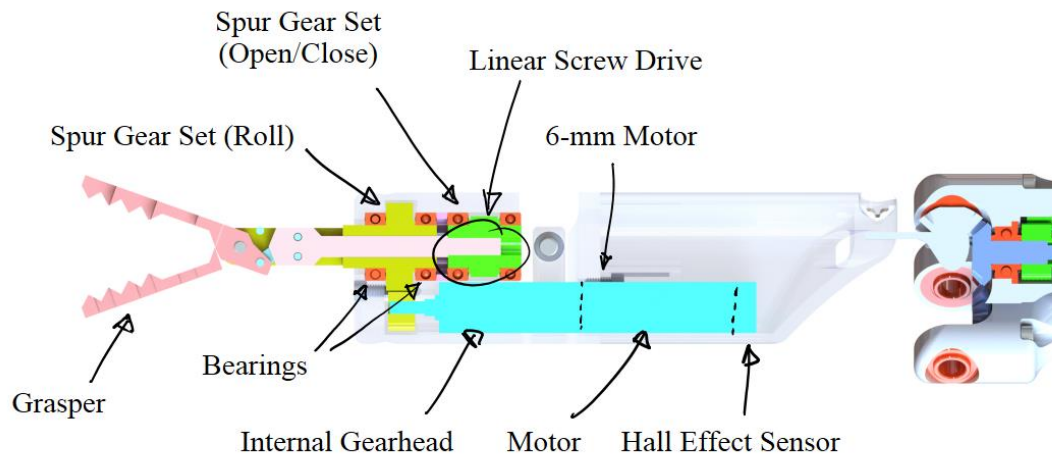


**Figure 4.20: EB2.0 2-DOF forearm cross section view.**

Based on the configuration of this forearm, the linear screw drive is coupled to the end-effector roll actuation. Both DOFs must be actuated at the same rate for the end-effector to roll without the grasper opening or closing.

The jaws of the grasper are part of a 4-bar-linkage that is driven by the linear screw drive. A cross-section view of the linkage is shown in Figure 4.21. One of the 4-bar-linkages is labeled. Over time, this type of linkage has been proven as a more stable mechanism as compared to a pin and slot type of 4-bar-linkage that was used with predicate devices. Deformation was often seen in the slot, causing severe backlash.



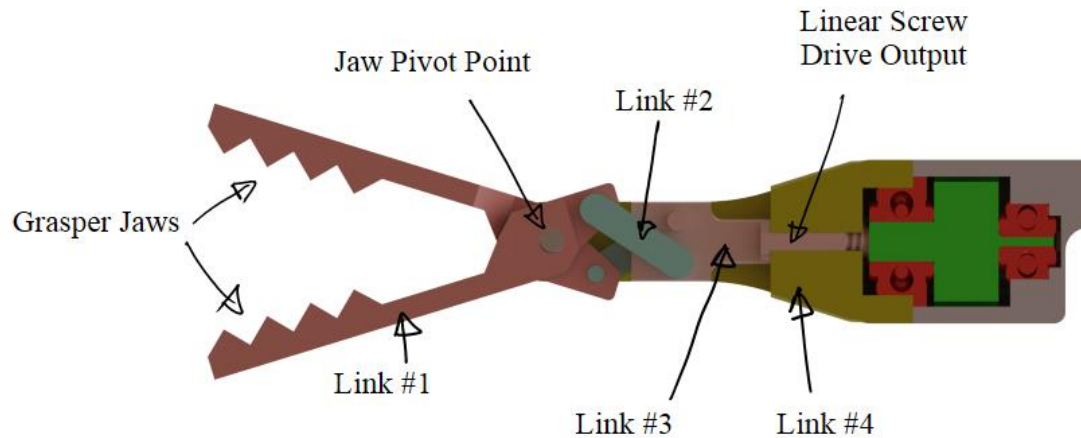


Figure 4.21: EB2.0 grasper cross section view.

### *Section 4.2.3.3: Alternate Grasper End-Effector*

An alternative grasper design has been developed that decouples the two end-effector actuations by moving grasper roll to the proximal end of the forearm. The joint design is otherwise nearly identical to the previously discussed forearm. A cross-section view is shown in Figure 4.22. This alternative configuration allows the prototype device to have two grasper-type end-effectors for surgical tasks such as suturing. Previously, only one grasper type forearm was allowed due to space constraints. The alternative forearm is equipped with a local control board, responsible for both end-effector actuations. However, this forearm design does not allow unlimited rotation of the end-effector because of the cabling between the upper arm and forearm.

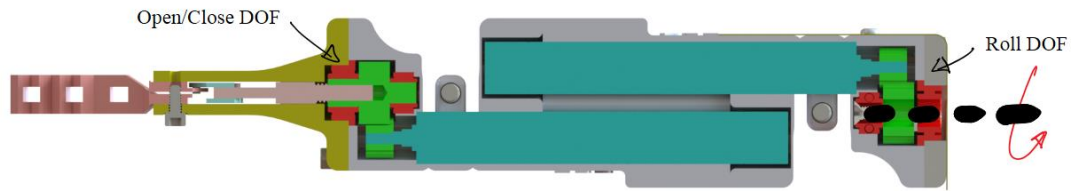
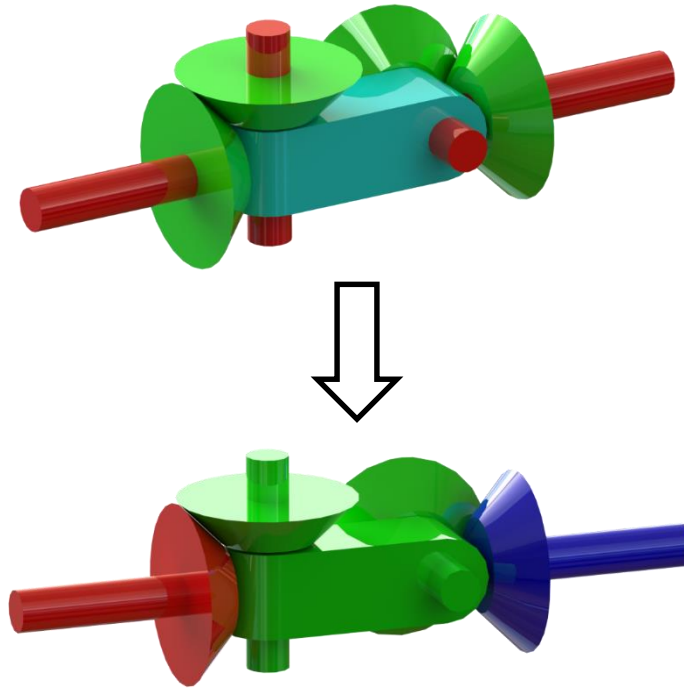


Figure 4.22: EB2.0 alternative grasper forearm design cross section view.

### ***Section 4.2.4: Bevel Gear Manufacturing***

A non-standard manufacturing technique, lost wax investment casting, was used to manufacture all of the bevel gears for EB2.0. Wood et al. developed NB1.0 using modified commercial-off-the-shelf (COTS) bevel gears. The shoulder yaw joint consisted of a link and mating bevel gear. Looking at specifically the joint between frame {1} and {2} of EB2.0, five individual parts would be required if traditional manufacturing techniques were used: 2 modified COTS bevel gears, 2 bearing shafts, and 1 link. This comparison is shown in Figure 4.23. In addition to the part count difference, there is almost a 35% cost savings between the two manufacturing methods. The cost break-down between traditional and non-traditional manufacturing techniques for EB2.0 is shown in Table 4.3. This price comparison is for 6 units. A greater cost savings will be seen as the number of units are increased.



**Figure 4.23: Joint design comparison using traditional (top) versus non-traditional (bottom) manufacturing techniques.**

The investment-cast bevel gears were manufactured out of 316 stainless steel (SS). A major difference in the surface finish of the bevel gears based on manufacturing techniques can be seen. The final parts required some surface finishing and minor touchups where the bearings were seated. As a precaution the bevel gears were buffed using a scouring pad to remove any excess material. Some of the original parts and one touched-up part are shown in Figure 4.24.

Table 4.3: EB2.0 joint cost using traditional versus non-traditional manufacturing techniques.

Joint	Traditional		Non-Traditional	
	Parts	Cost	Parts	Cost
1	Bevel Gear	\$105	Bevel Gear Input	Lot Cost
	Shaft	\$135		
1-2	2x Bevel Gear	\$210	Link 1-2	Lot Cost
	2x Shaft	\$270		
	Link	\$365		
2	Bevel Gear	\$105	Bevel Gear Input	Lot Cost
	Shaft	\$135		
3	Bevel Gear	\$105	Bevel Gear Input	Lot Cost
	Shaft	\$135		
3-4	Bevel Gear	\$105	Link 3-4	Lot Cost
	Shaft	\$135		
	Link	\$365		
Total:		\$2170		\$1420



**Figure 4.24:** Lost wax investment cast bevel gears. The bearing seats on the far right part have been touched up. The other two parts are as cast.

### ***Section 4.2.5: Flexibility Methods***

The automation of the task of making this type of robotic device flexible for insertion through a natural orifice will be one of the most important topics in the coming years. Novel flexibility mechanisms will be required to allow a smoother transition to NOTES. One of the most promising devices provides an additional benefit that would help to make the device more human friendly.

An electropermanent magnetic clutch has been developed that would allow the clutch to become “programmable.” This type of magnetic technology has been used in other types of robotic devices such as modular robotics [54]. Such a clutch can become completely flexible for insertion through a natural orifice, become rigid once inside the

abdominal cavity, and can be tuned to a torsional stiffness between the two extremes, while consuming a minimal amount of power. This type of magnetic technology is similar to an electromagnet; however, it only consumes power when changing the magnetic field strength. Gilpin et al. proposed a method for assembling such devices by using two different types of permanent magnet materials wrapped in copper coil and capped with soft-iron poles, as shown in Figure 4.25. One of the permanent magnets is Neodymium-Iron-Boron (NdFeB), and the other is Alnico V. Both of the materials have essentially the same magnetization; however, the magnetic field of Alnico V can be switched about 100 times easier than the neodymium magnet. Thus, Alnico V can be easily coerced, changing the overall magnetization of the electropermanent magnet from approximately zero to twice the strength of a single magnetic core. The opposing side of the clutch would be equipped with a standard diametrically magnetized rare earth magnet or some type of multi-pole magnet. The original concept drawing of the electropermanent magnetic clutch design is shown in Figure 4.26. Inadvertently, this type of transmission system provides a compliant mate between the input and output of the joint, while adding an elasticity constant to the joint dependent on the magnetization of the electropermanent magnet. In theory, this type of transmission system could be directly mounted to the motor shaft, due to the separation forces from the bevel gear set being decoupled from the input. Many advantages can be envisioned with this type of transmission such as reduced rate of joint failure, reduced unforeseen patient trauma, and ability to become flexible for insertion through a natural orifice.

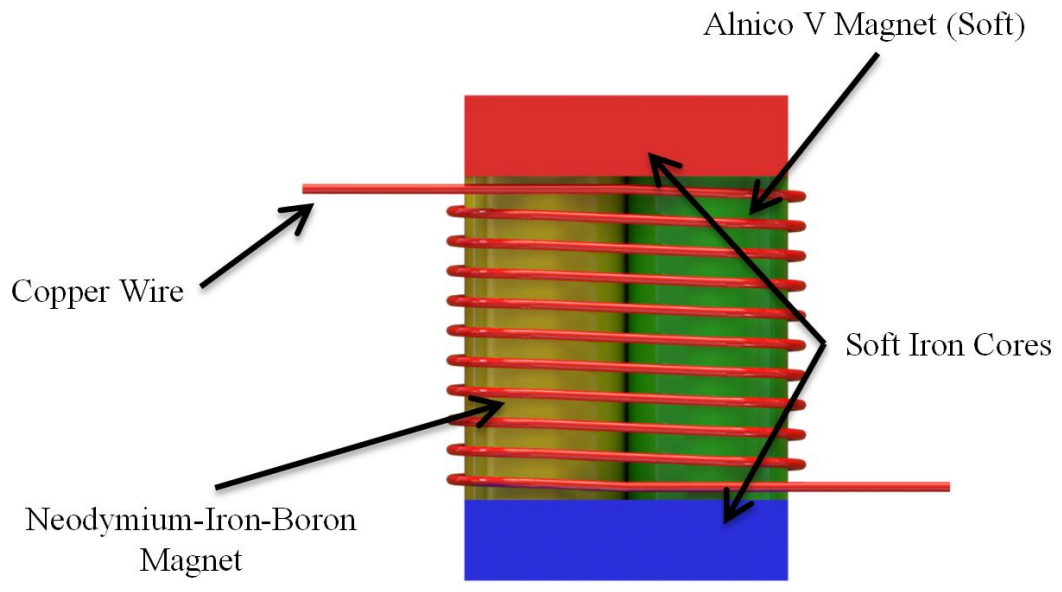


Figure 4.25: Electropermanent magnet assembly.

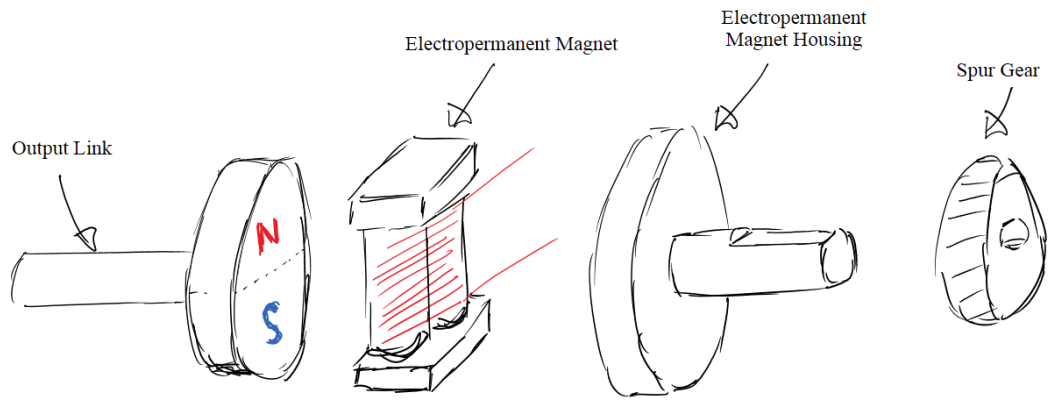
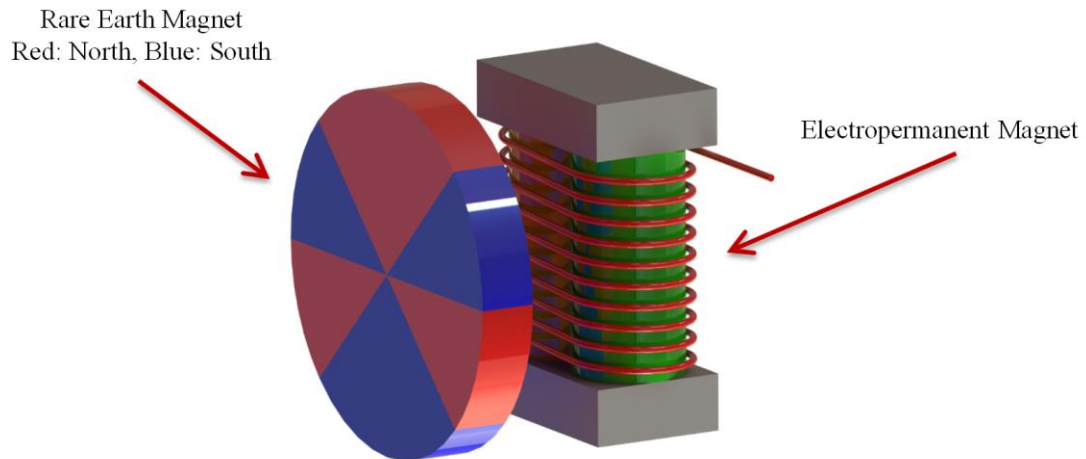


Figure 4.26: Original concept drawing for an electropermanent magnetic clutch.

A preliminary design of the electropermanent magnetic clutch (EPMC) with an opposing multi-pole magnet is shown in Figure 4.27. The control strategy of this joint designed is based on the theory of a series-elastic actuator, where the angular deflection between the electropermanent magnet and the multi-pole magnet can be measured and a joint torque could be derived. As described in Chapter 4, Section 4.1.4, the end point force

can then be found from the known joint torques, eliminating the need for an additional sensor to measure the interaction forces.



**Figure 4.27: Preliminary design for an electropermanent magnetic clutch (EPMC).**

Relative motion between the electropermanent magnet and the rare earth magnet generates both attractive and repelling forces. Analyzing the top half of the EPMC, an attractive force is generated by the red sector, while a repelling force is generated by one of the blue sectors depending on the direction of relative motion. Hence,  $\frac{3}{4}$  of the magnet is generating a resistive force. If the resistive force is applied at the center of mass of each sector, the minimum radius from the center of the rare earth magnet is based on the largest sector. The minimum radius is 0.0707 inches. The attractive and repelling force was based on a  $\frac{1}{4}$ " diameter by 0.125" thick NdFeB, Grade N52 magnet from K&J Magnetics, Inc. that was capable of generating a maximum pull force of 4.59 lbs. The maximum torque that could be transmitted by the EPMC is shown in Equation 4-21. The estimated allowable torque of the EPMC is capable of transmitting the maximum continuous torque of the 6-mm Faulhaber motor, while only 78.6% of the maximum intermittent torque.



Equation 4-21

$$\tau = 0.0707 [in] * 4.59 [lbf] * \left(\frac{3}{4}\right) = 0.243 lbf \cdot in \rightarrow 27.5 mNm$$

The presented flexibility method is a novel concept would allow the device to achieve an infinite number of joint states from flexible to rigid and anywhere between. The current transmission capabilities of the preliminary design are not applicable to the current device. Future benchtop testing will reveal the actual torque capabilities.

### ***Section 4.2.6: Vision System***

Carlson et al. developed a high-definition stereoscopic vision system for medical applications as shown in Figure 4.28, [55]. This system provides two 720p HD video streams at 30 frames per second (fps). A set of low profile, variable focus liquid lenses from Varioptic (Lyon, France) have been combined with the camera system. The integration of the HD stereoscopic vision system with EB2.0 is shown in Figure 4.29.

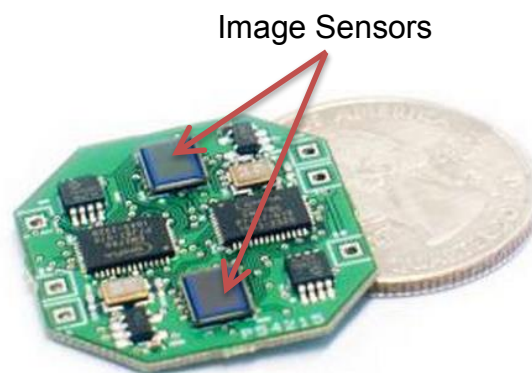


**Figure 4.28: High-definition stereoscopic vision system (Carlson et al.).**

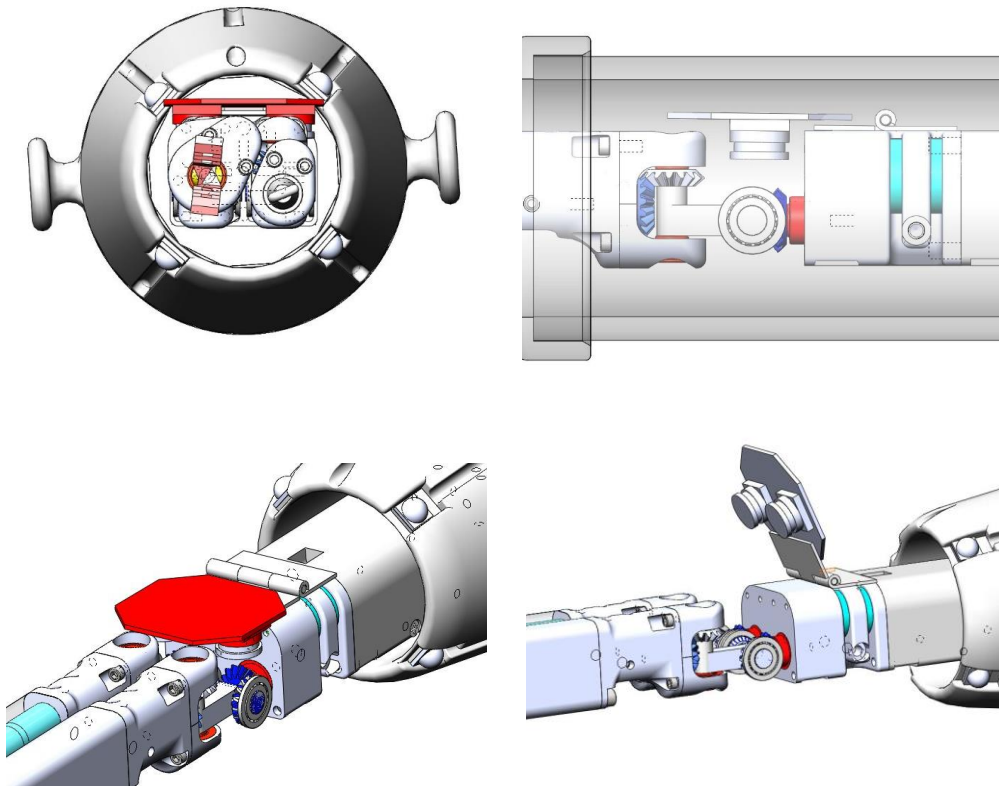


**Figure 4.29: Integration of EB2.0 with the high-definition stereoscopic vision system (Carlson et al.).**

The current vision system is too large for the current insertion cannula, however the system provides a very stable viewing platform. The liquid lenses have no moving parts and allow the surgeon to quickly and accurately focus on different items of interest throughout the surgical procedure.

The camera feedback could then be viewed on a 3-dimensional (3D) viewing system that uses mirrors to redirect the viewer's eyes to 2 independent monitors referred to as a mirror stereoscope, as shown in Figure 4.30. Commercial-off-the-shelf (COTS) 3D viewing systems could also be used such as the Oculus Rift (Oculus VR®) or a 3D television with polarized glasses.

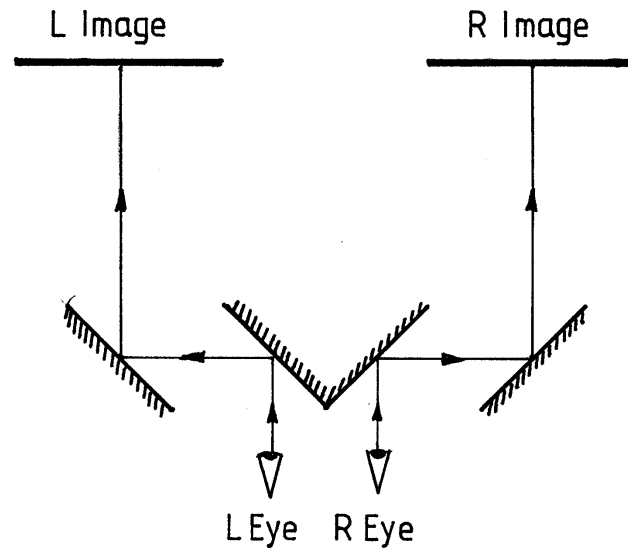
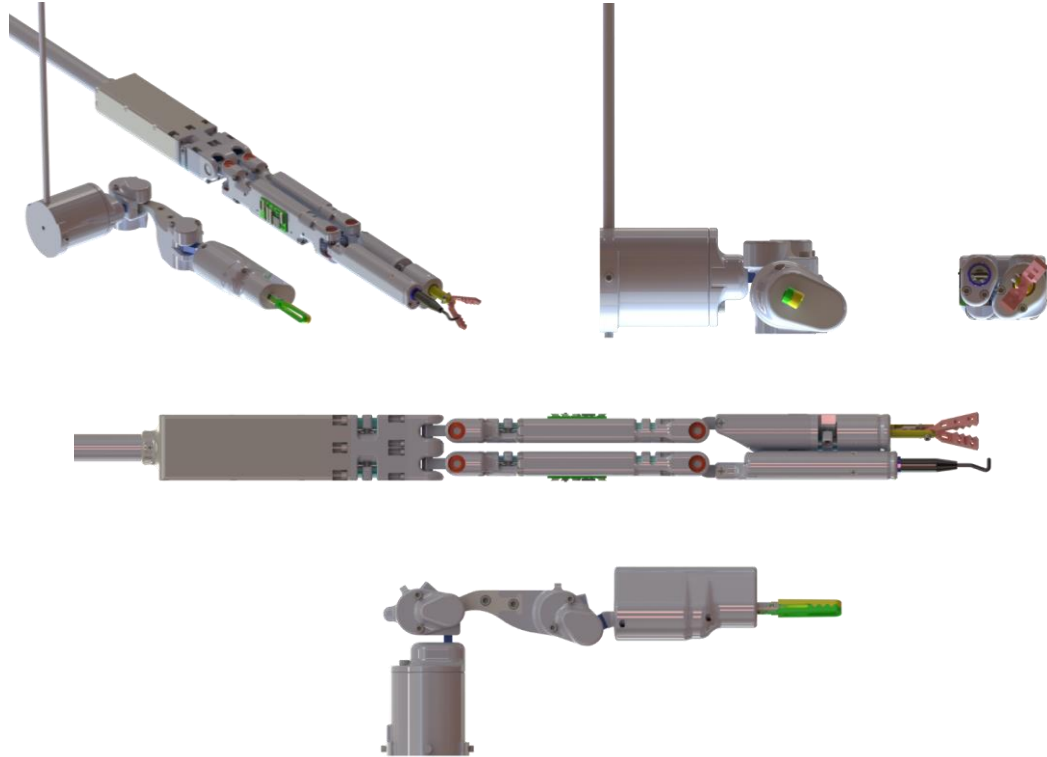


Figure 4.30: 3-dimensional viewing system, mirror stereoscope (<http://www.3dfocus.co.uk/>).

### *Section 4.2.7: Size Comparisons*

The prototype device, EB2.0, has been designed to be approximately the size of a single arm of the predicate device, TB2.0. A single arm of the predicate device has been successfully inserted into the abdominal cavity through a single incision. The size comparison of EB2.0 and a single arm of TB2.0 is shown in Figure 4.31.



**Figure 4.31: Size comparison of EB2.0 and a single arm of TB2.0. Top left: isometric view of size comparison. Top Right: front view of size comparison. Bottom: top view of size comparison.**

## ***Section 4.3: Control System***

### ***Section 4.3.1: Hardware and Communication***

All previously developed miniature in vivo surgical robotic prototypes from the Advanced Surgical Technologies Lab were controlled using via external motor controllers. This architecture required all of the motor leads to pass through the access site. For example, TB2.0 presented by Wortman [38] had 54 conductors passing through the incision site. The bundle of 54 wires is approximately 11 mm in diameter, accounting for over 30% of the access site for a standard LESS surgical procedure. To eliminate this large bundle of wires and associated external control hardware, Bartels [56] has developed a

distributed motor control system for miniature *in vivo* surgical robots. The conceptual diagram of the distributed motor control system is shown in Figure 4.32. Bartels et al. provided the basis for the software and hardware architecture for an *in vivo* robot with brushed DC motors. The third version of this distributed control system for brushless DC motors will be described herein.

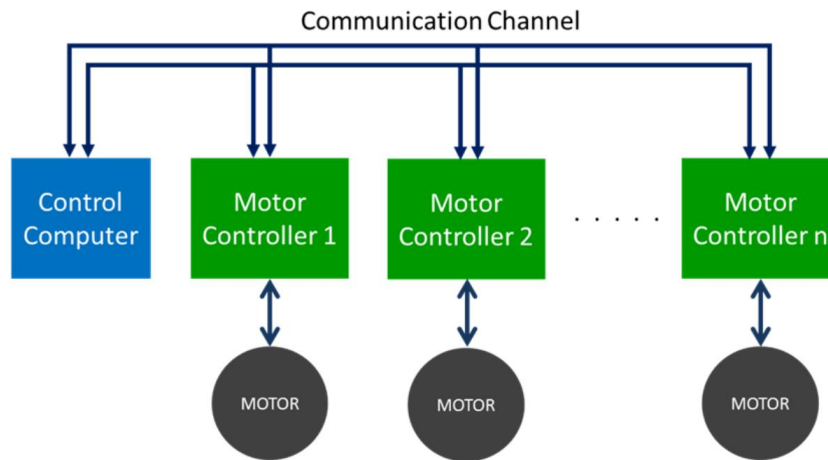
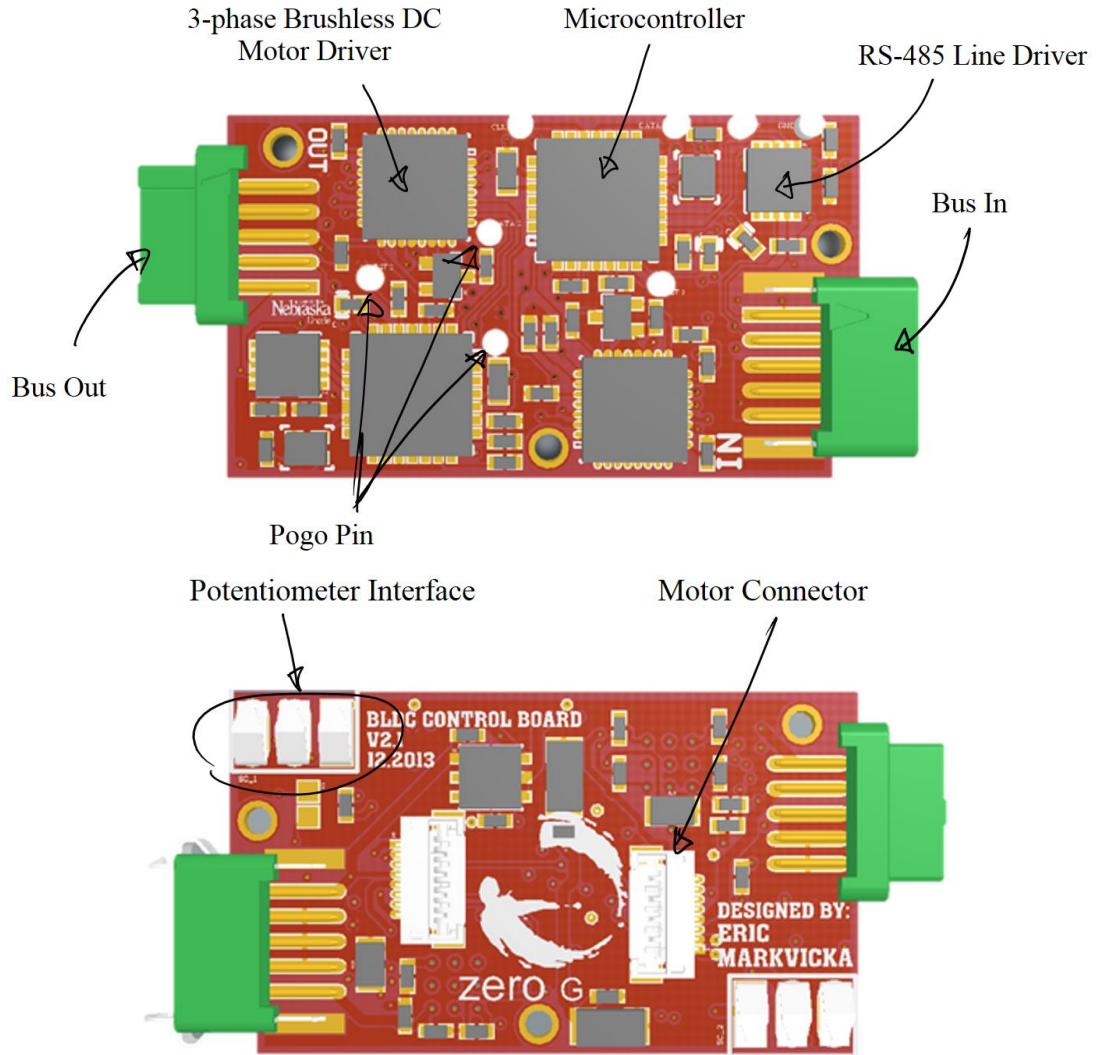


Figure 4.32: Conceptual diagram of the distributed motor control system (Bartels et al.).

### ***Section 4.3.1.1: Brushless DC Distributed Motor Control***

The brushless DC motor control board was based on the second version of the hardware that was developed by Bartels [56]. The current prototype, version 3 (V3), of the distributed motor control system (DMCS) is shown in Figure 4.33. Only one of the two identical motor control circuits is labeled. The schematic documents can be found in Appendix D.



**Figure 4.33:** Board layout for distributed motor control system V3, Top: front side of PCB, Bottom: back side of PCB.

The major changes to the electrical hardware between V2 and V3 of the DMCS is the replacement of the brushed DC H-Bridge with a three-phase motor controller, addition of Gecko (Harwin, Portsmouth, England) connectors for the differential serial bus, pogo pin programming header, and spring contact potentiometer interface. All other electrical items such as the microcontroller, RS-485 line driver, and voltage regulator remained the same between V2 and V3. The replacement of the brushed DC H-Bridge was an obvious

change between versions. The L6229Q (STMicroelectronics, Geneva, Switzerland) was selected based on its small footprint and ability to provide a peak current of 2.8 Amps. A large amount of time was often devoted to soldering the serial communication bus for both previous versions of the DMCS. Failures also occurred due to poor strain relief of this delicate connection. A miniaturized, high reliability connector from Harwin (Portsmouth, England) was added to V3 of the DMCS. The Gecko connector features 2A conductors, keyway polarization, and retention latches to ensure a secure connection. Each wired assembly also features a snap-in housing and back epoxy potting well for additional strain relief.

A pogo pin programming header interface was also added to minimize the footprint of the board. A pogo pin is a temporary electrical connection that is often used for in-circuit programming or with automatic test equipment [57]. A cross section view of a pogo pin is shown in Figure 4.34. This type of programming header allows the programming pins to be placed in a previously unusable place on the board. V3 of the DMCS with the pogo pin programming header jig is shown in Figure 4.35. The last major change was the addition of a spring contact interface of the potentiometer. This change allowed the board to be completely removed from the robotic prototype for possible debugging. Previous versions provided solder tabs for the potentiometer; while sufficient, the spring contacts did not necessarily provide an additional failure point but added convenience when problems arose.



Figure 4.34: Cross section view of a pogo pin.

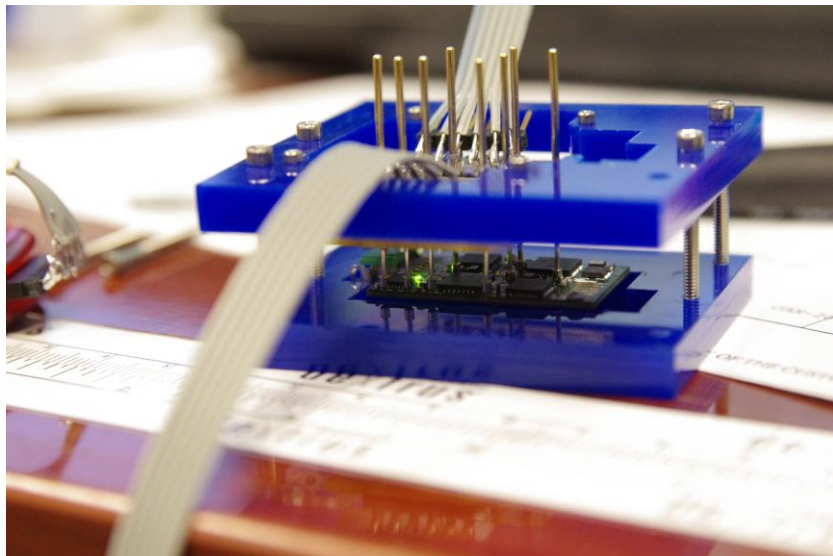


Figure 4.35: DMCS V3 with the pogo pin programming header jig.

### ***Section 4.3.2: Inverse Kinematics***

The inverse kinematics of the prototype can be solved using a geometric approach. A geometric approach is used based on the assumption that frames {1} and {2} intersect. This assumption greatly simplifies the inverse kinematics solution; which can be broken up into two parts,  $\theta_1$  and a planar device. The surgeon uses visual feedback to ensure the device is tracking his/her exact movements. Based on this theory, the assumption that frames {1} and {2} intersect is valid. A solution will be proposed for the right arm of the device as follows. A projection of the robot arm,  $R$ , onto the  $YZ$  plane at a positive pitch



angle of  $\theta_1$  is shown in Figure 4.36. Using the inverse trigonometric function, arctangent with two arguments,  $\theta_1$  can be found, shown in Equation 4-22. Using the Pythagorean theorem, the length of R can be found, shown in Equation 4-23.

**Equation 4-22**

$$\theta_1 = \text{atan2}(Y, \text{abs}(Z))$$

**Equation 4-23**

$$R = \sqrt{Y^2 + Z^2}$$

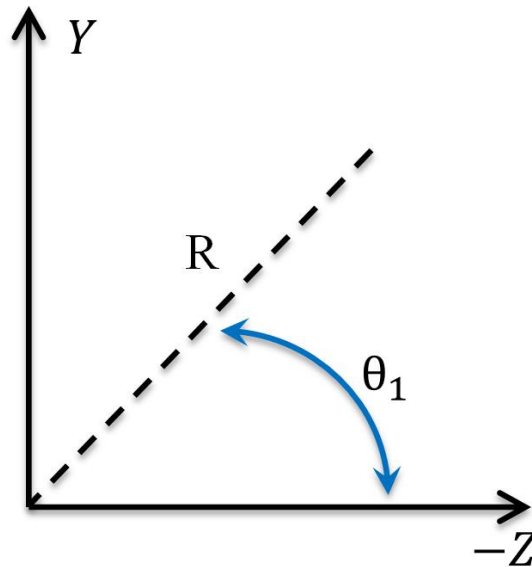


**Figure 4.36: Projection of the robot arm, R, on to the YZ plane.**

The planar orientation of the robotic arm can be used to find  $\theta_2$  and  $\theta_3$ . A projection of the planar arm onto the XR plane is shown in Figure 4.37, where plane R is defined as the plane that contains the robotic arm and is perpendicular to the YZ plane with an angular offset of  $\theta_1$  from the XZ plane.

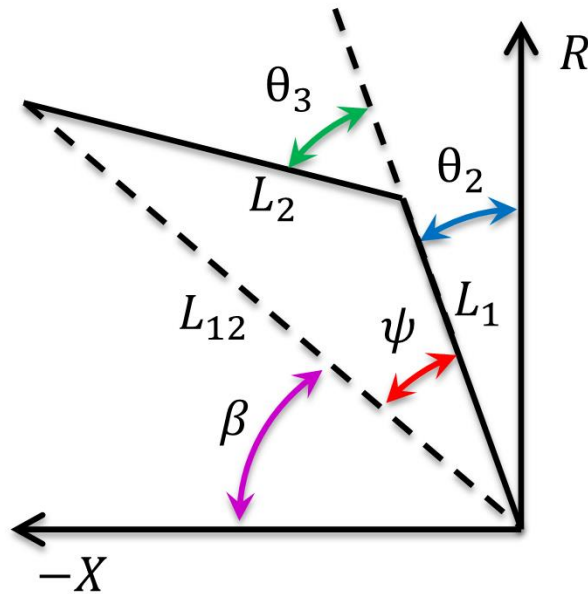


**Figure 4.37:** Planar orientation of the robotic arm projected on to the XR plane, where plane R is defined as the plane that contains the robotic arm and is perpendicular to the YZ plane with an angular offset of  $\theta_1$  from the XZ plane.

The shoulder yaw angle,  $\theta_2$ , is the complimentary angle of the sum of angles  $\beta$  and  $\psi$  as shown in Equation 4-24.

**Equation 4-24**

$$\theta_2 = \frac{\pi}{2} - \beta - \psi$$

Similar to  $\theta_1$ , angle  $\beta$  can be found, shown in Equation 4-25.

**Equation 4-25**

$$\beta = \text{atan2}(R, -X)$$

Angle  $\psi$  can be found using the law of cosines with the known link lengths of  $L_1$  and  $L_2$ , shown in Equation 4-26. This angle can be both  $+\psi$  or  $-\psi$  depending on if the desired X-coordinate is positive or negative.

Equation 4-26

$$\psi = \pm \cos^{-1} \left( \frac{L_{12}^2 + L_1^2 - L_2^2}{2L_{12}L_1} \right) \Rightarrow \begin{cases} +\psi, & \text{if } x < 0 \\ -\psi, & \text{if } x > 0 \end{cases}$$

The length  $L_{12}$  is calculated using the Pythagorean theorem, shown in Equation 4-27.

Equation 4-27

$$L_{12} = \sqrt{x^2 + r^2} = \sqrt{x^2 + y^2 + z^2}$$

Finally, the supplementary angle of  $\theta_3$  can be found using the law of cosines and the known lengths of  $L_1$  and  $L_2$ , shown in Equation 4-28.

Equation 4-28

$$\theta_3 = \pi - \cos^{-1} \left( \frac{L_1^2 + L_2^2 - L_{12}^2}{2L_1L_2} \right)$$

### ***Section 4.3.3: Surgical User Interface***

All of the recent robotic platforms developed by the Advanced Surgical Technologies Lab at UNL have been designed for teleoperation. This ability allows the device to be deployed in extreme environments with applications such as long-duration space flight, battlefields, and remote and rural areas such as the South Pole. The remote surgical user interface is shown in Figure 4.38.

Geomagic® Touch™ Haptic Devices (formerly Sensable Phantom Omni) are used to provide haptic feedback to the user. Currently, the only haptic feedback that is available to the user is the virtual workspace boundary of the device. This information is provided to ensure the operator remains within the usable workspace. Additionally, motion scaling and tremor reduction are provided by these devices to ensure smooth and actuate motion

of the device's end-effectors. Tremor reduction is implemented by applying a virtual “viscosity” to the controller's workspace, which effectively removes small muscle twitches. The controllers also have a two-button interface which is used to control the open and close actuation of the grasper. A set of foot pedals is provided to allow the surgeon to lock/unlock each arm individually or to clutch into a more ergonomic position. The

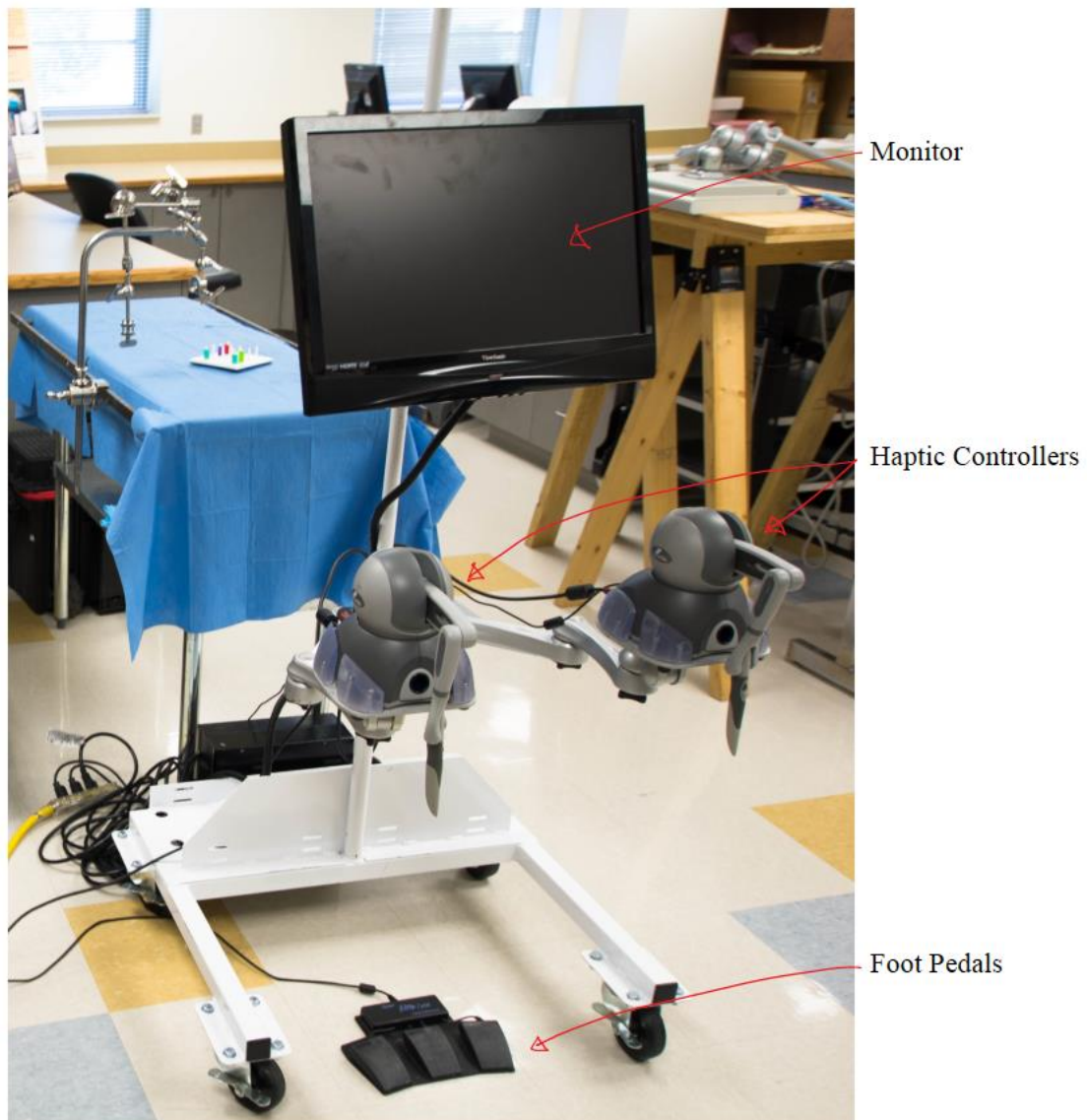


**Figure 4.38: Remote surgeon user interface for EB2.0.**

standard foot pedal setup for operating the electrocautery generator, used to activate the monopolar electrocautery device, is also provided, not shown in Figure 4.38.

### ***Section 4.4: Insufflated Insertion***

The most recent previously developed prototypes required a time consuming and difficult insertion process. The typical insertion of these devices requires brute force to lift the abdominal wall, while each arm is individually twisted and contorted into the cavity under no visualization. The arms are then blindly assembled together using a central insertion rod. A gel port is then placed over the incision and the device to create a seal for insufflation; during this time the device typically sits on the organ floor. Severe ingress is often seen, causing electrical shorts and damage to the external electronics.

Frederick et al. have developed various methods for introducing such devices into the abdominal cavity under insufflation [58]. Some of the devices are shown in Figure 4.39. The most complex of these devices, such as Figure 4.39 A, was heavy, extremely complex, and crowded the surgical site but nevertheless was able to sustain insufflation throughout the insertion process; while simpler, non-intrusive devices, Figure 4.39 B, C, D, failed to maintain insufflation. A simplified insertion method would be required for wide spread adoption.

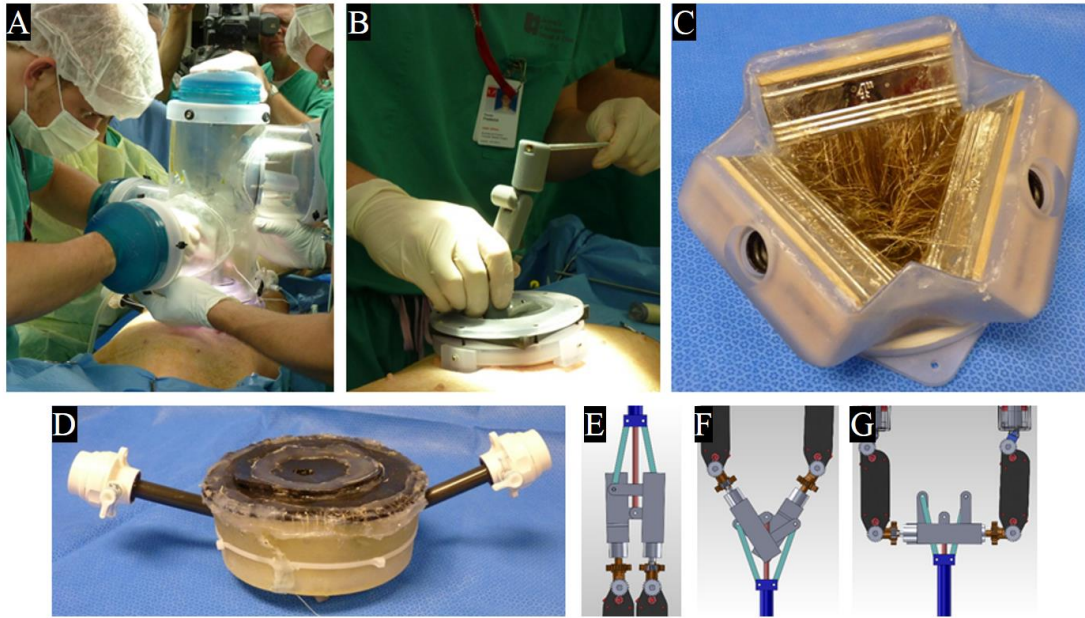


**Figure 4.39:** Subset of insertion devices that were developed to allow non-uniform shaped devices to be insertion into the abdominal cavity under insufflation. A: Canister type device that extends the pressurized environment into the canister, allowing the surgeon to insert and/or remove his/her hands into the pressurized environment and insert the device under insufflation; B, C, D: Standalone, custom insertion port that seals against non-uniform objects; E, F, G: Deployment of a 4-bar-linkage that allows the overall diameter of the arms to be minimized for insertion, E, and expand once fully inserted; F, G (Frederick et al.).

A simpler insertion method was developed for EB2.0 that would allow a single motion to insert the device into the abdominal cavity under insufflation. A large majority of the devices proposed by Frederick et al. required more than one step, [58]. The insertion protocol developed for EB2.0 is similar to a piston-cylinder, where the insertion rod of the device is linearly advanced and the robot is introduced into the abdominal cavity under full visualization. The insertion system has a conical port that is wedged into the single incision. A conical structure was used to all the device to account for variability in the incision size. Sutures are then used to secure the system to the incision. A cross section view of the insertion device is shown in Figure 4.40 and the insertion protocol is shown in Figure 4.41. A linear bushing is used to provide a smooth and accurate insertion into the abdominal cavity, while a radial wiper seal is used to sustain insufflation.



Figure 4.40: Cross section view of the insertion device for EB2.0.

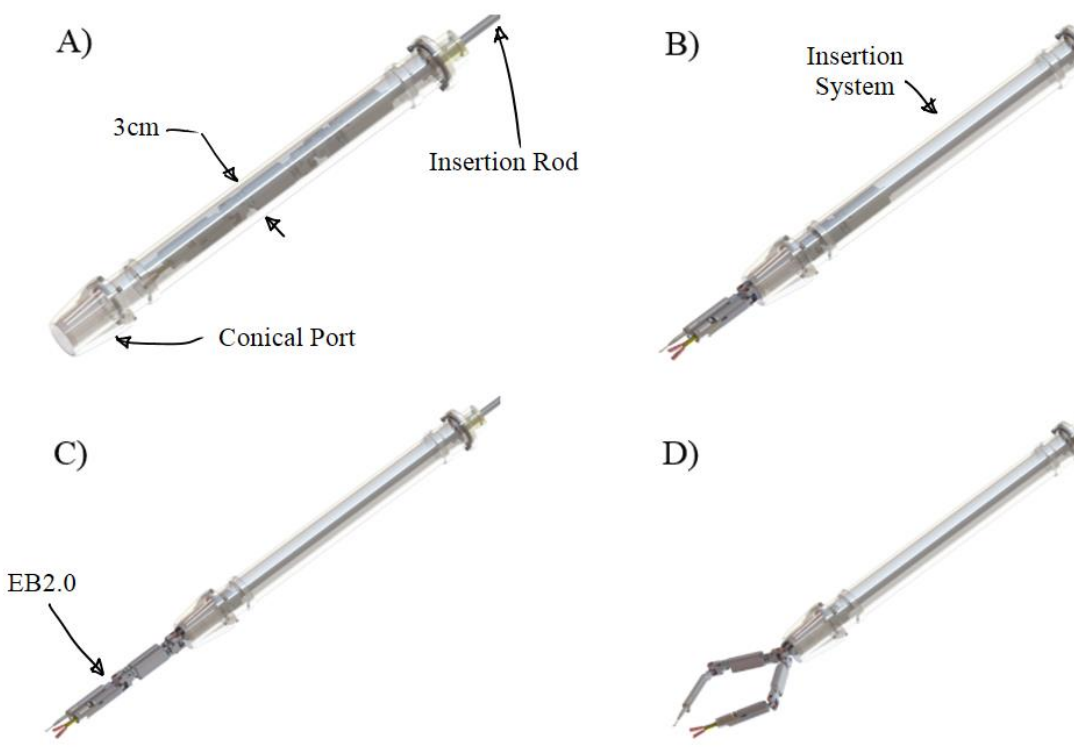
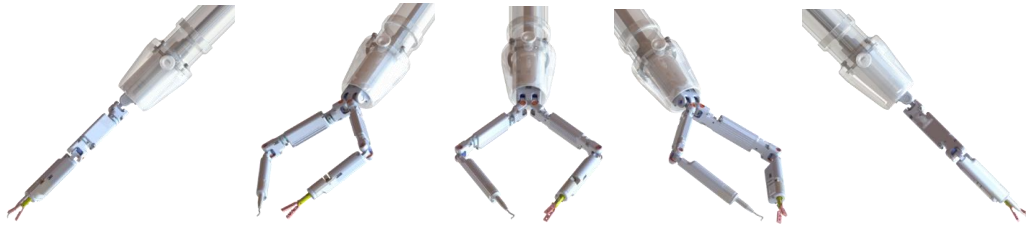


Figure 4.41: Introduction of EB2.0 into the abdominal cavity through a 3 cm diameter access port. A) Robotic platform stored within access port, B) & C) Insertion of the robotic platform into the abdominal cavity, D) Robotic platform secured to the abdominal wall by magnet, ready for surgical procedure to begin. The robotic vision system and communication and power tether is not shown.

The main advantage of this system is its ability to reach all four quadrants of the abdominal cavity. The robotic prototype, EB2.0, has two DOFs relative to the insertion device. EB2.0 can independently rotate and translate about the axis of the insertion rod.

The insertion device has two DOFs relative to the patient. The insertion device can pitch and yaw due to elastic deformation of the abdominal wall, resulting in a conical workspace. After insertion, EB2.0 can be rotated about a fulcrum at the incision site to access multiple quadrants of the abdominal cavity. The articulation of EB2.0 from the upper abdominal quadrant to the lower abdominal quadrant at an angle of 45 degrees relative to vertical is shown in Figure 4.42. Throughout this articulation, the insertion device remains fixed to the incision site. A video of the articulation has been created to help eliminate confusion, [59].



**Figure 4.42: Articulation of EB2.0 from the upper abdominal quadrant to the lower quadrant about a fulcrum located at the access point. Top: top view, Bottom: side view. A video of the articulation can be found at [59].**



## Chapter 5: Conclusions and Future Work

This thesis presents several advancements in the field of single-incision robotic surgery. A miniature *in vivo* surgical robot has been developed with an insufflated insertion protocol and distributed motor control. A high-definition stereoscopic camera system has also been integrated. The theoretical analysis of the devices capabilities were presented and are in line with the proposed requirements and the capabilities of predicate devices. An increase of 79.9% in workspace and 170.8% in intersecting workspace was seen compared to TB2.0, while the diameter a single arm of TB2.0 is larger than the entire diameter of the prototype EB2.0. The entire workspace was increased by increasing the link length of EB2.0. The intersecting workspace was increased by decreasing the distance between the right and left arm of EB2.0. A preliminary design of an electropermanent magnetic clutch has been developed that would allow the device to become flexible for insertion through a natural orifice but then become rigid to perform the surgical procedure.

Several benchtop tests will be performed to verify the efficacy of the device. These results will be compared to the theoretical capabilities and the results from predicate devices. Based on the results, *in vivo* animal experiments will shortly follow. Additional work will include reliability tests in an effort to obtain FDA clearance as a multi-functional surgical robot for LESS procedures. In addition, sterilization will also have to be addressed.

## References

- [1] G. Stiff, M. Rhodes, A. Kelly, K. Telford, C. P. Armstrong, and B. I. Rees, "Long-term pain: less common after laparoscopic than open cholecystectomy.," *Br. J. Surg.*, vol. 81, no. 9, pp. 1368–70, Sep. 1994.
- [2] R. J. Stein, W. M. White, R. K. Goel, B. H. Irwin, G. P. Haber, and J. H. Kaouk, "Robotic laparoendoscopic single-site surgery using GelPort as the access platform.," *Eur. Urol.*, vol. 57, no. 1, pp. 132–6, Jan. 2010.
- [3] A. Iannelli, A. S. Schneck, and J. Gugenheim, "Single-incision laparoscopic cholecystectomy: is it more than a challenge?," *Surg. Endosc.*, vol. 25, no. 3, p. 978, Mar. 2011.
- [4] I. J. Park, G.-S. Choi, K.-H. Lim, B.-M. Kang, and S.-H. Jun, "Multidimensional analysis of the learning curve for laparoscopic colorectal surgery: lessons from 1,000 cases of laparoscopic colorectal surgery.," *Surg. Endosc.*, vol. 23, no. 4, pp. 839–46, Apr. 2009.
- [5] C. P. Delaney, *Operative Techniques in Laparoscopic Colorectal Surgery*. Wolters Kluwer Health, 2013, p. 248.
- [6] A. N. Kalloo, V. K. Singh, S. B. Jagannath, H. Niiyama, S. L. Hill, C. A. Vaughn, C. A. Magee, and S. V Kantsevov, "Flexible transgastric peritoneoscopy: a novel approach to diagnostic and therapeutic interventions in the peritoneal cavity.," *Gastrointest. Endosc.*, vol. 60, no. 1, pp. 114–7, Jul. 2004.
- [7] C. R. Tracy, J. D. Raman, J. A. Cadeddu, and A. Rane, "Laparoendoscopic single-site surgery in urology: where have we been and where are we heading?," *Nat. Clin. Pract. Urol.*, vol. 5, no. 10, pp. 561–8, Oct. 2008.
- [8] M. J. Mack, "Minimally Invasive and Robotic Surgery," *JAMA*, vol. 285, no. 5, p. 568, Feb. 2001.
- [9] M. J. Mack, R. J. Aronoff, T. E. Acuff, M. B. Douthit, R. T. Bowman, and W. H. Ryan, "Present role of thoracoscopy in the diagnosis and treatment of diseases of the chest.," *Ann. Thorac. Surg.*, vol. 54, no. 3, pp. 403–8; discussion 407–9, Sep. 1992.
- [10] S. Horgan and D. Vanuno, "Robots in laparoscopic surgery.," *J. Laparoendosc. Adv. Surg. Tech. A*, vol. 11, no. 6, pp. 415–9, Dec. 2001.
- [11] J. W. Hazey, V. K. Narula, D. B. Renton, K. M. Reavis, C. M. Paul, K. E. Hinshaw, P. Muscarella, E. C. Ellison, and W. S. Melvin, "Natural-orifice

- transgastric endoscopic peritoneoscopy in humans: Initial clinical trial.," *Surg. Endosc.*, vol. 22, no. 1, pp. 16–20, Jan. 2008.
- [12] H. Ross, S. Steele, M. Whiteford, S. Lee, M. Albert, M. Mutch, D. Rivadeneira, and P. Marcello, "Early multi-institution experience with single-incision laparoscopic colectomy.," *Dis. Colon Rectum*, vol. 54, no. 2, pp. 187–92, Feb. 2011.
- [13] K. Ahmed, T. T. Wang, V. M. Patel, K. Nagpal, J. Clark, M. Ali, S. Deeba, H. Ashrafian, A. Darzi, T. Athanasiou, and P. Paraskeva, "The role of single-incision laparoscopic surgery in abdominal and pelvic surgery: a systematic review.," *Surg. Endosc.*, vol. 25, no. 2, pp. 378–96, Feb. 2011.
- [14] R. H. Taylor, "A Perspective on Medical Robotics," *Proc. IEEE*, vol. 94, no. 9, pp. 1652–1664, Sep. 2006.
- [15] R. M. Satava, "Surgical robotics: the early chronicles: a personal historical perspective.," *Surg. Laparosc. Endosc. Percutan. Tech.*, vol. 12, no. 1, pp. 6–16, Feb. 2002.
- [16] K. Moorthy, Y. Munz, A. Dosis, J. Hernandez, S. Martin, F. Bello, T. Rockall, and A. Darzi, "Dexterity enhancement with robotic surgery.," *Surg. Endosc.*, vol. 18, no. 5, pp. 790–5, May 2004.
- [17] F. Corcione, C. Esposito, D. Cuccurullo, A. Settembre, N. Miranda, F. Amato, F. Pirozzi, and P. Caiazzo, "Advantages and limits of robot-assisted laparoscopic surgery: preliminary experience.," *Surg. Endosc.*, vol. 19, no. 1, pp. 117–9, Jan. 2005.
- [18] G. H. Ballantyne, "Robotic surgery, telerobotic surgery, telepresence, and telementoring. Review of early clinical results.," *Surg. Endosc.*, vol. 16, no. 10, pp. 1389–402, Oct. 2002.
- [19] S. H. B. and M.D., *Robot Surgery*. InTech, 2010.
- [20] "Intuitive Surgical - Media - Press Release." [Online]. Available: <http://investor.intuitivesurgical.com/phoenix.zhtml?c=122359&p=irol-newsArticle&ID=1914477>. [Accessed: 06-Jul-2014].
- [21] C. A. Nelson, X. Zhang, B. C. Shah, M. R. Goede, and D. Oleynikov, "Multipurpose surgical robot as a laparoscope assistant.," *Surg. Endosc.*, vol. 24, no. 7, pp. 1528–32, Jul. 2010.
- [22] M. J. H. Lum, D. C. W. Friedman, G. Sankaranarayanan, H. King, K. Fodero, R. Leuschke, B. Hannaford, J. Rosen, and M. N. Sinanan, "The RAVEN: Design and

- Validation of a Telesurgery System,” *Int. J. Rob. Res.*, vol. 28, no. 9, pp. 1183–1197, May 2009.
- [23] U. Hagn, R. Konietzschke, A. Tobergte, M. Nickl, S. Jörg, B. Kübler, G. Passig, M. Gröger, F. Fröhlich, U. Seibold, L. Le-Tien, A. Albu-Schäffer, A. Nothhelfer, F. Hacker, M. Grebenstein, and G. Hirzinger, “DLR MiroSurge: a versatile system for research in endoscopic telesurgery.,” *Int. J. Comput. Assist. Radiol. Surg.*, vol. 5, no. 2, pp. 183–93, Mar. 2010.
- [24] S.-K. Kim, W.-H. Shin, S.-Y. Ko, J. Kim, and D.-S. Kwon, “Design of a compact 5-DOF surgical robot of a spherical mechanism: CURES,” in *2008 IEEE/ASME International Conference on Advanced Intelligent Mechatronics*, 2008, pp. 990–995.
- [25] A. Tobergte, P. Helmer, U. Hagn, P. Rouiller, S. Thielmann, S. Grange, A. Albu-Schäffer, F. Conti, and G. Hirzinger, “The sigma.7 haptic interface for MiroSurge: A new bi-manual surgical console,” in *2011 IEEE/RSJ International Conference on Intelligent Robots and Systems*, 2011, pp. 3023–3030.
- [26] M. E. Rentschler, J. Dumpert, S. R. Platt, S. M. Farritor, and D. Oleynikov, “Mobile in vivo biopsy and camera robot.,” *Stud. Health Technol. Inform.*, vol. 119, pp. 449–54, Jan. 2006.
- [27] S. R. Platt, J. A. Hawks, and M. E. Rentschler, “Vision and task assistance using modular wireless in vivo surgical robots.,” *IEEE Trans. Biomed. Eng.*, vol. 56, no. 6, pp. 1700–10, Jun. 2009.
- [28] J. Midday, *Material Handling System for Robotic Natural Orifice Surgery*. 2012.
- [29] W. J. Chin, C. A. Nelson, and C. M. Seow, “Articulated Mechanism Design and Kinematics for Natural Orifice Translumenal Endoscopic Surgery Robot,” in *Volume 2: Biomedical and Biotechnology Engineering; Nanoengineering for Medicine and Biology*, 2011, pp. 459–467.
- [30] A. Pourghodrat, C. Nelson, and D. Oleynikov, “Electro-Hydraulic Robotic Manipulator with Multiple Instruments for Minimally Invasive Surgery,” *J. Med. Device.*, Mar. 2014.
- [31] M. Kroh, K. El-Hayek, S. Rosenblatt, B. Chand, P. Escobar, J. Kaouk, and S. Chalikonda, “First human surgery with a novel single-port robotic system: cholecystectomy using the da Vinci Single-Site platform.,” *Surg. Endosc.*, vol. 25, no. 11, pp. 3566–73, Nov. 2011.
- [32] “Intuitive Surgical - Media - Press Release.” [Online]. Available: <http://investor.intuitivesurgical.com/phoenix.zhtml?c=122359&p=irol-newsArticle&ID=1920546&highlight=>. [Accessed: 07-Jul-2014].

- [33] M. Piccigallo, U. Scarfogliero, C. Quaglia, G. Petroni, P. Valdastri, A. Menciassi, and P. Dario, "Design of a Novel Bimanual Robotic System for Single-Port Laparoscopy," *IEEE/ASME Trans. Mechatronics*, vol. 15, no. 6, pp. 871–878, Dec. 2010.
- [34] N. A. Wood, *Design and Analysis of Dexterous in Vivo Robots for NOTES*. University of Nebraska--Lincoln, 2008.
- [35] A. C. Lehman, "Miniature in vivo robots for minimally invasive surgery," 2012.
- [36] R. McCormick, "Six Degree Of Freedom Miniature In Vivo Robot For Laparoendoscopic Single-Site Surgery," 2011.
- [37] J. Hawks, "Improved Mobile Wireless In Vivo Surgical Robots: Modular Design, Experimental Results, And Analysis," 2010.
- [38] T. Wortman, "Design, Analysis, And Testing Of In Vivo Surgical Robots," 2011.
- [39] J. Mondry, *Design and Development of a Four Degree of Freedom In Vivo Surgical Robot for Laparoendoscopic Single-Site Surgery*. 2012.
- [40] M. E. Rentschler, *In vivo abdominal surgical robotics: Tissue mechanics modeling, robotic design, experimentation, and analysis*. 2006, pp. 1 – 164.
- [41] J. Dumpert, *Towards Supervised Autonomous Task Completion Using an in vivo Surgical Robot*. 2009.
- [42] E. J. Markvicka, R. L. McCormick, T. P. Frederick, J. R. Bartels, S. M. Farritor, and D. Oleynikov, "Multi-Quadrant Surgical Robot for Single Incision Laparoscopic Colectomy," in *Volume 6A: 37th Mechanisms and Robotics Conference*, 2013, p. V06AT07A013.
- [43] T. D. Wortman, A. Meyer, O. Dolghi, A. C. Lehman, R. L. McCormick, S. M. Farritor, and D. Oleynikov, "Miniature surgical robot for laparoendoscopic single-incision colectomy.," *Surg. Endosc.*, vol. 26, no. 3, pp. 727–31, Mar. 2012.
- [44] E. Markvicka, K. Lackas, T. Frederick, J. Bartels, S. Farritor, and D. Oleynikov, "Gross Positioning System for In Vivo Surgical Devices," *J. Med. Device.*, vol. 7, no. 3, p. 030922, Jul. 2013.
- [45] M. Lum, D. Trimble, J. Rosen, K. Fodero, H. King, S. Ganesh, J. Doshier, R. Leuschke, B. Martin-Anderson, M. Sinanan, and B. Hannaford, "Multidisciplinary Approach for Developing a New Minimally Invasive Surgical Robotic System," in *Biomedical Robotics and Biomechatronics, BioRob 2006. The First IEEE / RAS-EMBS International Conference on Biomedical Robotics and Biomechatronics*, 2006, pp. 841–846.

- [46] J. Rosen, J. D. Brown, M. Barreca, L. Chang, B. Hannaford, and M. Sinanan, "The Blue DRAGON--a system for monitoring the kinematics and the dynamics of endoscopic tools in minimally invasive surgery for objective laparoscopic skill assessment.," *Stud. Health Technol. Inform.*, vol. 85, pp. 412–8, Jan. 2002.
- [47] M. J. H. Lum, J. Rosen, M. N. Sinanan, and B. Hannaford, "Optimization of a spherical mechanism for a minimally invasive surgical robot: theoretical and experimental approaches.," *IEEE Trans. Biomed. Eng.*, vol. 53, no. 7, pp. 1440–5, Jul. 2006.
- [48] H. de Visser, E. A. M. Heijnsdijk, J. L. Herder, and P. V Pistecky, "Forces and displacements in colon surgery.," *Surg. Endosc.*, vol. 16, no. 10, pp. 1426–30, Oct. 2002.
- [49] R. L. McCormick, T. D. Wortman, K. W. Strabala, T. Frederick, S. M. Farritor, and D. Oleynikov, "KINEMATIC AND WORKSPACE COMPARISON OF FOUR AND FIVE DEGREE OF FREEDOM MINIATURE IN VIVO SURGICAL ROBOT," in *Proceedings of the 2011 Design of Medical Devices Conference*, 2011.
- [50] A. C. Lehman, J. Dumpert, N. A. Wood, L. Redden, A. Q. Visty, S. Farritor, B. Varnell, and D. Oleynikov, "Natural orifice cholecystectomy using a miniature robot.," *Surg. Endosc.*, vol. 23, no. 2, pp. 260–6, Feb. 2009.
- [51] J. J. Craig, *Introduction to Robotics: Mechanics and Control*. Pearson Education, Incorporated, 2005, p. 400.
- [52] "EC 16 Ø16 mm, brushless, 60 Watt, sterilizable, with Hall sensors, 394216." [Online]. Available: <http://www.maxonmotorusa.com/maxon/view/product/motor/ecmotor/ec/ec16/394216>. [Accessed: 14-Jul-2014].
- [53] T. Yoshikawa, "Manipulability of Robotic Mechanisms," *Int. J. Rob. Res.*, vol. 4, no. 2, pp. 3–9, Jun. 1985.
- [54] K. Gilpin, A. Knaian, and D. Rus, "Robot pebbles: One centimeter modules for programmable matter through self-disassembly," in *2010 IEEE International Conference on Robotics and Automation*, 2010, pp. 2485–2492.
- [55] L. P. JD Carlson, J Kowalczyk, E Psota, "A compact high-definition low-cost digital stereoscopic video camera for rapid robotic surgery development.," in *In MMVR*, 2012, pp. 92–96.
- [56] J. R. Bartels, "Development Of Distributed Motor Control And Haptic," 2013.

- [57] “Everett Charles Technologies.” [Online]. Available: <http://www.ectinfo.com/>. [Accessed: 31-Jul-2014].
- [58] T. Frederick, “Insertion of a surgical robot into an insufflated abdominal cavity,” 2012.
- [59] E. Markvicka, “Gross Positioning,” 2014. [Online]. Available: <https://www.youtube.com/watch?v=Y2iRheXL06o&feature=youtu.be>. [Accessed: 01-Aug-2014].

## Appendix A. Kinematic Analysis

with linearAlgebra

$$T1 := \text{matrix}(4, 4, [1, 0, 0, 0, 0, \cos(t1), -\sin(t1), 0, 0, \sin(t1), \cos(t1), 0, 0, 0, 0, 1]) \quad (1)$$

$$\begin{bmatrix} 1 & 0 & 0 & 0 \\ 0 & \cos(t1) & -\sin(t1) & 0 \\ 0 & \sin(t1) & \cos(t1) & 0 \\ 0 & 0 & 0 & 1 \end{bmatrix} \quad (2)$$

$$T2 := \text{matrix}(4, 4, [\cos(t2), 0, \sin(t2), 0, 0, 1, 0, 0, -\sin(t2), 0, \cos(t2), -\text{Offset}, 0, 0, 0, 1])$$

$$\begin{bmatrix} \cos(t2) & 0 & \sin(t2) & 0 \\ 0 & 1 & 0 & 0 \\ -\sin(t2) & 0 & \cos(t2) & -\text{Offset} \\ 0 & 0 & 0 & 1 \end{bmatrix} \quad (3)$$

$$T3 := \text{matrix}(4, 4, [\cos(t3), 0, \sin(t3), 0, 0, 1, 0, 0, -\sin(t3), 0, \cos(t3), -L1, 0, 0, 0, 1])$$

$$\begin{bmatrix} \cos(t3) & 0 & \sin(t3) & 0 \\ 0 & 1 & 0 & 0 \\ -\sin(t3) & 0 & \cos(t3) & -L1 \\ 0 & 0 & 0 & 1 \end{bmatrix} \quad (4)$$

$$T4 := \text{matrix}(4, 4, [1, 0, 0, 0, 0, 1, 0, 0, 0, 0, 1, -L2, 0, 0, 0, 1])$$

$$\begin{bmatrix} 1 & 0 & 0 & 0 \\ 0 & 1 & 0 & 0 \\ 0 & 0 & 1 & -L2 \\ 0 & 0 & 0 & 1 \end{bmatrix} \quad (5)$$

$$T := \text{evalm}(T1 \& \cdot T2 \& \cdot T3 \& \cdot T4)$$

$$\begin{aligned} & [[\cos(t2) \cos(t3) - \sin(t2) \sin(t3), 0, \cos(t2) \sin(t3) + \sin(t2) \cos(t3), -(\cos(t2) \sin(t3) \\ & \quad + \sin(t2) \cos(t3)) L2 - \sin(t2) L1], \\ & [\sin(t1) \sin(t2) \cos(t3) + \sin(t1) \cos(t2) \sin(t3), \cos(t1), \sin(t1) \sin(t2) \sin(t3) \\ & \quad - \sin(t1) \cos(t2) \cos(t3), -(\sin(t1) \sin(t2) \sin(t3) - \sin(t1) \cos(t2) \cos(t3)) L2 \\ & \quad + \sin(t1) \cos(t2) L1 + \sin(t1) \text{Offset}], \\ & [-\cos(t1) \sin(t2) \cos(t3) - \cos(t1) \cos(t2) \sin(t3), \sin(t1), -\cos(t1) \sin(t2) \sin(t3) \\ & \quad + \cos(t1) \cos(t2) \cos(t3), -(-\cos(t1) \sin(t2) \sin(t3) + \cos(t1) \cos(t2) \cos(t3)) L2 \\ & \quad - \cos(t1) \cos(t2) L1 - \cos(t1) \text{Offset}], \\ & [0, 0, 0, 1]] \end{aligned} \quad (6)$$

$$X := T[1, 4] - (\cos(t2) \sin(t3) + \sin(t2) \cos(t3)) L2 - \sin(t2) L1 \quad (7)$$

$$Y := T[2, 4] - (\sin(t1) \sin(t2) \sin(t3) - \sin(t1) \cos(t2) \cos(t3)) L2 + \sin(t1) \cos(t2) L1 + \sin(t1) \text{Offset} \quad (8)$$

$$Z := T[3, 4] - (-\cos(t1) \sin(t2) \sin(t3) + \cos(t1) \cos(t2) \cos(t3)) L2 - \cos(t1) \cos(t2) L1 - \cos(t1) \text{Offset} \quad (9)$$



$$J1 := (t1, t2, t3) \rightarrow X; \quad (t1, t2, t3) \rightarrow X \quad (10)$$

$$J2 := (t1, t2, t3) \rightarrow Y; \quad (t1, t2, t3) \rightarrow Y \quad (11)$$

$$J3 := (t1, t2, t3) \rightarrow Z; \quad (t1, t2, t3) \rightarrow Z \quad (12)$$

$$J11 := \text{diff}(J1(t1, t2, t3), t1); \quad 0 \quad (13)$$

$$J12 := \text{diff}(J1(t1, t2, t3), t2); \quad -(\cos(t2) \cos(t3) - \sin(t2) \sin(t3)) L2 - \cos(t2) L1 \quad (14)$$

$$J13 := \text{diff}(J1(t1, t2, t3), t3); \quad -(\cos(t2) \cos(t3) - \sin(t2) \sin(t3)) L2 \quad (15)$$

$$J21 := \text{diff}(J2(t1, t2, t3), t1); \quad -(\cos(t1) \sin(t2) \sin(t3) - \cos(t1) \cos(t2) \cos(t3)) L2 + \cos(t1) \cos(t2) L1 + \cos(t1) \text{Offset} \quad (16)$$

$$J22 := \text{diff}(J2(t1, t2, t3), t2); \quad -(\sin(t1) \sin(t2) \cos(t3) + \sin(t1) \cos(t2) \sin(t3)) L2 - \sin(t1) \sin(t2) L1 \quad (17)$$

$$J23 := \text{diff}(J2(t1, t2, t3), t3); \quad -(\sin(t1) \sin(t2) \cos(t3) + \sin(t1) \cos(t2) \sin(t3)) L2 \quad (18)$$

$$J31 := \text{diff}(J3(t1, t2, t3), t1); \quad -(\sin(t1) \sin(t2) \sin(t3) - \sin(t1) \cos(t2) \cos(t3)) L2 + \sin(t1) \cos(t2) L1 + \sin(t1) \text{Offset} \quad (19)$$

$$J32 := \text{diff}(J3(t1, t2, t3), t2); \quad -(-\cos(t1) \sin(t2) \cos(t3) - \cos(t1) \cos(t2) \sin(t3)) L2 + \cos(t1) \sin(t2) L1 \quad (20)$$

$$J33 := \text{diff}(J3(t1, t2, t3), t3); \quad -(-\cos(t1) \sin(t2) \cos(t3) - \cos(t1) \cos(t2) \sin(t3)) L2 \quad (21)$$

$$\text{Jac} := \text{matrix}(3, 3, [J11, J12, J13, J21, J22, J23, J31, J32, J33]) \quad (22)$$

$$[[0, -(\cos(t2) \cos(t3) - \sin(t2) \sin(t3)) L2 - \cos(t2) L1, -(\cos(t2) \cos(t3) - \sin(t2) \sin(t3)) L2,$$

$$[-(\cos(t1) \sin(t2) \sin(t3) - \cos(t1) \cos(t2) \cos(t3)) L2 + \cos(t1) \cos(t2) L1$$

$$+ \cos(t1) \text{Offset}, -(\sin(t1) \sin(t2) \cos(t3) + \sin(t1) \cos(t2) \sin(t3)) L2$$

$$- \sin(t1) \sin(t2) L1, -(\sin(t1) \sin(t2) \cos(t3) + \sin(t1) \cos(t2) \sin(t3)) L2],$$

$$[-(\sin(t1) \sin(t2) \sin(t3) - \sin(t1) \cos(t2) \cos(t3)) L2 + \sin(t1) \cos(t2) L1$$

$$+ \sin(t1) \text{Offset}, -(-\cos(t1) \sin(t2) \cos(t3) - \cos(t1) \cos(t2) \sin(t3)) L2$$

$$+ \cos(t1) \sin(t2) L1, -(-\cos(t1) \sin(t2) \cos(t3) - \cos(t1) \cos(t2) \sin(t3)) L2]]$$

transpose

$$[[0, -(\cos(t1) \sin(t2) \sin(t3) - \cos(t1) \cos(t2) \cos(t3)) L2 + \cos(t1) \cos(t2) L1 \quad (23)$$

$$+ \cos(t1) \text{Offset}, -(\sin(t1) \sin(t2) \sin(t3) - \sin(t1) \cos(t2) \cos(t3)) L2$$

$$+ \sin(t1) \cos(t2) L1 + \sin(t1) \text{Offset}],$$

$$[-(\cos(t2) \cos(t3) - \sin(t2) \sin(t3)) L2 - \cos(t2) L1, -(\sin(t1) \sin(t2) \cos(t3)$$

$$+ \sin(t1) \cos(t2) \sin(t3)) L2 - \sin(t1) \sin(t2) L1, -(-\cos(t1) \sin(t2) \cos(t3)$$

$$- \cos(t1) \cos(t2) \sin(t3)) L2 + \cos(t1) \sin(t2) L1],$$

$$[-(\cos(t2) \cos(t3) - \sin(t2) \sin(t3)) L2, -(\sin(t1) \sin(t2) \cos(t3)$$

$$+ \sin(t1) \cos(t2) \sin(t3)) L2, -(-\cos(t1) \sin(t2) \cos(t3) - \cos(t1) \cos(t2) \sin(t3)) L2]]$$

inverse

$$\begin{aligned}
& \left[ \left[ 0, -\frac{\cos(t_2) \sin(t_3) + \sin(t_2) \cos(t_3)}{(\sin(t_2)^2 + \cos(t_2)^2) L_1 \sin(t_3)}, \right. \right. \\
& \quad \left. \left. \frac{\cos(t_3) \sin(t_2) L_2 + \cos(t_2) \sin(t_3) L_2 + \sin(t_2) L_1}{(\sin(t_2)^2 + \cos(t_2)^2) L_1 L_2 \sin(t_3)} \right] \right] \\
& \left[ (\cos(t_1)) / (-L_2 \cos(t_1)^2 \sin(t_2) \sin(t_3) + L_2 \cos(t_1)^2 \cos(t_2) \cos(t_3)) \right. \\
& \quad - L_2 \sin(t_2) \sin(t_3) \sin(t_1)^2 + L_2 \cos(t_2) \cos(t_3) \sin(t_1)^2 + L_1 \cos(t_1)^2 \cos(t_2) \\
& \quad \left. + L_1 \cos(t_2) \sin(t_1)^2 + \cos(t_1)^2 \text{Offset} + \sin(t_1)^2 \text{Offset} \right), \\
& - ((\sin(t_2) \sin(t_3) - \cos(t_2) \cos(t_3)) \sin(t_1)) / ((\cos(t_1)^2 \sin(t_2)^2 \\
& \quad + \cos(t_1)^2 \cos(t_2)^2 + \sin(t_2)^2 \sin(t_1)^2 + \cos(t_2)^2 \sin(t_1)^2) L_1 \sin(t_3)), \\
& - ((-\sin(t_3) \sin(t_2) L_2 + L_2 \cos(t_2) \cos(t_3) + \cos(t_2) L_1) \sin(t_1)) / \\
& \quad ((\cos(t_1)^2 \sin(t_2)^2 + \cos(t_1)^2 \cos(t_2)^2 + \sin(t_2)^2 \sin(t_1)^2 \\
& \quad + \cos(t_2)^2 \sin(t_1)^2) L_1 L_2 \sin(t_3))), \\
& \left[ (\sin(t_1)) / (-L_2 \cos(t_1)^2 \sin(t_2) \sin(t_3) + L_2 \cos(t_1)^2 \cos(t_2) \cos(t_3)) \right. \\
& \quad - L_2 \sin(t_2) \sin(t_3) \sin(t_1)^2 + L_2 \cos(t_2) \cos(t_3) \sin(t_1)^2 + L_1 \cos(t_1)^2 \cos(t_2) \\
& \quad \left. + L_1 \cos(t_2) \sin(t_1)^2 + \cos(t_1)^2 \text{Offset} + \sin(t_1)^2 \text{Offset} \right), \\
& ((\sin(t_2) \sin(t_3) - \cos(t_2) \cos(t_3)) \cos(t_1)) / ((\cos(t_1)^2 \sin(t_2)^2 + \cos(t_1)^2 \cos(t_2)^2 \\
& \quad + \sin(t_2)^2 \sin(t_1)^2 + \cos(t_2)^2 \sin(t_1)^2) L_1 \sin(t_3)), \\
& ((-\sin(t_3) \sin(t_2) L_2 + L_2 \cos(t_2) \cos(t_3) + \cos(t_2) L_1) \cos(t_1)) / \\
& \quad ((\cos(t_1)^2 \sin(t_2)^2 + \cos(t_1)^2 \cos(t_2)^2 + \sin(t_2)^2 \sin(t_1)^2 \\
& \quad + \cos(t_2)^2 \sin(t_1)^2) L_1 L_2 \sin(t_3))) ] ] \\
& \xrightarrow{\text{to matlab}} \\
& \text{cg} = [0 -(\cos(t_2) * \sin(t_3) + \sin(t_2) * \cos(t_3)) / (\sin(t_2) ^ 2 + \\
& \cos(t_2) ^ 2) / L_1 / \sin(t_3) (\cos(t_3) * \sin(t_2) * L_2 + \cos(t_2) * \\
& \sin(t_3) * L_2 + \sin(t_2) * L_1) / (\sin(t_2) ^ 2 + \cos(t_2) ^ 2) / L_1 / \\
& L_2 / \sin(t_3); \cos(t_1) / (-L_2 * \cos(t_1) ^ 2 * \sin(t_2) * \sin(t_3) + \\
& L_2 * \cos(t_1) ^ 2 * \cos(t_2) * \cos(t_3) - L_2 * \sin(t_2) * \sin(t_3) * \\
& \sin(t_1) ^ 2 + L_2 * \cos(t_2) * \cos(t_3) * \sin(t_1) ^ 2 + L_1 * \cos(t_1) \\
& ^ 2 * \cos(t_2) + L_1 * \cos(t_2) * \sin(t_1) ^ 2 + \cos(t_1) ^ 2 * \text{Offset} \\
& + \sin(t_1) ^ 2 * \text{Offset}) -(\sin(t_2) * \sin(t_3) - \cos(t_2) * \cos(t_3)) \\
& * \sin(t_1) / (\cos(t_1) ^ 2 * \sin(t_2) ^ 2 + \cos(t_1) ^ 2 * \cos(t_2) ^ 2 + \\
& \sin(t_2) ^ 2 * \sin(t_1) ^ 2 + \cos(t_2) ^ 2 * \sin(t_1) ^ 2) L_1 \sin(t_3) \\
& -((-\sin(t_3) \sin(t_2) L_2 + L_2 \cos(t_2) \cos(t_3) + \cos(t_2) L_1) \sin(t_1)) / \\
& ((\cos(t_1) ^ 2 \sin(t_2) ^ 2 + \cos(t_1) ^ 2 \cos(t_2) ^ 2 + \sin(t_2) ^ 2 \sin(t_1) ^ 2 \\
& + \cos(t_2) ^ 2 \sin(t_1) ^ 2) L_1 L_2 \sin(t_3))] ]
\end{aligned}$$

```

2 + sin(t2) ^ 2 * sin(t1) ^ 2 + cos(t2) ^ 2 * sin(t1) ^ 2) / L1 /
sin(t3) -(-sin(t3) * sin(t2) * L2 + L2 * cos(t2) * cos(t3) + cos
(t2) * L1) * sin(t1) / (cos(t1) ^ 2 * sin(t2) ^ 2 + cos(t1) ^ 2 *
cos(t2) ^ 2 + sin(t2) ^ 2 * sin(t1) ^ 2 + cos(t2) ^ 2 * sin(t1) ^
2) / L1 / L2 / sin(t3); sin(t1) / (-L2 * cos(t1) ^ 2 * sin(t2) *
sin(t3) + L2 * cos(t1) ^ 2 * cos(t2) * cos(t3) - L2 * sin(t2) *
sin(t3) * sin(t1) ^ 2 + L2 * cos(t2) * cos(t3) * sin(t1) ^ 2 + L1
* cos(t1) ^ 2 * cos(t2) + L1 * cos(t2) * sin(t1) ^ 2 + cos(t1) ^
2 * Offset + sin(t1) ^ 2 * Offset) (sin(t2) * sin(t3) - cos(t2) *
cos(t3)) * cos(t1) / (cos(t1) ^ 2 * sin(t2) ^ 2 + cos(t1) ^ 2 *
cos(t2) ^ 2 + sin(t2) ^ 2 * sin(t1) ^ 2 + cos(t2) ^ 2 * sin(t1) ^
2) / L1 / sin(t3) (-sin(t3) * sin(t2) * L2 + L2 * cos(t2) * cos
(t3) + cos(t2) * L1) * cos(t1) / (cos(t1) ^ 2 * sin(t2) ^ 2 + cos
(t1) ^ 2 * cos(t2) ^ 2 + sin(t2) ^ 2 * sin(t1) ^ 2 + cos(t2) ^ 2
* sin(t1) ^ 2) / L1 / L2 / sin(t3)];

```

## Appendix B. Theoretical Abilities and Supporting Material

```

clear all
close all
clc
clf

%% Joint Parameters
theta2min=-90*pi/180;
theta2max=0*pi/180;
theta2step=.25*pi/180;

theta3min=0*pi/180;
theta3max=135*pi/180;
theta3step=.25*pi/180;

%% Joint Length
OffsetZ = -.42*25.4;
OffsetX = 6;
L1 = 3.445*25.4;
L2 = 3.75*25.4;

%%%%%%%%%%%%%%%%%%%%%%%%%%%%%%%%%%%%%%%%%%%%%%%%%%%%%%%%%%%%%%%%%%%%%%%%
%%
% T = (stall torque)*(Motor Gear Head Ratio)*(External Gear Head
% Ratio)*(Motor Gear Head Efficiency)
% w = ((no load speed)/(Motor Gear Head Ratio))*(1/(External Gear Head
% Ratio))*(rpm to rad/sec conversion)
%%%%%%%%%%%%%%%%%%%%%%%%%%%%%%%%%%%%%%%%%%%%%%%%%%%%%%%%%%%%%%%%%%%%%%%%
%%

% Motor 1: 315171 + 218418 64:1 (Maxon Motors USA)
% Motor 2: 0620K006B + 06/1K 1024:1 (MicroMo)
% Motor 3: 0620K006B + 06/1K 1024:1 (MicroMo)

%% Motor Specs [mNm] 271.2320 657.8176 657.8176
T(1) = (1.63)*(256)*(1/1)*(.65);
T(2) = (.73)*(1024)*(16/10)*(.55);
T(3) = (.73)*(1024)*(16/10)*(.55);

%% Motor Speed [rad/s]
wm(1) = ((45600)/(256))*(1/60)*(2*pi);
wm(2) = ((46500)/(1024))*(10/16)*(1/60)*(2*pi);
wm(3) = ((46500)/(1024))*(10/16)*(1/60)*(2*pi);

n=0; m=0;
for t2= theta2min:theta2step:theta2max
    m=m+1;
    n=0;
    for t3= theta3min:theta3step:theta3max
        n=n+1;
    end
end

```

```

%% Forward Kinematics with t1 = 0, YF = 0
XF(m,n) = -(cos(t2)*sin(t3) + sin(t2)*cos(t3))*L2 - sin(t2)*L1
+ OffsetX;
ZF(m,n) = (sin(t2)*sin(t3) - cos(t2)*cos(t3))*L2-cos(t2)*L1 +
OffsetZ;

%% Jacobian Calculation Frame Zero, t1 = 0
J = [0 -(cos(t2) * cos(t3) - sin(t2) * sin(t3)) * L2 - cos(t2)
* L1 -(cos(t2) * cos(t3) - sin(t2) * sin(t3)) * L2; -(sin(t2) * sin(t3)
- cos(t2) * cos(t3)) * L2 + cos(t2) * L1 0 0; 0 -(-sin(t2) * cos(t3) -
cos(t2) * sin(t3)) * L2 + sin(t2) * L1 -(-sin(t2) * cos(t3) - cos(t2) *
sin(t3)) * L2;];

%% Jacobian Transpose Calculation Frame Zero, t1 = 0
Jt = [0 -(sin(t2) * sin(t3) - cos(t2) * cos(t3)) * L2 + cos(t2)
* L1 0; -(cos(t2) * cos(t3) - sin(t2) * sin(t3)) * L2 - cos(t2) * L1 0
-(-sin(t2) * cos(t3) - cos(t2) * sin(t3)) * L2 + sin(t2) * L1; -
(cos(t2) * cos(t3) - sin(t2) * sin(t3)) * L2 0 -(-sin(t2) * cos(t3) -
cos(t2) * sin(t3)) * L2;];

%% Jacobian transpose, inverse
Jti = [0 -(cos(t2) * sin(t3) + sin(t2) * cos(t3)) / (cos(t2) ^
2 + sin(t2) ^ 2) / L1 / sin(t3) (L2 * cos(t2) * sin(t3) + L2 * cos(t3)
* sin(t2) + sin(t2) * L1) / (cos(t2) ^ 2 + sin(t2) ^ 2) / L1 / L2 /
sin(t3); 0.1e1 / (L2 * cos(t2) * cos(t3) - L2 * sin(t2) * sin(t3) +
cos(t2) * L1) 0 0; 0 -(cos(t2) * cos(t3) - sin(t2) * sin(t3)) /
(cos(t2) ^ 2 + sin(t2) ^ 2) / L1 / sin(t3) (L2 * cos(t2) * cos(t3) - L2
* sin(t2) * sin(t3) + cos(t2) * L1) / (cos(t2) ^ 2 + sin(t2) ^ 2) / L1
/ L2 / sin(t3);];

%% Manipulability Measure
w(m,n) = sqrt(abs(det(J*Jt)));

%% Force and Velocity
F = Jti*T'; % [mNm/mm]
Fx(m,n)=abs(F(1));
Fy(m,n)=abs(F(2));
Fz(m,n)=abs(F(3));

V = J*wm'; % [mm/sec]
Vx(m,n)=abs(V(1));
Vy(m,n)=abs(V(2));
Vz(m,n)=abs(V(3));
end
end

YF = zeros(size(XF));

%% Find Maximum Manipulability
maxw=max(max(w));

%% Normalize Manipulability
for m=1:size(w,1)
    for n=1:size(w,2)

```

```

        w(m,n)=w(m,n)/maxw;
    end
end

% Limit Maximum Force to 40 Nm, find minimum F and V
for m=1:size(Fx,1)
    for n=1:size(Fx,2)
        if Fx(m,n) > 40
            Fx(m,n) = 40;
        end
        if Fz(m,n) > 40
            Fz(m,n) = 40;
        end
        if Fy(m,n) > 40
            Fy(m,n) = 40;
        end
        Fmin(m,n) = min([Fx(m,n) Fy(m,n) Fz(m,n)]);
        Vmin(m,n) = min([Vx(m,n) Vy(m,n) Vz(m,n)]);
    end
end

%%%%%%%%%%%%%%%%%%%%%%%%%%%%%%%%%%%%%%%%%%%%%%%%%%%%%%%%%%%%%%%%%%%%%%%%
%% Plot Workspace Mesh
figure(1)

surface(ZF,XF,YF,w,'facecol','no','edgecol','interp','linewidth',2);
view(90,90)

colorbar;
colormap('default')
xlabel('Z [mm]')
ylabel('X [mm]')
zlabel('Y [mm]')
title('EB2 Workspace')
saveas(gcf,'EB2Workspace.jpg')
caxis([0 0.5]);
saveas(gcf,'EB2Workspacehalf.jpg')
%%%%%%%%%%%%%%%%%%%%%%%%%%%%%%%%%%%%%%%%%%%%%%%%%%%%%%%%%%%%%%%%%%%%%%%%
%% Plot Minimum Force Mesh
surface(ZF,XF,YF,Fmin,'facecol','no','edgecol','interp','linewidth',2);

%% view(1);
caxis([0.8 3]);
title('EB2 Minimum Force (N)')
saveas(gcf,'EB2MinF.jpg')
caxis([0 0.8]);
saveas(gcf,'EB2MinF0to8.jpg')
%%%%%%%%%%%%%%%%%%%%%%%%%%%%%%%%%%%%%%%%%%%%%%%%%%%%%%%%%%%%%%%%%%%%%%%%
%% Plot Fx Mesh
surface(ZF,XF,YF,Fx,'facecol','no','edgecol','interp','linewidth',2);

%% view(1);
caxis([0.8 10]);
title('EB2 Fx (N)')

```

```

saveas(gcf,'EB2Fx.jpg')
caxis([0 0.8]);
saveas(gcf,'EB2Fx0to8.jpg')
%%%%%%%%%%%%%%%%%%%%%%%%%%%%%%%%%%%%%%%%%%%%%%%%%%%%%%%%%%%%%%%%%%%%%%%%
%% Plot Fy Mesh
surface(ZF,XF,YF,Fy,'facecol','no','edgecol','interp','linewidth',2);

%% view(1);
caxis([0.8 4]);
title('EB2 Fy (N)')
saveas(gcf,'EB2Fy.jpg')
caxis([0 0.8]);
saveas(gcf,'EB2Fy0to8.jpg')
%%%%%%%%%%%%%%%%%%%%%%%%%%%%%%%%%%%%%%%%%%%%%%%%%%%%%%%%%%%%%%%%%%%%%%%%
%% Plot Fz Mesh
surface(ZF,XF,YF,Fz,'facecol','no','edgecol','interp','linewidth',2);

%% view(1);
caxis([2.2 10]);
title('EB2 Fz (N)')
saveas(gcf,'EB2Fz.jpg')
caxis([0 2.2]);
saveas(gcf,'EB2Fz0to22.jpg')
%%%%%%%%%%%%%%%%%%%%%%%%%%%%%%%%%%%%%%%%%%%%%%%%%%%%%%%%%%%%%%%%%%%%%%%%
%% Plot Minimum Velocity Mesh
surface(ZF,XF,YF,Vmin,'facecol','no','edgecol','interp','linewidth',2);

%% view(1);
caxis([70 150]);
title('EB2 Minimum Velocity (mm/sec)')
saveas(gcf,'EB2MinV.jpg')
caxis([0 70]);
saveas(gcf,'EB2MinV0270.jpg')
%%%%%%%%%%%%%%%%%%%%%%%%%%%%%%%%%%%%%%%%%%%%%%%%%%%%%%%%%%%%%%%%%%%%%%%%
%% Plot Vx Mesh
surface(ZF,XF,YF,Vx,'facecol','no','edgecol','interp','linewidth',2);

caxis([70 800]);
title('EB2 Vx (mm/sec)')
saveas(gcf,'EB2Vx.jpg')
caxis([0 70]);
saveas(gcf,'EB2Vx0270.jpg')
%%%%%%%%%%%%%%%%%%%%%%%%%%%%%%%%%%%%%%%%%%%%%%%%%%%%%%%%%%%%%%%%%%%%%%%%
%% Plot Vy Mesh
surface(ZF,XF,YF,Vy,'facecol','no','edgecol','interp','linewidth',2);

caxis([70 1000]);
title('EB2 Vy (mm/sec)')
saveas(gcf,'EB2Vy.jpg')
%%%%%%%%%%%%%%%%%%%%%%%%%%%%%%%%%%%%%%%%%%%%%%%%%%%%%%%%%%%%%%%%%%%%%%%%
%% Plot Vz Mesh
surface(ZF,XF,YF,Vz,'facecol','no','edgecol','interp','linewidth',2);

caxis([70 500]);
title('EB2 Vz (mm/sec)')
saveas(gcf,'EB2Vz.jpg')

```

```
caxis([0 70]);  
saveas(gcf, 'EB2Vz0270.jpg')
```



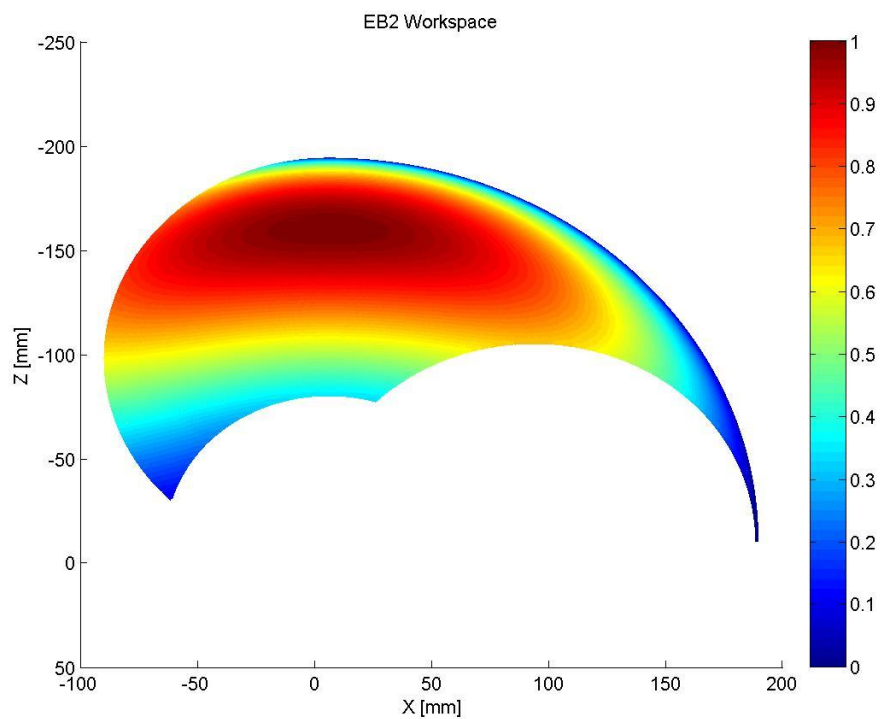


Figure 0.1: EB2.0 manipulability measure, right arm.

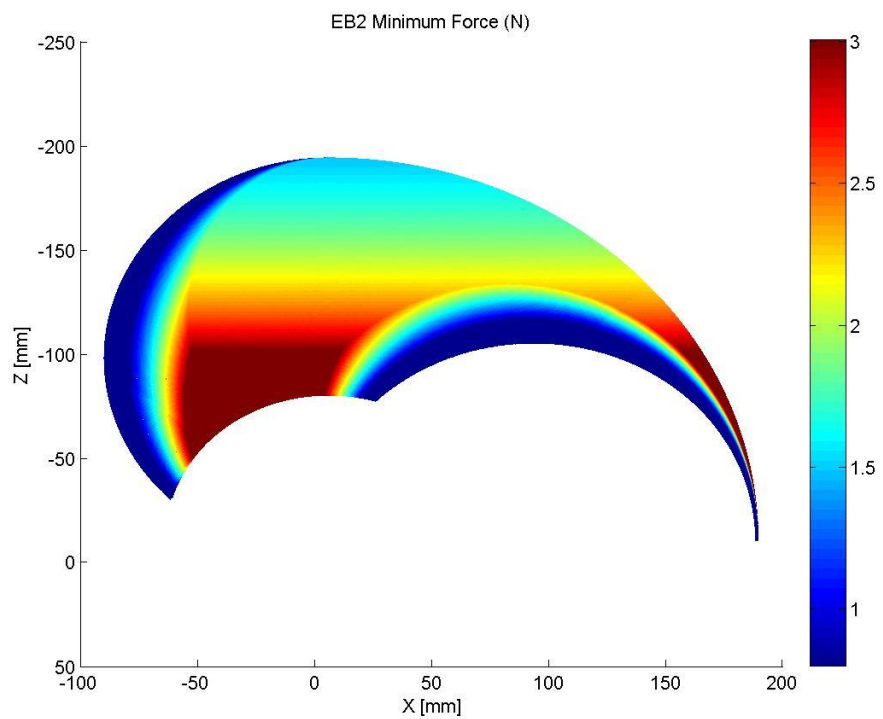


Figure 0.2: EB2.0 minimum static endpoint force, right arm.

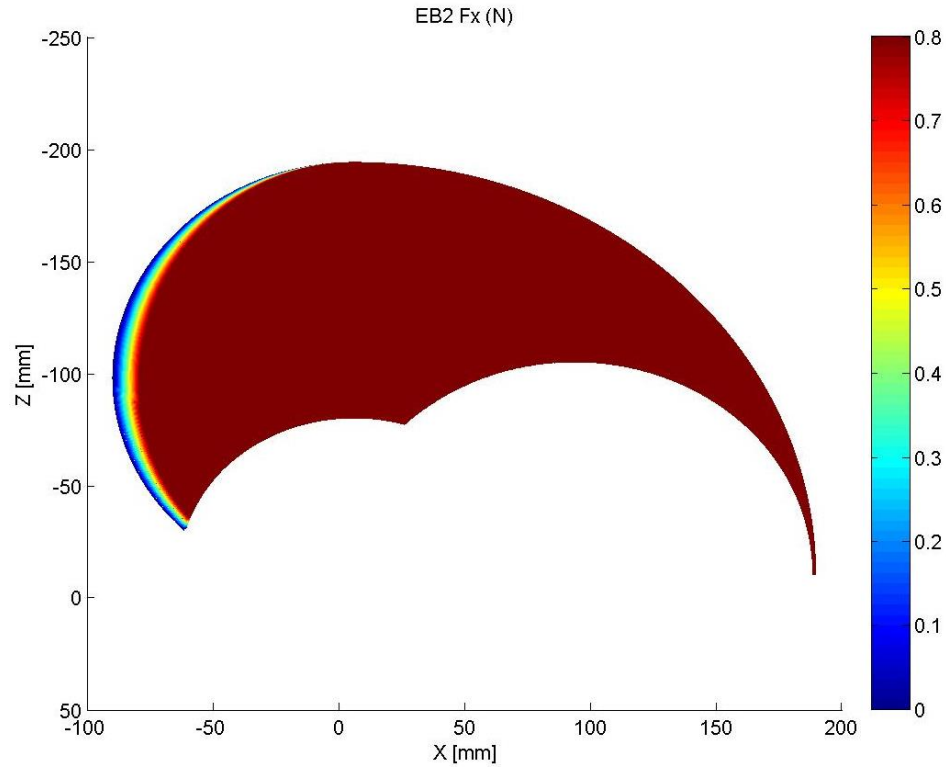


Figure 0.3: EB2.0 static endpoint force deficiencies in the X principal Cartesian axis, right arm.

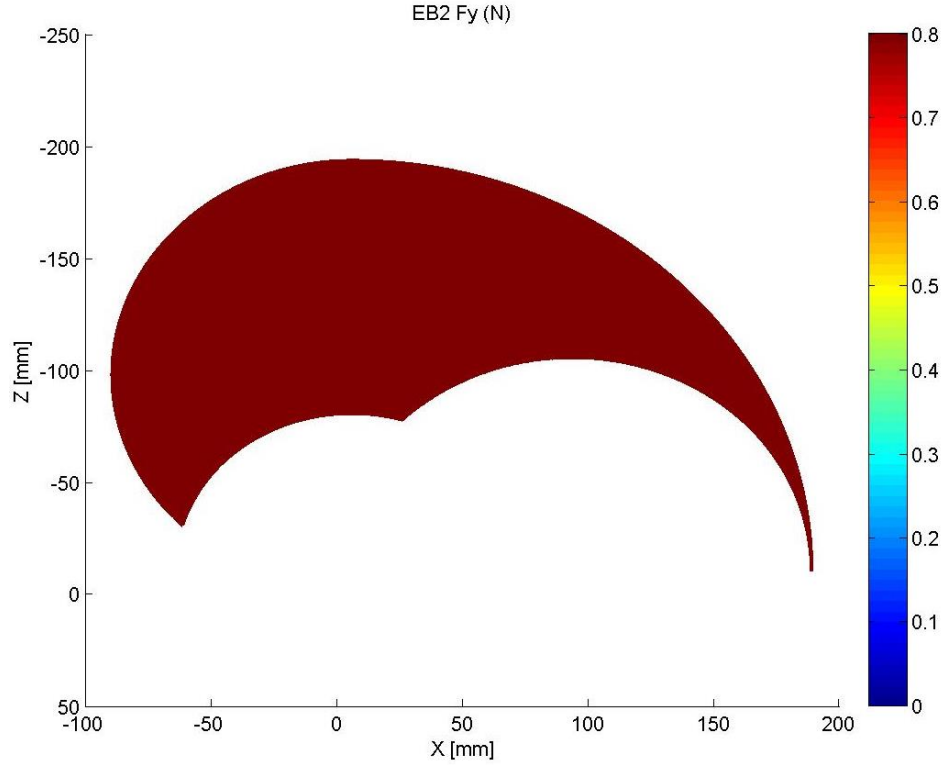


Figure 0.4: EB2.0 static endpoint force deficiencies in the Y principal Cartesian axis, right arm.

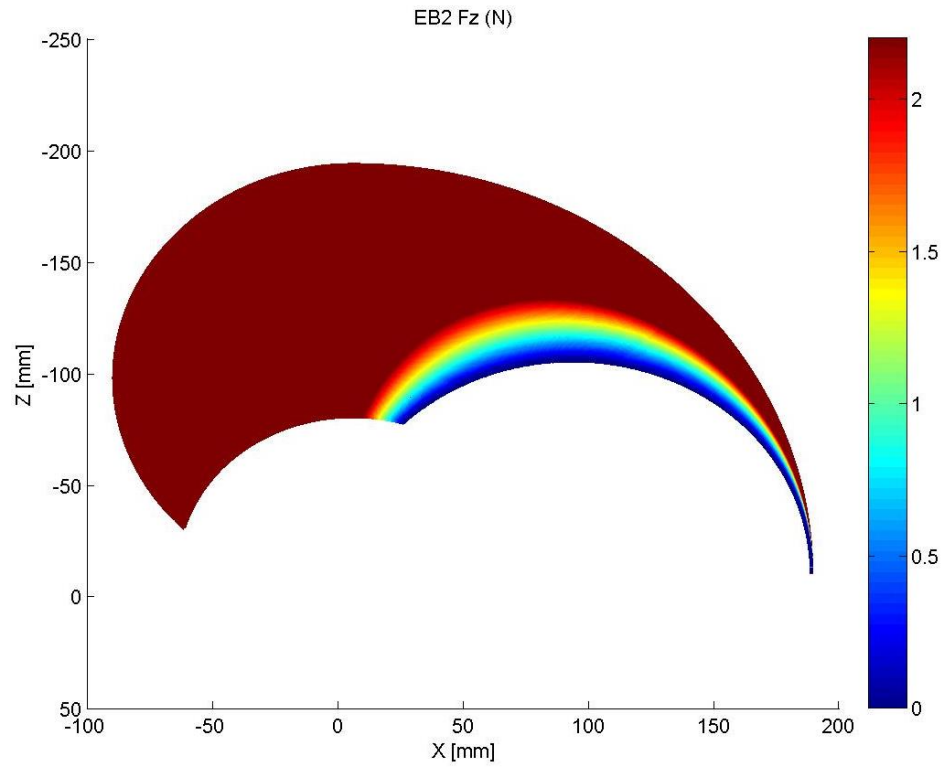


Figure 0.5: EB2.0 static endpoint force deficiencies in the Z principal Cartesian axis, right arm.

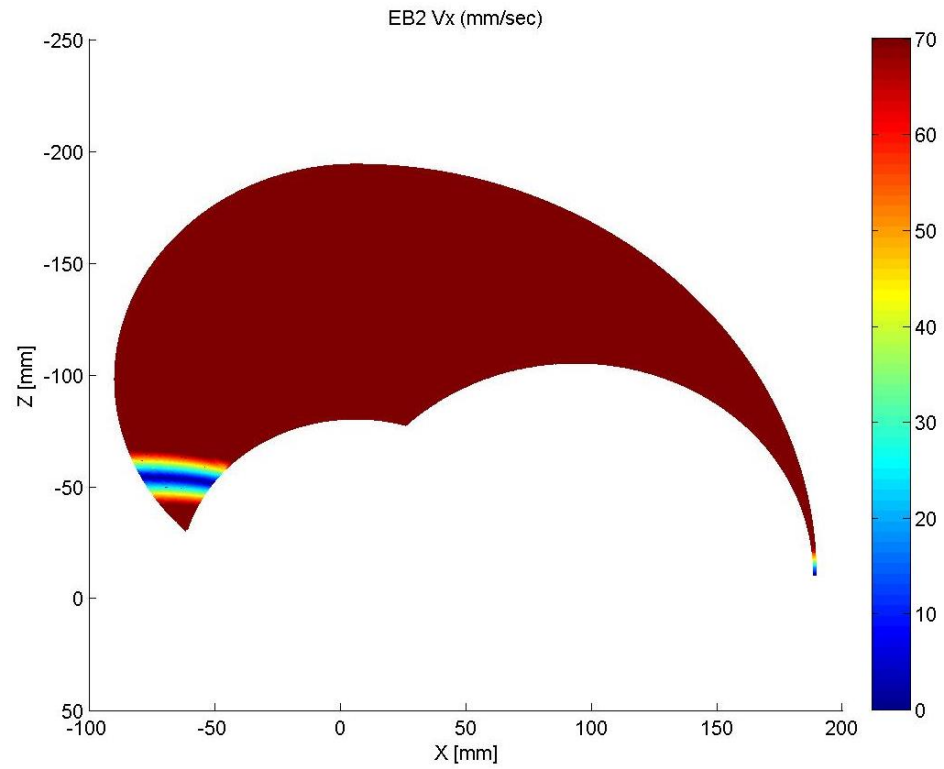
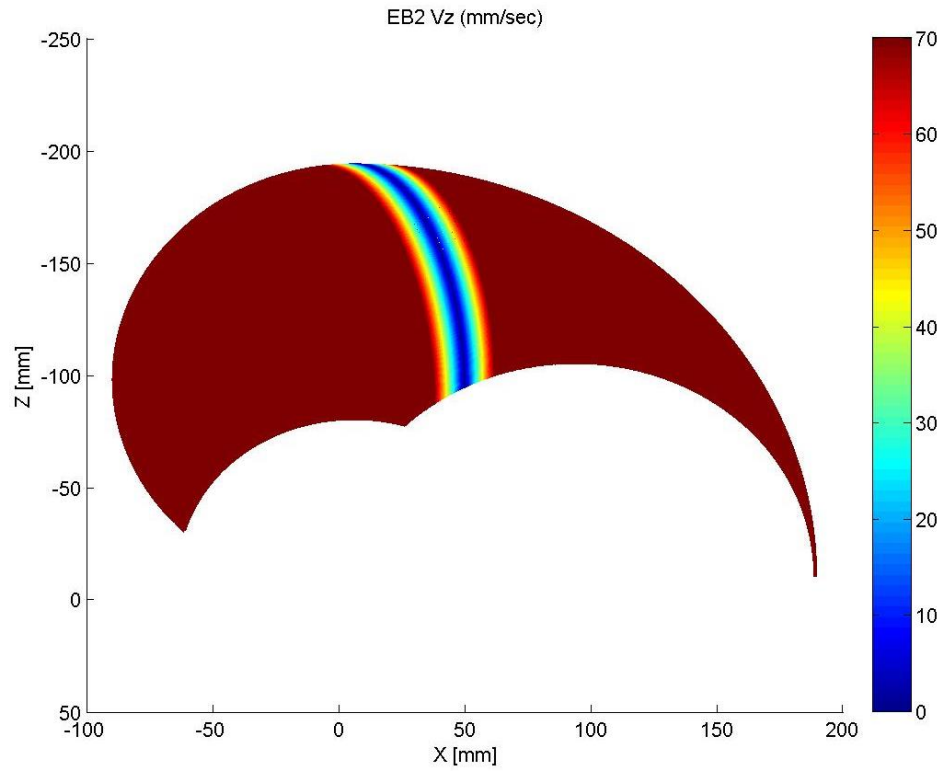


Figure 0.6: EB2.0 endpoint velocity deficiencies in the X principal Cartesian axis, right arm.

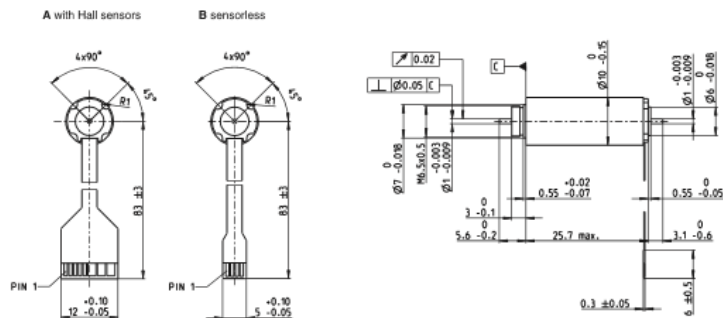


**Figure 0.7: EB2.0 endpoint velocity deficiencies in the Z principal Cartesian axis, right arm.**

# Appendix C. Brushless DC Motor Data Sheets

maxon EC motor

## EC 10 Ø10 mm, brushless, 8 Watt



	Part Numbers			
A with Hall sensors	315170	315171	315172	<b>315173</b>
B sensorless	315174	315175	315176	315177

Motor Data (provisional)					
Values at nominal voltage					
1 Nominal voltage	V	6	9	12	18
2 No load speed	rpm	49200	52500	53200	57100
3 No load current	mA	160	118	90.4	67.3
4 Nominal speed	rpm	41700	45600	46600	50900
5 Nominal torque (max. continuous torque)	mNm	1.74	1.63	1.62	1.61
6 Nominal current (max. continuous current)	A	1.66	1.11	0.843	0.6
7 Stall torque	mNm	12	13	13.7	15.6
8 Starting current	A	10.4	8.05	6.46	5.27
9 Max. efficiency	%	77	78	78	79
Characteristics					
10 Terminal resistance phase to phase	Ω	0.575	1.12	1.86	3.42
11 Terminal inductance phase to phase	mH	0.00998	0.0198	0.0342	0.0671
12 Torque constant	mNm/A	1.15	1.61	2.12	2.97
13 Speed constant	rpm/V	8340	5920	4500	3220
14 Speed/torque gradient	rpm/mNm	4180	4110	3940	3700
15 Mechanical time constant	ms	3.03	2.97	2.85	2.68
16 Rotor inertia	gcm <sup>2</sup>	0.0691	0.0691	0.0691	0.0691

Specifications	Operating Range	Comments
<b>Thermal data</b> 17 Thermal resistance housing-ambient 39.8 K/W 18 Thermal resistance winding-housing 5.1 K/W 19 Thermal time constant winding 1.51 s 20 Thermal time constant motor 221 s 21 Ambient temperature -40...+100°C 22 Max. permissible winding temperature +125°C <b>Mechanical data (preloaded ball bearings)</b> 23 Max. permissible speed 65000 rpm 24 Axial play at axial load < 1.0 N 0 mm > 1.0 N max. 0.14 mm 25 Radial play preloaded 26 Max. axial load (dynamic) 0.8 N 27 Max. force for press fits (static) 12 N (static, shaft supported) 250 N 28 Max. radial loading, 5 mm from flange 2 N <b>Other specifications</b> 29 Number of pole pairs 1 30 Number of phases 3 31 Weight of motor 13 g		<p><b>Continuous operation</b>                      In observation of above listed thermal resistance (lines 17 and 18) the maximum permissible winding temperature will be reached during continuous operation at 25°C ambient.                      = Thermal limit.</p> <p><b>Short term operation</b>                      The motor may be briefly overloaded (recurring).</p> <p>Assigned power rating</p>

maxon Modular System		Overview on page 20 - 25
<b>Connection</b> Pin 1 V <sub>HE</sub> 4.5...24 VDC Pin 2 Hall sensor 3 Pin 3 Hall sensor 1 Pin 4 Hall sensor 2 Pin 5 GND Pin 6 Motor winding 3 Pin 7 Motor winding 2 Pin 8 Motor winding 1 <b>Adapter</b> see p. 339 <b>Connector</b> Tyco 1-84953-1 Molex 52207-1185 Molex 52089-1119 Pin for design with Hall sensors: FPC, 11-pol, Pitch 1.0 mm, top contact style	<b>Planetary Gearhead</b> Ø10 mm 0.01 - 0.15 Nm Page 233	<b>Recommended Electronics:</b> ESCON 36/3 EC Page 320 ESCON Module 50/5 321 ESCON 50/5 321 DECS 50/5 324 DEC Module 24/2 325 DEC Module 50/5 325 <b>Notes</b> 24



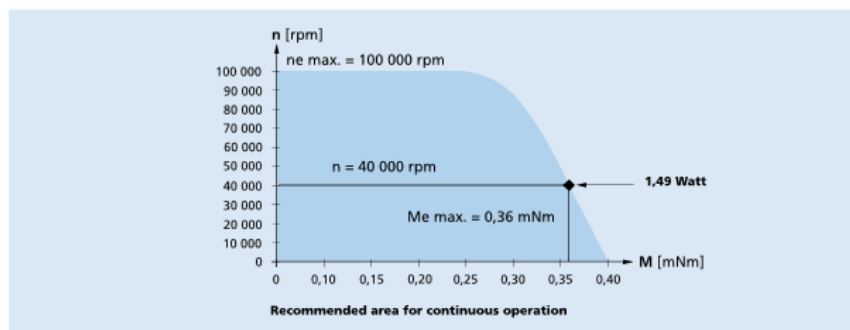
## Brushless DC-Servomotors

0,36 mNm

For combination with  
Gearheads:  
06/1  
Encoder:  
PA2-50, HXM3-64  
Drive Electronics:  
Speed Controller, Motion Controller

## Series 0620 ... B

	0620 K	006 B	012 B	
1 Nominal voltage	$U_N$	6	12	Volt
2 Terminal resistance, phase-phase	$R$	9,1	59,0	$\Omega$
3 Output power <sup>1)</sup>	$P_2 \text{ max.}$	1,47	1,49	W
4 Efficiency	$\eta \text{ max.}$	52	50	%
5 No-load speed	$n_0$	46 500	35 600	rpm
6 No-load current (with shaft $\phi$ 1,0 mm)	$I_0$	0,062	0,020	A
7 Stall torque	$M_H$	0,73	0,57	mNm
8 Friction torque, static	$C_0$	0,023	0,023	mNm
9 Friction torque, dynamic	$C_v$	$1,0 \cdot 10^{-6}$	$1,0 \cdot 10^{-6}$	mNm/rpm
10 Speed constant	$k_n$	8 451	3 282	rpm/V
11 Back-EMF constant	$k_E$	0,118	0,305	mV/rpm
12 Torque constant	$k_M$	1,13	2,91	mNm/A
13 Current constant	$k_I$	0,885	0,344	A/mNm
14 Slope of n-M curve	$\Delta n/\Delta M$	68 054	66 533	rpm/mNm
15 Terminal inductance, phase-phase	$L$	26	187	$\mu\text{H}$
16 Mechanical time constant	$\tau_m$	6	6	ms
17 Rotor inertia	$J$	0,0095	0,0095	$\text{gcm}^2$
18 Angular acceleration	$\alpha \text{ max.}$	768	601	$\cdot 10^3 \text{rad/s}^2$
19 Thermal resistance	$R_{th1} / R_{th2}$	14 / 88,0		K/W
20 Thermal time constant	$\tau_{w1} / \tau_{w2}$	1 / 149		s
21 Operating temperature range:				
– motor		-20 ... +100		$^{\circ}\text{C}$
– coil, max. permissible		+125		$^{\circ}\text{C}$
22 Shaft bearings		ball bearings, preloaded		
23 Shaft load max.:				
– radial at 10 000/50 000 rpm (3,7 mm from mounting flange)		2,0 / 1,5		N
– axial at 10 000/50 000 rpm (push-on only)		0,6 / 0,2		N
– axial at standstill (push-on only)		10		N
24 Shaft play:				
– radial	$\leq$	0,012		mm
– axial	$=$	0		mm
25 Housing material		aluminium, black anodized		
26 Weight		2,5		g
27 Direction of rotation		electronically reversible		
<b>Recommended values - mathematically independent of each other</b>				
28 Speed up to <sup>2)</sup>	$n \text{ max.}$	100 000	100 000	rpm
29 Torque up to <sup>1) 2)</sup>	$M \text{ max.}$	0,351	0,356	mNm
30 Current up to <sup>1) 2)</sup>	$I \text{ max.}$	0,367	0,144	A

<sup>1)</sup> at 40 000 rpm<sup>2)</sup> thermal resistance  $R_{th2}$  by 55% reduced

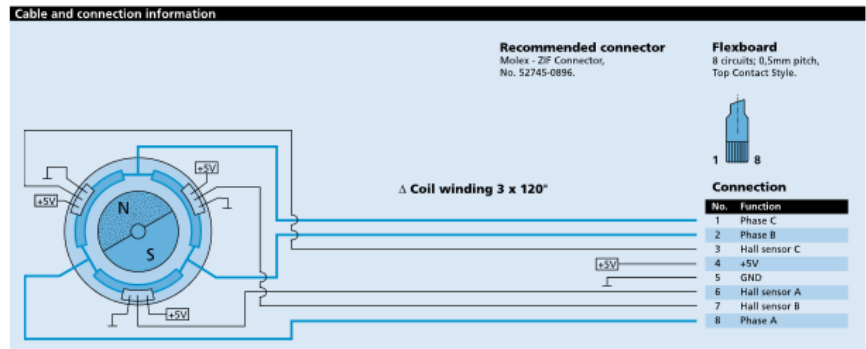
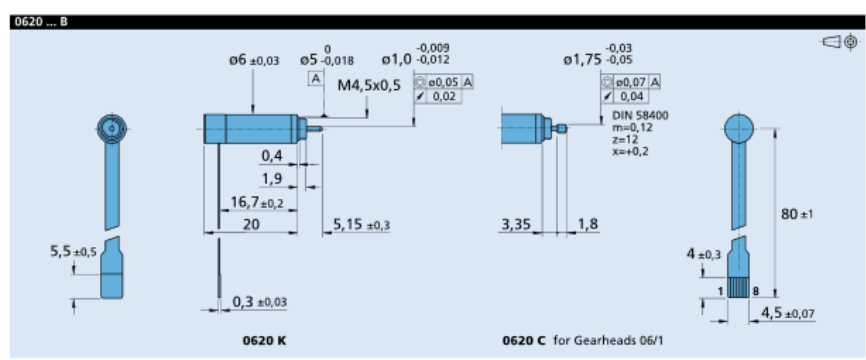
For notes on technical data and lifetime performance refer to "Technical Information".  
Edition 2011 – 2012

Page 1/2

© DR. FRITZ FAULHABER GMBH & CO. KG  
Specifications subject to change without notice.



**Options**  
 K1855:  
 Motors for operation with Motion Controllers  
 MCBL 3003 S/C, MCBL 3006 S/C.



For notes on technical data and lifetime performance refer to "Technical Information".  
 Edition 2011 – 2012





## Planetary Gearheads

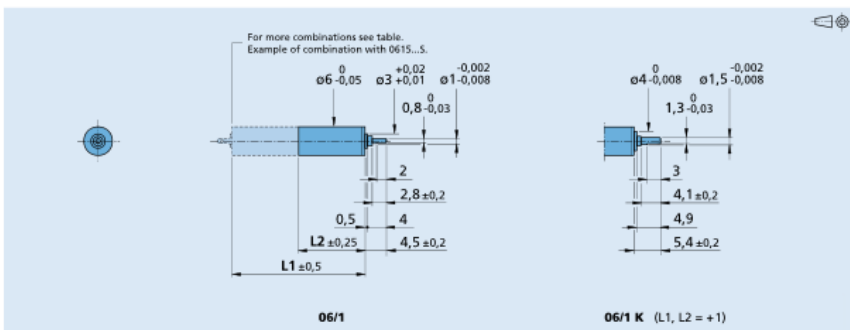
25 mNm

For combination with  
DC-Motors  
Brushless DC-Motors  
Stepper Motors

### Series 06/1

	06/1	06/1K
Housing material	steel	steel
Geartrain material	steel	steel
Recommended max. input speed for:		
- continuous operation	8 000 rpm	8 000 rpm
Backlash, at no-load	≤ 3 °	≤ 3 °
Bearings on output shaft	sintered bearings	ball bearings
Shaft load, max.:		
- radial (3,5 mm from mounting face)	≤ 0,5 N	≤ 5 N
- axial	≤ 0,5 N	≤ 3 N
Shaft press fit force, max.	≤ 3,5 N	≤ 5 N
Shaft play		
- radial (3,5 mm from mounting face)	≤ 0,06 mm	≤ 0,06 mm
- axial	≤ 0,1 mm	≤ 0,05 mm
Operating temperature range	- 30 ... + 100 °C	- 30 ... + 100 °C

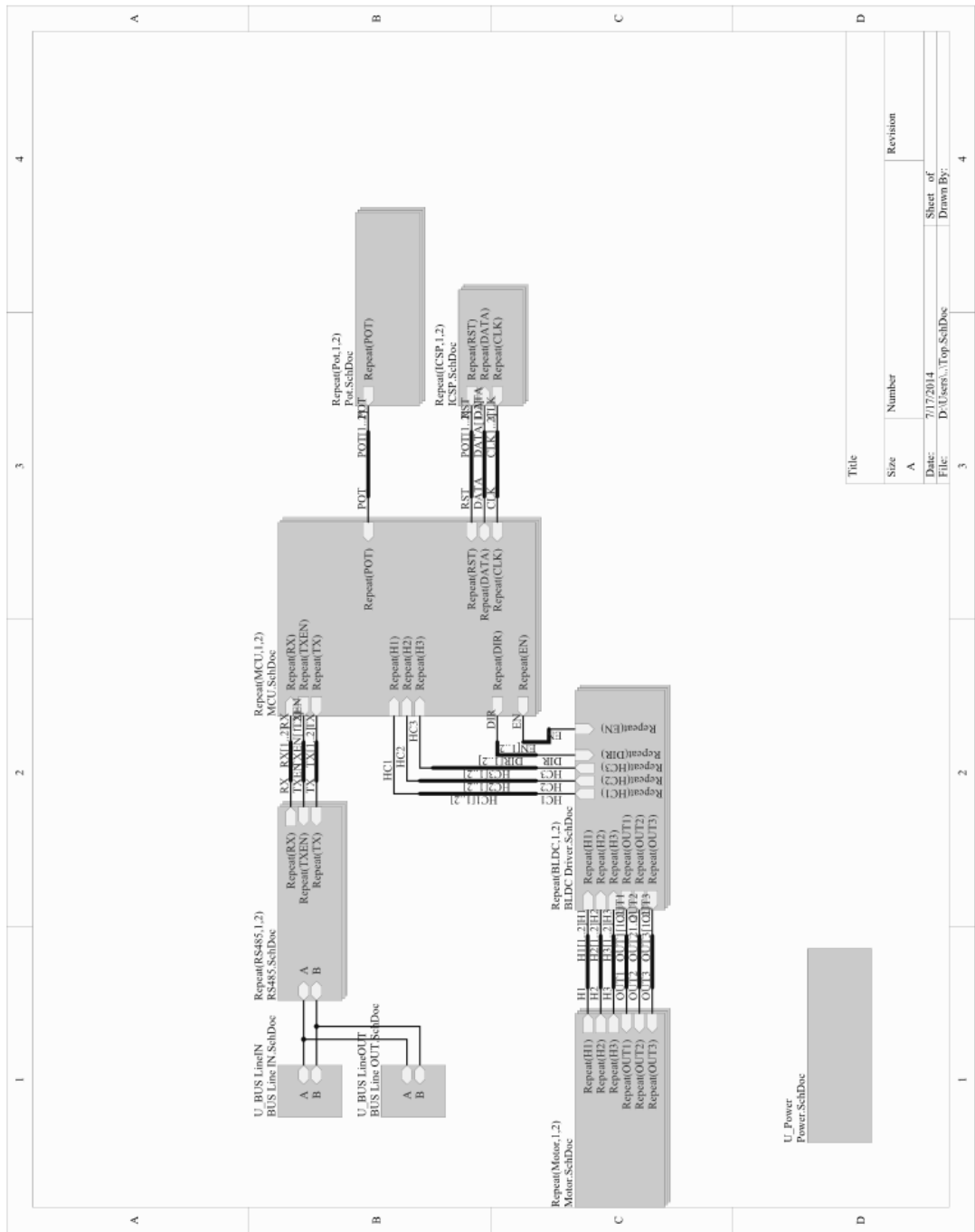
Specifications		1	2	3	4	5	6
Number of gear stages		1	2	3	4	5	6
Continuous torque	mNm	25	25	25	25	25	25
Intermittent torque	mNm	35	35	35	35	35	35
Mass without motor, ca.	g	2	2,8	3,4	4	4,4	5
Efficiency, max.	%	90	80	70	60	55	48
Direction of rotation, drive to output		=	=	=	=	=	=
Reduction ratio (exact)		4:1	16:1	64:1	256:1	1 024:1	4 096:1
L2 [mm] = length without motor		9,2	11,9	14,6	17,3	20,0	22,7
L1 [mm] = length with motor	0615C...S	24,2	26,9	29,6	32,3	35,0	37,7
	0620C...B	29,2	31,9	34,6	37,3	40,0	42,7
	ADM0620...-05	18,8	21,5	24,2	26,9	29,6	32,3



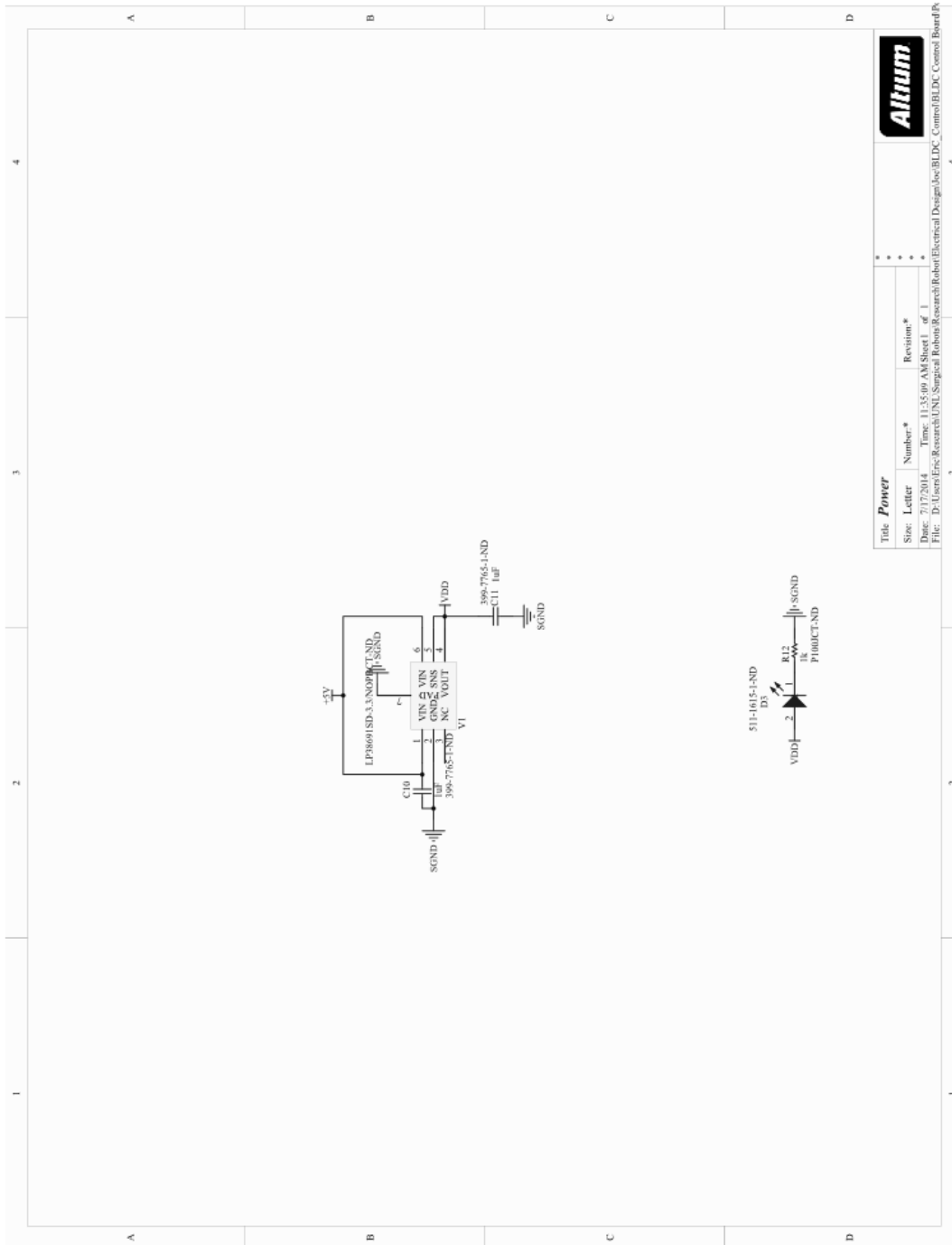
For notes on technical data and lifetime performance refer to "Technical Information".  
Edition 2014

© DR. FRITZ FAULHABER GMBH & CO. KG  
Specifications subject to change without notice.  
www.faulhaber.com

# Appendix D. Distributed Motor Control Schematics

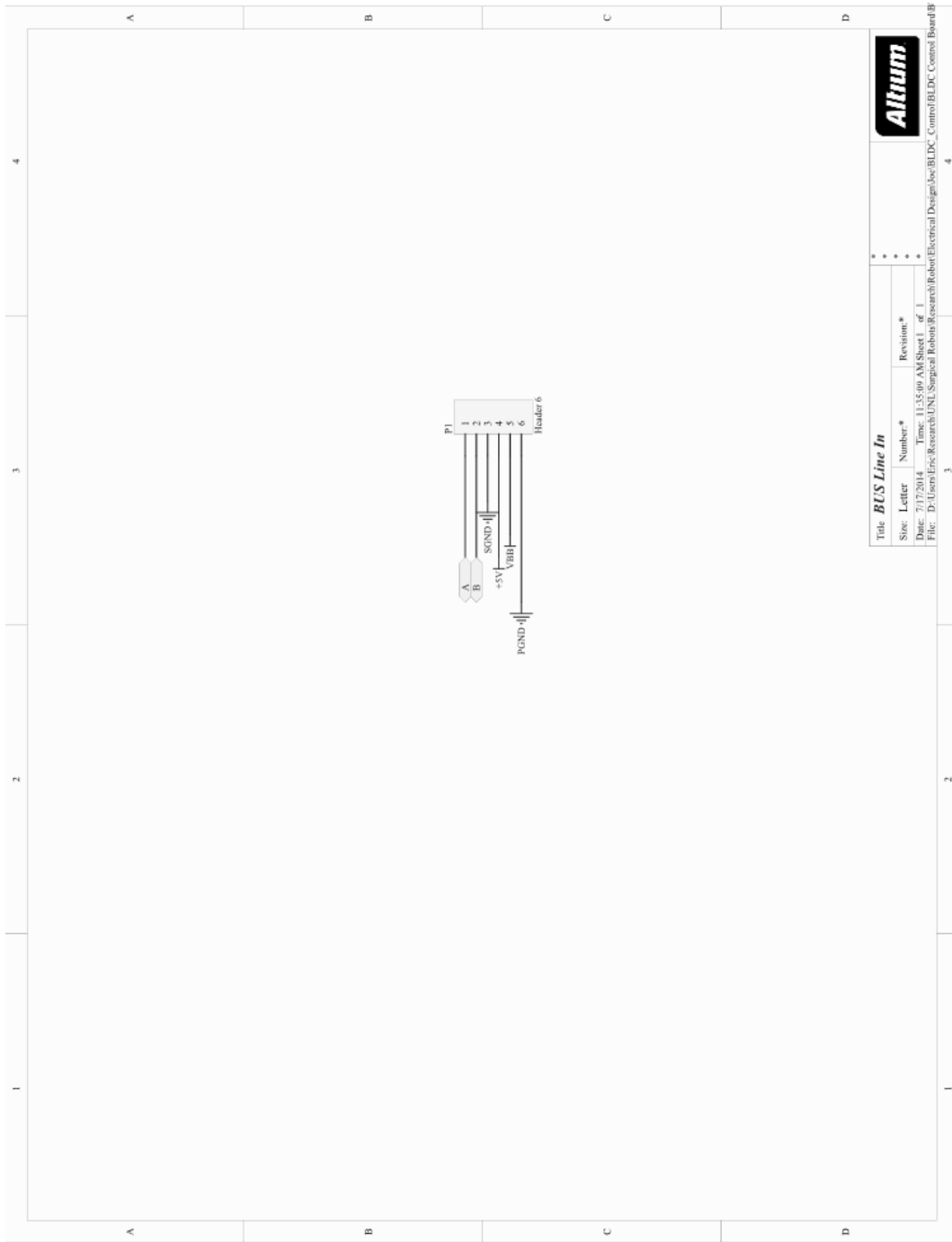


Title	Size	Number	Revision
	A		
Date:	7/17/2014		
File:	D:\Users\...Top_SchDoc		
	3		4



Title: <b>Power</b>			
Size	Letter	Number	Revision
			*
Date:	Time: 11:35:00 AM Sheet 1 of 1		
File:	D:\User\Eric_Research\UNI_Surgical_Robots\Research\Robot\Electrical_Design\loc_BLD_Control Board\FK		

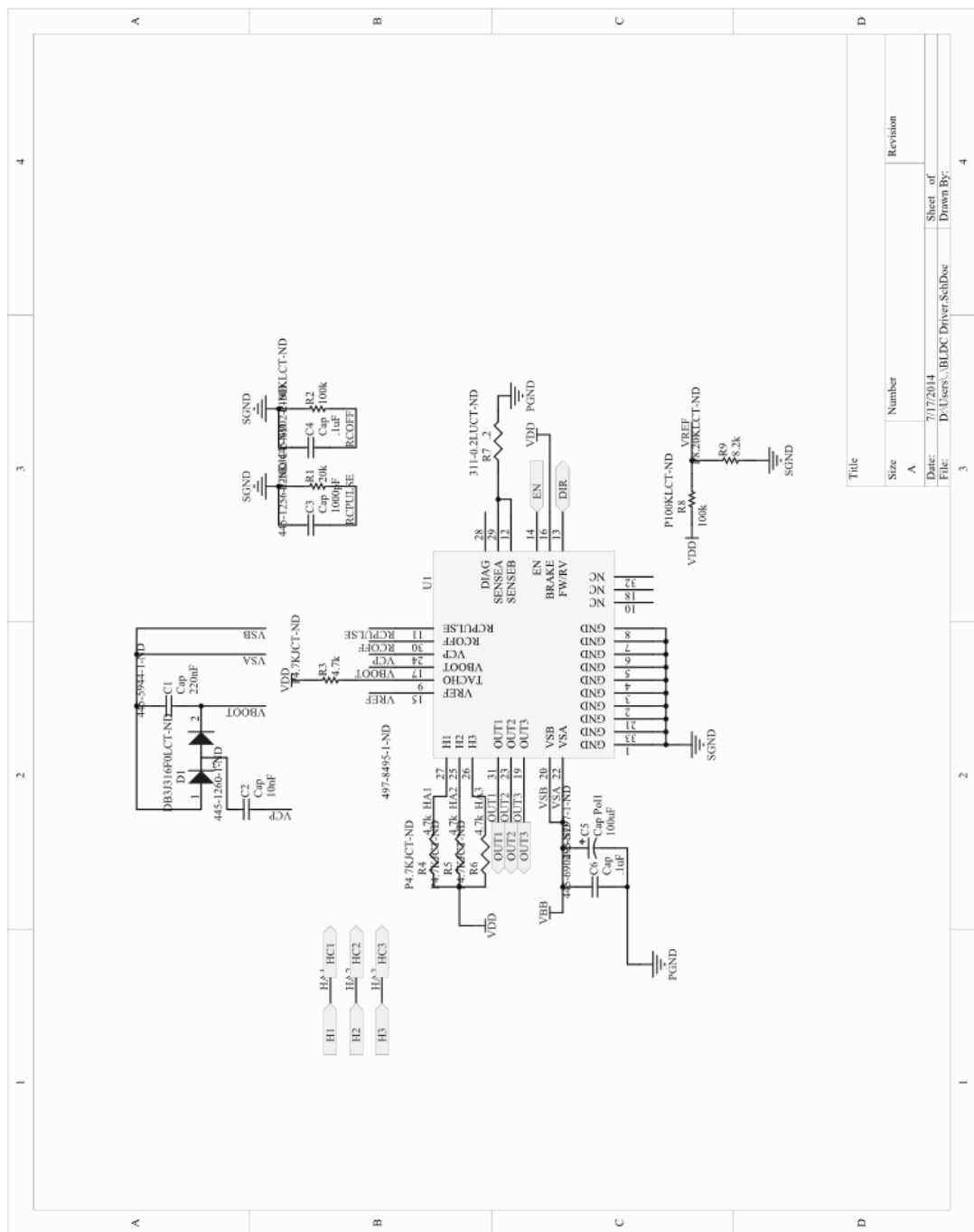




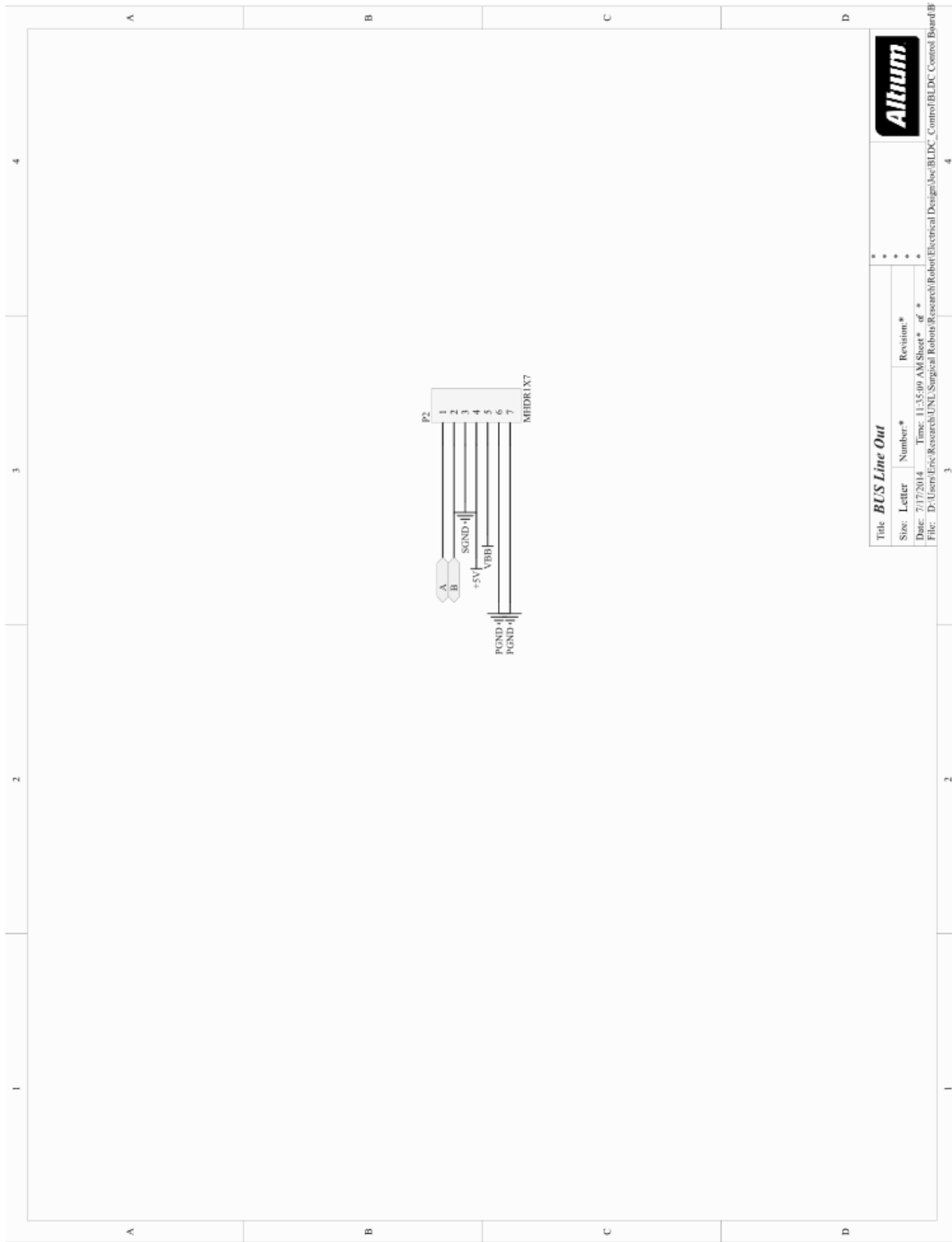
Title: **BUS Line In**

Size	Letter	Number	Revision
			*

Date: 7/17/2014 Time: 11:35:00 AM Sheet 1 of 1  
File: D:\User\Eric\_Research\UNI\_Surgical\_Robots\Research\Robot\Electrical Design\Job\BLDC\_Control Board\B



Title	
Size	Number
A	A
Date:	7/17/2014
File:	D:\Users\... \BLDC Driver\SchDoc
Sheet of	4
Drawn By:	



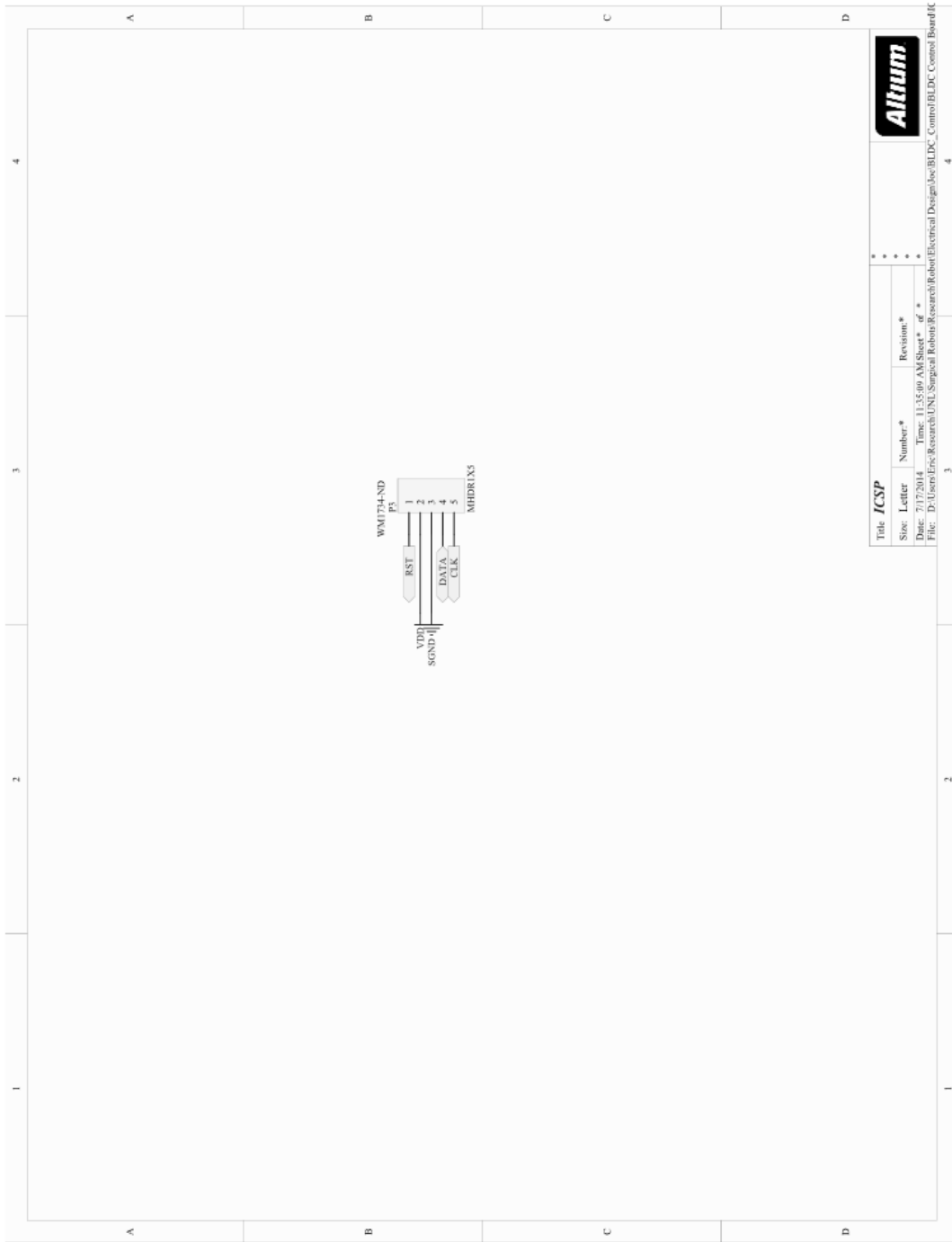
Title: **BUS Line Out**

Size	Letter	Number	Revision
			*

Date: 7/17/2014 Time: 11:35:00 AM Sheet \* of \*

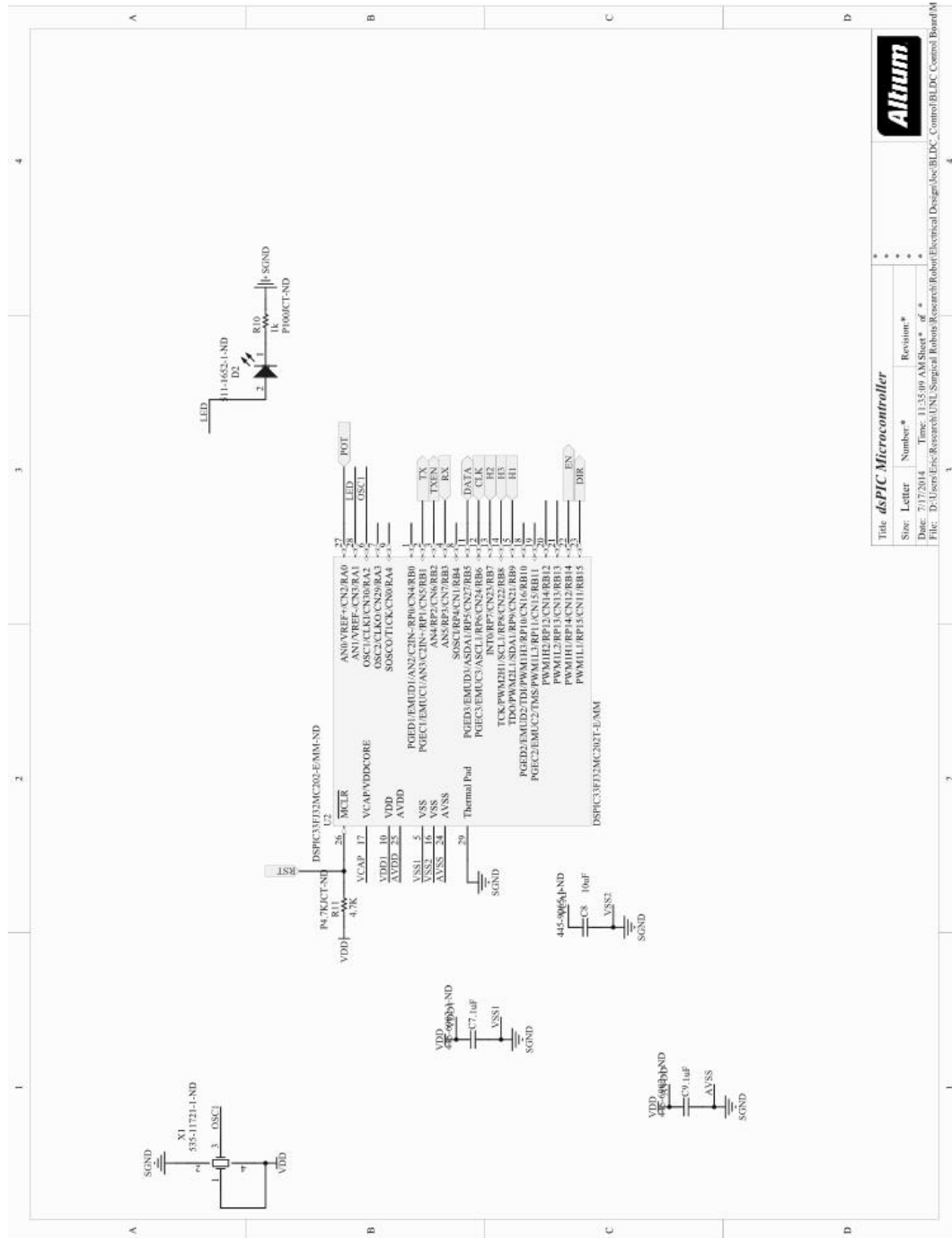
File: D:\User\Eric\_Research\UNI\_Surgical\_Robots\Research\Robot\Electrical Design\Job\BLDC\_Control\Board\B

3 4



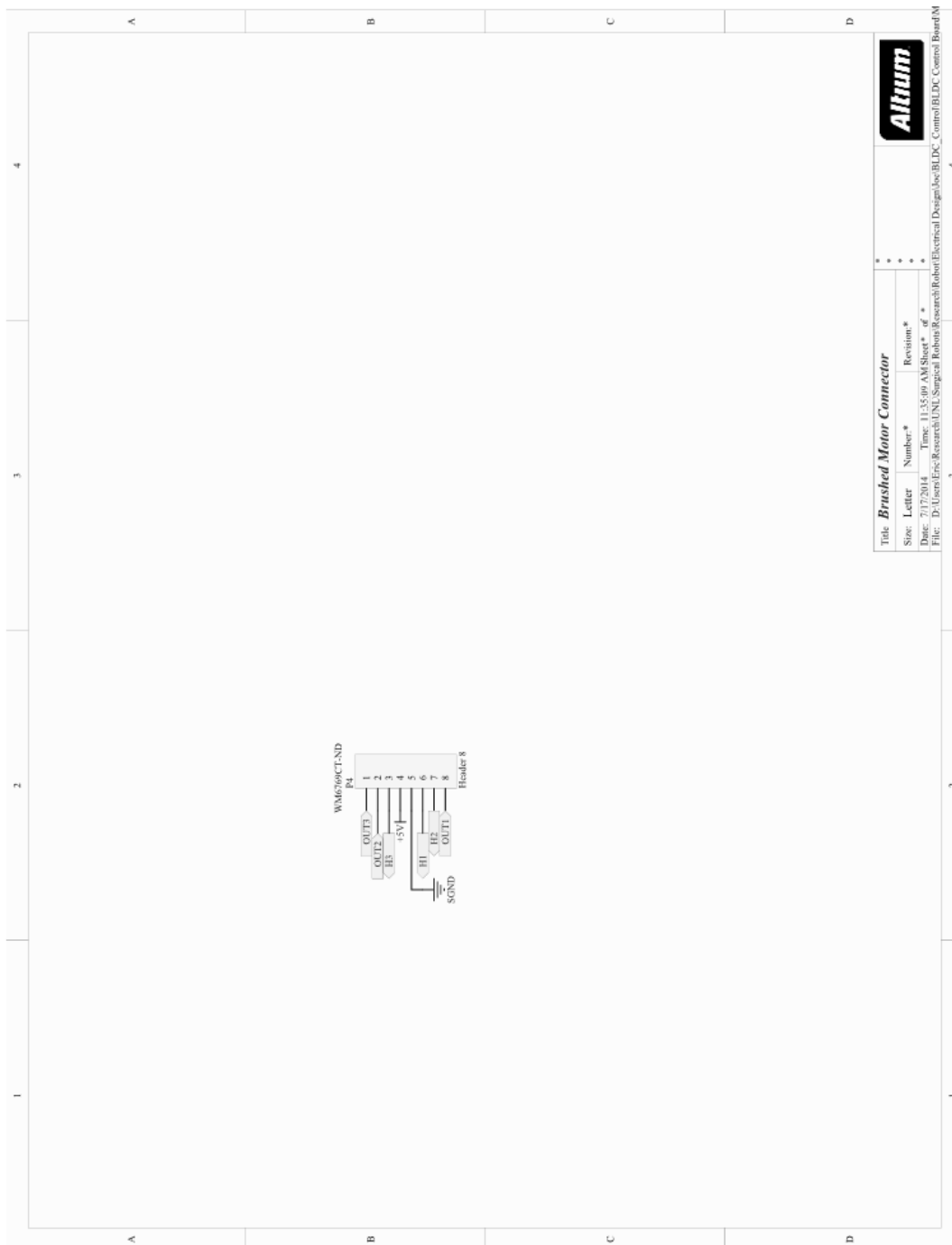
Title: ICSP	
Size: Letter	Number: *
Date: 7/17/2014	Time: 11:35:00 AM
File: D:\User\Eric_Research\UNI_Surgical_Robots\Research\Robot\Electrical_Design\Job_BLD_C Control Board\IC	Revision: *

Page 3 of 4



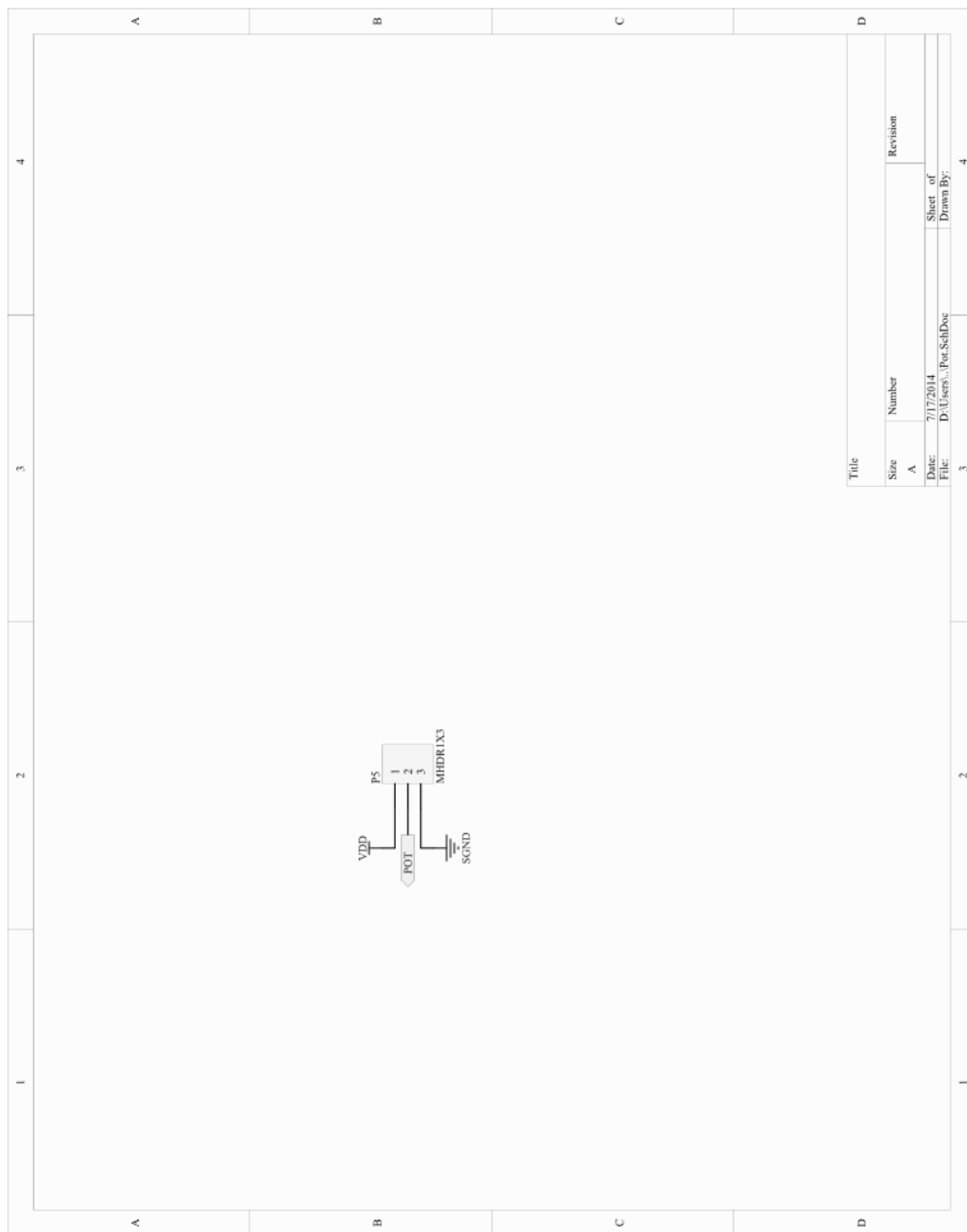
Title: dsPIC Microcontroller	
Size	Letter
Number	Revision
Date: 7/17/2014	Time: 11:35:00 AM Sheet # of #
File: D:\Users\Eric_Research\LNLSurgical\Robots\Research\Electrical Design\loc/BLDC_Control/BLDC_Control_Board.M	



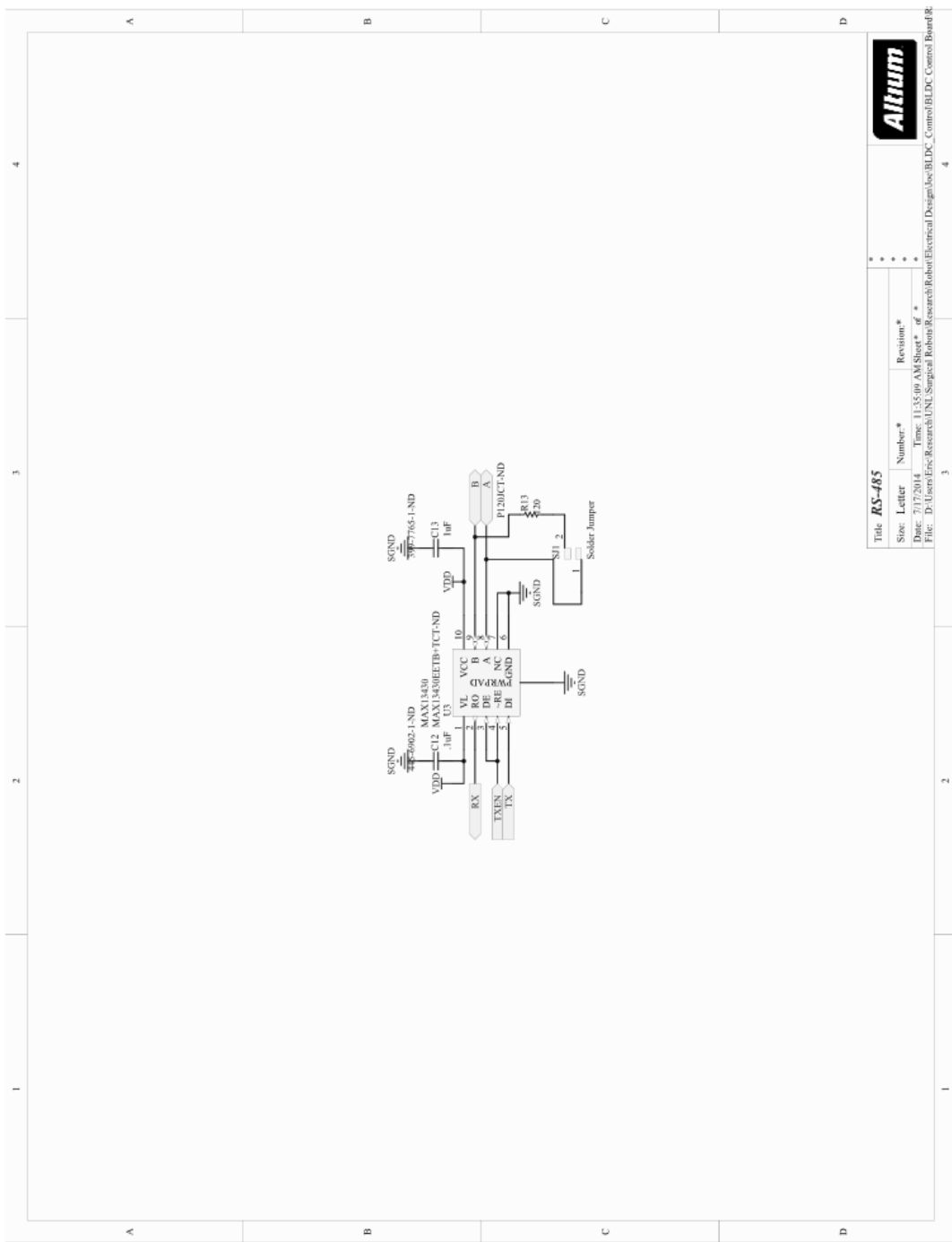


Title: <b>Brushed Motor Connector</b>			
Size:	Letter:	Number:	Revision:
			*
Date:	Time:		of
File:	D:\Users\Eric.Research\NL\Surgical Robots\Research\Robot\Electrical Design\Bldc Control\Bldc Control Board.M		





Title	
Size	Number
A	
Revision	
Date: 7/17/2014	
File: D:\Users\...Pot.SchDoc	
Sheet of	
Drawn By:	



Title: <b>RS-485</b>		Revision: *	
Size: Letter	Number: *	Revision: *	
Date: 7/17/2014	Time: 11:35:00 AM	Sheet * of *	
File: D:\Users\Eric.Research\NL\Surgical\Robot\Research\Robot\Electrical Design\Bldc Control\Bldc Control Board.R			